

A Frequency Domain Beamforming Method to Locate Moving Sound Sources

Hugo Elias Camargo

Dissertation submitted to the faculty of the Virginia Polytechnic Institute and State University in
partial fulfillment of the requirements for the degree of

Doctor of Philosophy
in
Mechanical Engineering

Ricardo A. Burdisso, Chair
William J. Devenport, Co-Chair
Marty E. Johnson
Alfred L. Wicks
Mark R. Paul

May 4, 2010
Blacksburg, Virginia

Keywords: Aeroacoustics, Phased Array, Frequency Domain Beamforming, De-Dopplerization,
Moving Sound Sources

Copyright 2010

A Frequency Domain Beamforming Method to Locate Moving Sound Sources

Hugo Elias Camargo

ABSTRACT

A new technique to de-Dopplerize microphone signals from moving sources of sound is derived. Currently available time domain de-Dopplerization techniques require oversampling and interpolation of the microphone time data. In contrast, the technique presented in this dissertation performs the de-Dopplerization entirely in the frequency domain eliminating the need for oversampling and interpolation of the microphone data. As a consequence, the new de-Dopplerization technique is computationally more efficient.

The new de-Dopplerization technique is then implemented into a frequency domain beamforming algorithm to locate moving sources of sound. The mathematical formulation for the implementation of the new de-Dopplerization technique is presented for sources moving along a linear trajectory and for sources moving along a circular trajectory, i.e. rotating sources.

The resulting frequency domain beamforming method to locate moving sound sources is then validated using numerical simulations for various source configurations (e.g. emission angle, emission frequency, and source velocity), and different processing parameters (e.g. time window length). Numerical datasets for sources with linear motion as well as for rotating sources were simulated. For comparison purposes, selected datasets were also processed using traditional time domain beamforming. The results from the numerical simulations show that the frequency domain beamforming method is at least 10 times faster than the traditional time domain beamforming method with the same performance. Furthermore, the results show that as the number of microphones and/or grid points increase, the processing time for the traditional time domain beamforming method increases at a rate 20 times larger than the rate of increase in processing time of the new frequency domain beamforming method.

Dedicated with love to my family.

Acknowledgements

I would like to express my most sincere gratitude to my advisor Dr. Ricardo Burdisso for his guidance throughout my years at Virginia Tech and beyond. His support, advice and mentorship have helped me accomplish this goal in life which is the completion of my doctoral degree.

I would also like to thank my Co-Chair Dr. William Devenport for always providing me help and advice when I needed, not only academically but also personally. Thanks are also due to the members of my committee Dr. Marty Johnson, Dr. Mark Paul and Dr. Al Wicks for the knowledge gained in their lectures and also for their valuable feedback in the preparation of this dissertation.

My gratitude is also to my friends who made my passage through Blacksburg very memorable. In especial, I would like to thank my friends Patricio Ravetta and Marcel Remillieux for sharing the good and the hard times and for always giving me a hand when I needed most.

I could not have succeeded in this endeavor without the love and comprehension of my wife Fulvia and my daughters Anahi and Nicole; they are my inspiration, to them I am thankful. I am also thankful to my parents Maria Elena and Hugo for giving me the opportunity to be here, and to my sister Maria del Pilar and my niece Mayra for their selfless and unconditional love.

My acknowledgement is also to my supervisor Mr. Peter G. Kovalchik for all his support, encouragement and generosity, and for allowing me to focus on the completion of this dissertation.

Finally, I would like to thank God for giving me the most precious gift of life and for walking along by my side in this journey.

Table of Contents

	Page
Index of Figures.....	vii
Chapter 1 Introduction.....	1
1.1 Literature Review.....	2
1.2 Motivation.....	5
1.3 Objectives	5
1.4 Dissertation Organization	6
Chapter 2 Acoustic Field of Monopole Sources of Sound	7
2.1 Acoustic Field of a Fixed Monopole Source	7
2.2 Acoustic Field of a Moving Monopole Source.....	10
2.3 De-Dopplerization Technique.....	23
2.4 Interpolation of the de-Dopplerized Signal.....	30
Chapter 3 Current Beamforming Methods	32
3.1 Time Domain Beamforming for Stationary Sound Sources	32
3.2 Time Domain Beamforming for Moving Sound Sources.....	38
3.3 Frequency Domain Beamforming for Stationary Sound Sources.....	50
Chapter 4 A New Frequency Domain Beamforming Method	54
4.1 Introduction to the New Method.....	55
4.2 Linear, Translation, and Scaling Properties of the Fourier Transform	55
4.3 Frequency Domain de-Dopplerization.....	58
4.4 Beamformer Implementation	66
4.5 Application to Rotating Sources	70
Chapter 5 Numerical Validation of the New Beamforming Method	75
5.1 The Relative Phase between Microphones	75
5.2 Validation of the de-Dopplerization Technique	80
5.3 Validation of the Frequency Domain Beamforming Approach.....	95
5.4 Parametric Studies	101
5.5 Remarks from the Numerical Validation.....	117

Chapter 6	Conclusions and Future Work.....	119
6.1	Conclusions.....	119
6.2	Future Work.....	120
References.....		122
APPENDIX A: Derivation of Equations.....		125
A1.1	Properties of Delta Dirac Function δ	125
A1.2	Derivative of Equation $g(\tau) = t - \tau - \bar{x} - \bar{x}_s(\tau) /c$	125
A1.3	Derivation of $\partial\tau/\partial t$	126
A.1.4	Derivation of the Discrete Fourier Transform Equations	128
A1.5	Shifting and Scaling Properties of the Fourier Transform.....	130
A1.6	Linearization of the Reception vs Emission Times	132

Index of Figures

	Page
Figure 2.1: Schematic representation of a source field and the sound field induced by this source.	9
Figure 2.2: Sound perceived by a stationary observer from a source of sound moving in a linear path at constant speed.....	13
Figure 2.3: Component of the source velocity in the direction of source-to-observer at emission time.....	14
Figure 2.4: Effect of source motion on the acoustic field.....	15
Figure 2.5: Monopole in linear constant speed motion.	16
Figure 2.6: Monopole source moving in a circular trajectory. Position and velocity vectors with respect to (a) microphone m_1 , and (b) microphone m_2	19
Figure 2.7: Effect of motion on the acoustic field of a monopole source - $\omega = 500 \times 2\pi \text{ rad} / \text{s}$, $\omega_r = 1500 \times 2\pi / 60 \text{ rad} / \text{s}$, $R=0.5 \text{ m}$, $L=1 \text{ m}$, $M_{tip} = \omega_r R / c = 0.22$	21
Figure 2.8: Schematic of the transcendental equation to find emission time from reception time for a rotating source.....	22
Figure 2.9: Physical interpretation of de-Dopplerization: (a) stationary microphone with signal affected by the Doppler effect and (b) microphone moving with the source (e.g. stationary relative to the source) with signal de-Dopplerized.	24
Figure 2.10: Steps involved in the de-Dopplerization of the signal in terms of emission time: (a) original source position, and (b) original microphone signal measured at equal interval of emission times, (c) estimated source strength signal at emission times, and (d) estimated sound signal at reference observer position	27

Figure 2.11: Steps involved in the de-Dopplerization of the signal in terms of reception time: (a) original source position signal, and (b) microphone signal measured at equal interval of reception times, (c) estimated source strength signal at emission times, and (d) estimated sound signal at reference observer position	29
Figure 3.1: Array of microphones sampling the acoustic field of a stationary monopole source.	33
Figure 3.2: Beamforming to a potential source location \vec{x}_b	34
Figure 3.3: Example of acoustic maps obtained using a frequency domain beamforming algorithm.	38
Figure 3.4: Acoustic field of a monopole source with linear motion, sampled by an array of N -microphones	39
Figure 3.5: Illustration of (a) source position signal, (b) n^{th} microphone signals, (c) estimated source strength, and (d) n^{th} de-Depplorization microphone signal for reference location of source.....	41
Figure 3.6: Sound field of a rotating source recorded by an array of microphones.	45
Figure 3.7: First step in the TD beamforming algorithm: A period of revolution is identified and divided into a set of J equally spaced emission times.....	46
Figure 3.8: Illustration of (a) angular source position signal, (b) n th microphone signals, and (c) estimated de-Dopplerized source strength	47
Figure 4.1: (a) Original and (b) translated and scaled signals.	56
Figure 4.2: Source of sound moving along the 1-direction, sensed by a fixed microphone located at \vec{x}_n	59
Figure 4.3: Emission time window and its correspondent reception time window over a short time period.....	61
Figure 4.4: Extraction of the microphone signal that is associated to the emitted sound by the source during time window T	63

Figure 4.5: Schematic of grid moving with the vehicle over time window T .	67
Figure 4.6: Schematic of the scanning grid points moving (rotating) with the same source angular speed.	71
Figure 4.7: Schematic of the approximation of the circular trajectory into a sequence of linear segments.	72
Figure 4.8: Extraction of the microphone data at reception time for each emission time window for a source moving along a circular trajectory.	73
Figure 5.1: Example used to illustrate the relative phase between microphones using the linear approximation for the reception times	76
Figure 5.2: Time delay $ \bar{x}_n - \bar{x}_s(\tau) /c$ as a function of the emission time τ exact and linear approximation. Case: source at $x_{n1} = 40m$ and $x_{m1} = 60m$ at $\tau = 0$ and $T=0.3$ sec.	77
Figure 5.3: Relative time delay between microphones, $ \bar{x}_n - \bar{x}_s(\tau) /c - \bar{x}_m - \bar{x}_s(\tau) /c$ as a function of the emission time τ exact and from linear approximations. Case: source at $x_{n1} = 40m$ and $x_{m1} = 60m$ at $\tau = 0$ and $T=0.3$ sec.	77
Figure 5.4: Example used to illustrate the relative phase between microphones using the linear approximation for the reception times (Source passing over one microphone).	78
Figure 5.5: Time delay $ \bar{x}_n - \bar{x}_s(\tau) /c$ as a function of the emission time τ exact and linear approximation. Case: source at $x_{n1} = 0m$ and $x_{m1} = 20m$ at $\tau = 0$ and $T=0.3$ sec.	79
Figure 5.6: Relative time delay between microphones, $ \bar{x}_n - \bar{x}_s(\tau) /c - \bar{x}_m - \bar{x}_s(\tau) /c$ as a function of the emission time τ exact and from linear approximations. Case: source at $x_{n1} = 0m$ and $x_{m1} = 20m$ at $\tau = 0$ and $T=0.3$ sec	79
Figure 5.7: Simulated monopole source moving from position $(0,0,0)$ to position $(100,0,0)$, passing over a fixed microphone located at $(50,0,50)$. The source	

emits sound at 1000 Hz, 1250 Hz and 1600 Hz with amplitudes of 10000, 9000, and 8000 Kg/s², respectively. To compute the de-Dopplerized source strength signal, the source trajectory is divided into 25 segments of equal length (4 meters each). 81

Figure 5.8: Data sampled by the microphone: (a) Original time signal sampled as the source moved 100 meters from position (0,0,0) to (100,0,0) , and b) Fourier transform of this signal..... 81

Figure 5.9: (a) Fourier transform of microphone signals with Doppler effect and (b) corresponding de-Dopplerized source strength spectra computed from each time window..... 82

Figure 5.10: De-Dopplerized Fourier transforms of the source strength signal computed using emission *time windows of 0.06 seconds* each. (Source moving along the x-direction at 100 m/s (Mach 0.29) along a linear trajectory located at 30 meters from the observer). 85

Figure 5.11: De-Dopplerized Fourier transforms of the source strength signal computed using emission *time windows of 0.08 seconds* each. (Source moving along the x-direction at 100 m/s (Mach 0.29) along a linear trajectory located at 30 meters from the observer). 86

Figure 5.12: Maximum time window length for various source velocities and various observer-to-source trajectory distances. Selection of a window length below the curve for a particular source velocity allows recovering the correct frequency content of the FT of the source strength signal. 88

Figure 5.13: Original source strength signal (red), de-Dopplerized source strength signal using the correct source velocity (black), and de-Dopplerized source strength signal using a source velocity 2% greater than the correct source velocity. (Monopole source moving along the x-direction at 100 m/s) 90

Figure 5.14: Maximum error in the adjusted frequency of the FT of the source strength signal due to uncertainty (expressed in percentage) on the source velocity. 91

Figure 5.15: FT of the original source strength signal (red) and the de-Dopplerized signal obtained from the microphone data (blue) for a monopole source moving along the x-direction at 50 m/s and emitting sound between 1000 Hz and 2000 Hz, <i>as the source moves from (0,0,0) to (24,0,0)</i> . Data processed using equal-length emission time windows of 0.04 seconds each.	93
Figure 5.16: FT of the original source strength signal (red) and the de-Dopplerized signal obtained from the microphone data (blue) for a monopole source moving along the x-direction at 50 m/s and emitting sound between 1000 Hz and 2000 Hz, <i>as the source moves from (24,0,0) to (48,0,0)</i> . Data processed using equal-length emission time windows of 0.04 seconds each.	94
Figure 5.17: Array pattern used for the numerical simulations.	95
Figure 5.18: Schematic of the data processing of the new method.	98
Figure 5.19: Acoustic maps of a monopole source radiating sound at 1000 Hz, moving in the x-direction at 50 m/s obtained with a) Time Domain beamforming, and b) Frequency domain beamforming for source strength estimation.	99
Figure 5.20: Acoustic maps of a monopole source radiating sound at 2500 Hz, rotating around the z-axis in the z=0 plane at 600 rpm, obtained with a) Time domain beamforming, and b) Frequency domain beamforming.	100
Figure 5.21: Emission angle range for data processing of a monopole source moving at various velocities.	102
Figure 5.22: Acoustic maps for a monopole source emitting sound at 1000 Hz moving along the x-direction with velocities of: a) 50 m/s, b) 100 m/s, c) 150 m/s, d) 200 m/s, e) 250 m/s, and f) 300 m/s. All maps were processed using constant time windows of 0.02 sec. (6 dB cutoff).	104
Figure 5.23: Acoustic maps for a monopole source emitting sound at 1000 Hz moving along the x-direction with velocities of: a) 50 m/s, b) 100 m/s, c) 150 m/s, d) 200 m/s, e) 250 m/s, and f) 300 m/s. All maps were processed using constant time windows of 0.02 sec with no overlap. (10 dB cutoff).	105

Figure 5.24: Acoustic maps for a monopole source emitting sound at 1000 Hz moving along the x-direction with velocities of: a) 250 m/s, and b) 300 m/s. Both maps were processed using constant time windows of 0.02 sec with 50% overlap. (10 dB cutoff).....	106
Figure 5.25: Acoustic maps for a monopole source moving along the x-direction at 50 m/s emitting sound at: a) 1000 Hz, b) 1600 Hz, c) 2500 Hz, and b) 4000 Hz.....	108
Figure 5.26: Beamwidth of the acoustic maps of a monopole source with linear motion emitting sound at various frequencies obtained using the new frequency domain beamforming method.	109
Figure 5.27: Source position segments for various emission angles ϕ	110
Figure 5.28: Acoustic maps showing the spot-size (3 dB down from the main-lobe peak) for the various source position segments shown in Figure 5.27.	111
Figure 5.29: Fourier Transform of the first microphone of the array, and the corresponding acoustic map showing the effect of uncorrelated noise in the array microphones for various levels of noise	113
Figure 5.30: Acoustic maps for two monopole sources: a) Correlated sources emitting sound at 1000 Hz located at (3,3,0) and (3,-3,0), and b) Uncorrelated sources emitting sound at 1000 Hz (3,3,0) and at 1100 Hz (3,-3,0).	114
Figure 5.31: Acoustic maps for three monopole sources: a) Correlated sources emitting sound at 1000 Hz located at (-1,0,0), (3,3,0) and (3,-3,0), and b) Uncorrelated sources emitting sound at 1000 Hz (-1,0,0), 1050 Hz (3,3,0), and at 1100 Hz (3,-3,0).....	115
Figure 5.32: Processing time required to complete the computation of the beamforming output over a given scanning grid using the traditional time domain beamforming method and the new frequency domain beamforming method. For all the cases, a time window of 0.4 seconds was used.....	116

Chapter 1

Introduction

Technological developments of aerodynamic machines enabled the construction of faster and larger airplanes, alternative sources of energy such as wind turbines, and more efficient turbomachinery, just to mention a few. However, as these machines interact with the surrounding air they also generate undesirable noise. Furthermore, most of these noise sources are not static, i.e., they have time dependent position. At the same time, increased concern in noise pollution has derived in stringent laws and regulations regarding the noise emission levels of these machines. Therefore, there is a need to reduce the noise radiated by aerodynamic machines.

Efficient noise control solutions require identification of the dominant noise sources. Noise Source Identification (NSID) involves the identification of the spatial location as well as the frequency content of the dominant noise sources. These tasks are achieved using microphone phased arrays (MPAs). The application and further development of MPAs to perform aeroacoustic measurements has been largely made in the aeronautical field to identify aircraft noise sources. Of particular interest is the noise emitted by airplanes during take-off and landing.

Microphone phased arrays are also used in the locomotive field to identify different sources of sound such as wheel/rail interaction noise and aeroacoustic noise. In the wind turbine industry MPAs are used to identify the various noise mechanisms like incoming turbulence-leading edge interaction, turbulent boundary layer-trailing edge interaction, tip vortex noise, rotor wake-tower interaction, and nacelle noise.

Data collected by the array is processed by applying phase delays to the signal received by each microphone to focus or to steer the array to a particular point or in a specific direction, respectively. This data processing is also known as beamforming, and is used to locate sources of sound on an assumed source space.

Beamforming can be performed in the time domain or in the frequency domain. However, frequency domain beamforming is the preferred approach due to the availability of many advanced optimization techniques, such as diagonal removal, that improve significantly the beamforming output. Frequency domain beamforming is also a more computationally efficient technique than time domain beamforming.

Nevertheless, in spite of its more computationally intensive requirements and the lack of advanced optimization methods, time domain beamforming is the only currently available technique to identify moving sources of sound.

1.1 Literature Review

One of the earliest work reporting a technique to restore non-stationary signals from moving sound sources into stationary signals was presented by Verhas [1]. This technique was used to locate moving sources of sound with an array of microphones in 1985 by Howell *et al.* [2]. The technique to restore non-stationary signals removed the Doppler effect of time compression and expansion of the acoustic signal caused by source motion. The technique consisted of calculating an average source strength signal using the signals recorded by the microphones of the array. This calculation involved the interpolation of every data point at equally spaced intervals of time to remove the Doppler effect. During the averaging process of the computed source strength signals, if the assumed source position coincided with an actual source position, the sum of the signals reinforced, otherwise the sum diminished. This procedure was repeated for various assumed source positions, allowing the construction of one-dimensional acoustic images.

Howell's technique was used in 1988 by Bariskow and King [3] to investigate the sound generated by high-speed trains. The main purpose of that study was to locate all important sources of sound, and to analyze narrow band spectra to infer on the noise radiation mechanisms. To this end, Bariskow used a linear array of 15 microphones equally spaced 0.08-m apart, to collect data from trains passing by at 220 km/h. Processing of these data allowed the isolation of wheel/rail interaction noise.

Another significant step in NSID of moving sources of sound using microphone arrays was the transition from 1-D arrays to 2-D arrays that took place in the mid 1990s. First, simple cross-arrays were used for acoustic measurements [4,5]. Among the early studies reporting the use of 2-D arrays for NSID is the work of Bariskow in 1995 [5]. To locate sources of sound on railway trains, Bariskow used various configurations of microphone arrays. These configurations included horizontal and vertical linear arrays, and a cross array (x-array). With this array he located wheel/rail interaction noise and also aeroacoustic noise generated by the horns. Later more elaborate logarithmic spiral and multi-arm logarithmic spiral arrays were developed [6-8]. Two dimensional arrays have the ability to resolve the source location in two dimensions and allow the construction of 2-D acoustic maps.

Two dimensional arrays were also used in aeronautical applications. In 1998 Michel *et al.* [9] used a 2-D sparse array provided with 111 microphones to perform over 170 measurements on landing aircraft at Frankfurt/Main airport. The main goal of the study was the identification of the loudest noise source which should be controlled in order to reduce sound radiation levels. Processing of these data in the time domain allowed the identification of various known sources, i.e., landing gear, flap, and slat noise sources. Also, a loud source on the outer part of the wing of some airplanes was apparent which was attributed to the wake-vortex wing interaction.

The importance of the array parameters such as the array dimension and the spacing between microphones was reported by Piet *et al.* in 1999 [10,11] by comparing the performance of x-arrays and a sparse 2-D array to perform flyover measurements of an Airbus A340. The study showed the need of nested arrays for source location on a large frequency range. It was also concluded that phased arrays are a good tool for qualitative source location. However, quantitative information requires a perfect estimation of all the effects involved (source, propagation, microphone characteristics, etc.).

Phased arrays have also been used in wind tunnels to identify airframe noise sources [12-16], and noise from wind turbine blades [17-19]. In 2003, Stoker *et al.* [12] presented the results of a flyover test of a Boeing 777 using time domain beamforming, and then compared these results with those obtained in wind tunnel tests using scale models. Although the results from

both tests presented many similarities, there were also some major differences. The scale model tests show a significant noise source located at the leading edge, whereas the full scale flyover test showed almost no noise being radiated from the leading edge. Conversely, the flyover test revealed sources that were not present in the scale models. These sources were attributed to small details that were not reproduced in the scale models.

The next significant step in NSID of moving sound sources was the implementation of phased array technology to locate rotating sources of sound. This implementation was performed by Sijtsma and Oerlemans in 2001 [20]. Based on the work of Howell *et al.* [1] and Bariskow [2] a radiation model of a moving monopole source was implemented into a time domain beamforming algorithm, which they called Rotating Source Identifier (ROSI), to locate sources with rotational motion, i.e. moving along a circular trajectory. The ROSI algorithm consisted of first de-Dopplerizing the signals recorded by each microphone and then applying a delay-and-sum beamforming algorithm to reconstruct the source strength of the source at the assumed position.

In 2005 Oerlemans and Mendez [21] used a 15-m x 18-m horizontally mounted phased array to perform areroacoustic measurements of a full scale 3-blade wind turbine with a rotor diameter of 58 meters installed on a tower of 53.5 meters height. To identify the sound generation mechanisms, one blade was cleaned, the second blade was tripped, and the third blade was left untreated. The data was processed with a conventional beamforming algorithm and with the ROSI algorithm. Conventional beamforming showed that practically all noise is radiated during the downward movement of the blades. When the ROSI algorithm was used, the following restraints were applied: 1) Data with more than 8% variation in rpm was discarded, and 2) only the data corresponding to the first half rotation was processed. The resolution of the acoustic maps obtained with the ROSI algorithm, i.e. time domain beamforming, was not sufficient to identify if the noise is radiated by the leading-edge or by the trailing-edge of the blades. However, the acoustic maps for the tripped blade showed higher sound levels than the maps of the clean and the untreated blades. In 2006, Oerlemans *et al.* [22] explained that convective amplification and trailing edge directivity were responsible for the higher sound

levels radiated during the downward movement (blades moving towards the array) than in the upward movement (blades moving away from the array).

1.2 Motivation

As seen in the previous section, up to date no work has been reported where NSID of moving sources of sound is performed using a frequency domain beamforming algorithm. In this context, the motivation for this dissertation is twofold: From an academic point of view, to fill the gap left by the lack of a frequency domain beamforming method to locate moving sound sources. From a practical point of view, to develop an alternative approach to time domain beamforming for NSID of moving sources of sound that is computationally more efficient. This alternative approach will complement time domain beamforming which is the only currently available method for NSI of moving sources of sound.

1.3 Objectives

The three main objectives of this dissertation are:

1. To develop the mathematical formulation of a new technique that removes the Doppler effect from the microphone signals operating entirely in the frequency domain without the need to resample and interpolate the microphone signals
2. To develop a frequency domain beamforming algorithm to locate sources of sound in a moving reference frame, based on the new de-Dopplerization technique.
3. To conduct numerical simulations for the following two types of source motion that have practical applications: a) Sources moving along a linear trajectory (e.g. automotive, locomotive and aeronautical applications), and b) sources moving along a circular trajectory (e.g. wind turbine noise, helicopter rotor blade noise and fan noise applications). These simulations will consider several source configurations (e.g. emission frequency, signal-to-noise ratio, and source velocity), and various processing parameters (e.g. data block length, number of data blocks, and windowing). Then, use the results from these numerical simulations to identify the strengths and limitations of the new frequency domain beamforming method for moving sources of sound.

1.4 Dissertation Organization

The organization of this dissertation is as follows. Chapter 2 presents the mathematical formulation of the acoustic field of a moving source of sound, and discusses how the motion of the source affects the acoustic pressure perceived by a stationary observer, i.e., the Doppler effect.

Chapter 3 presents a summary of the currently available beamforming methods to identify sound sources. The two methods discussed are time domain beamforming for stationary and moving sources of sound, and frequency domain beamforming for stationary sound sources.

The mathematical formulation of the new frequency domain beamforming method to locate moving sources of sound is presented in Chapter 4. This Chapter presents first the derivation of a new de-Dopplerization technique in the frequency domain that is based on the translation and scaling properties of the Fourier Transform. Then, the de-Dopplerization technique is implemented into a frequency domain beamforming algorithm. Two cases of source motion are considered in this chapter: sources moving along a linear trajectory, and sources moving along a circular trajectory.

Chapter 5 describes the details of the numerical simulations performed to validate the new frequency domain beamforming method. Then, the results from these numerical simulations are used to assess the strengths and limitations of the new frequency domain beamforming method as compared to the traditional time domain beamforming method.

Chapter 6 discusses the most relevant conclusions drawn from this work. This chapter also suggests the focus for future work.

Appendix A contains the step-by-step derivation of some of the equations presented throughout the dissertation. This appendix is presented for the readers interested in the mathematical derivations without interrupting the flow of the presentation of the material.

Chapter 2

Acoustic Field of Monopole Sources of Sound

This chapter introduces the mathematical formulation of the acoustic field of a monopole point source of sound. First, the solution of the inhomogeneous wave equation for a fixed monopole source is presented. Then, this solution is extended for the case of a moving monopole source. The effect of the source motion on its radiated sound field is explained for the case a source with linear motion and for the case of a source with constant angular motion. Then, the most frequently used de-Dopplerization technique is presented along with a discussion of signal processing issues involved with this technique.

2.1 Acoustic Field of a Fixed Monopole Source

The derivation here is based on the work by Dowling and Ffowcs Williams [23]. The acoustic field produced by a distribution of fixed sources of sound is governed by the inhomogeneous wave equation,

$$\frac{1}{c^2} \frac{\partial^2 p(\vec{x}, t)}{\partial t^2} - \nabla^2 p(\vec{x}, t) = q(\vec{x}, t) \quad (2.1)$$

where $p(\vec{x}, t)$ is the acoustic pressure, $q(\vec{x}, t)$ is the source function, \vec{x} is the vector of spatial coordinates, t is the time variable, and c is the speed of sound. The coordinate system used here is Cartesian with the orthogonal directions referred by the indices 1, 2, and 3, respectively. If needed, the unit vectors are noted as \vec{e}_ℓ $\ell = 1, 2, 3$.

An expression for the acoustic pressure that satisfies equation (2.1) can be obtained using the Green's function method. This method allows writing the solution of equation (2.1) in terms of a Green's function as,

$$p(\vec{x}, t) = \int_{-\infty}^{\infty} \int_V q(\vec{y}, \tau) G(\vec{x}, t | \vec{y}, \tau) d^3y d\tau \quad (2.2)$$

In equation (2.2), G is the free-field Green's function which is the solution of the wave equation for an impulsive point source located at point \vec{y} that emits a sound pulse at time t_s . The spatial integration is over a volume, V , enclosing the source. Thus, the Green's function satisfies the following equation,

$$\frac{1}{c^2} \frac{\partial^2 G(\vec{x}, t | \vec{y}, t_s)}{\partial t^2} - \nabla^2 G(\vec{x}, t | \vec{y}, t_s) = \delta(\vec{x} - \vec{y}) \delta(t - t_s) \quad (2.3)$$

Solution of equation (2.3) for the impulsive point source in an unbounded region yields the free-field Green's function [24],

$$G(\vec{x}, t | \vec{y}, t_s) = \frac{\delta(t - t_s - r/c)}{4\pi r} \quad (2.4)$$

where r is the distance between the source and the observer locations given as

$$r = |\vec{x} - \vec{y}| \quad (2.5)$$

Substitution of equation (2.4) into equation (2.2) yields

$$p(\vec{x}, t) = \int_{-\infty}^{\infty} \int_V q(\vec{y}, t_s) \frac{\delta(t - t_s - |\vec{x} - \vec{y}|/c)}{4\pi |\vec{x} - \vec{y}|} d^3\vec{y} dt_s \quad (2.6)$$

Evaluation of the time integral in equation (2.6) can be performed using the “sifting” property of δ functions (see Appendix A1.1). Thus, obtaining an expression for the acoustic pressure induced by the source distribution, given by

$$p(\vec{x}, t) = \int_V \frac{q(\vec{y}, t - |\vec{x} - \vec{y}|/c)}{4\pi|\vec{x} - \vec{y}|} d^3\vec{y} = \int_V \frac{q(\vec{y}, \tau)}{4\pi|\vec{x} - \vec{y}|} d^3\vec{y}. \quad (2.7)$$

Figure 2.1 shows a schematic representation of a source field and the sound field it induces. As seen from this figure, the acoustic pressure perceived by an observer located at \vec{x} is obtained by integration over the source field of the source function of an elemental source at \vec{y} normalized by the distance from the elemental source to the observer. The variable τ represents the time at which the sound was emitted and is, thus, known as the emission time. It is given as

$$\tau = \frac{t - |\vec{x} - \vec{y}|}{c}. \quad (2.8)$$

Consequently, the difference $t - \tau = |\vec{x} - \vec{y}|/c$ accounts for the time required for the sound to travel from \vec{y} to \vec{x} and it is called the propagation time. Therefore, we have an emission time τ , arrival or reception time t , and propagation time $t - \tau = |\vec{x} - \vec{y}|/c$.

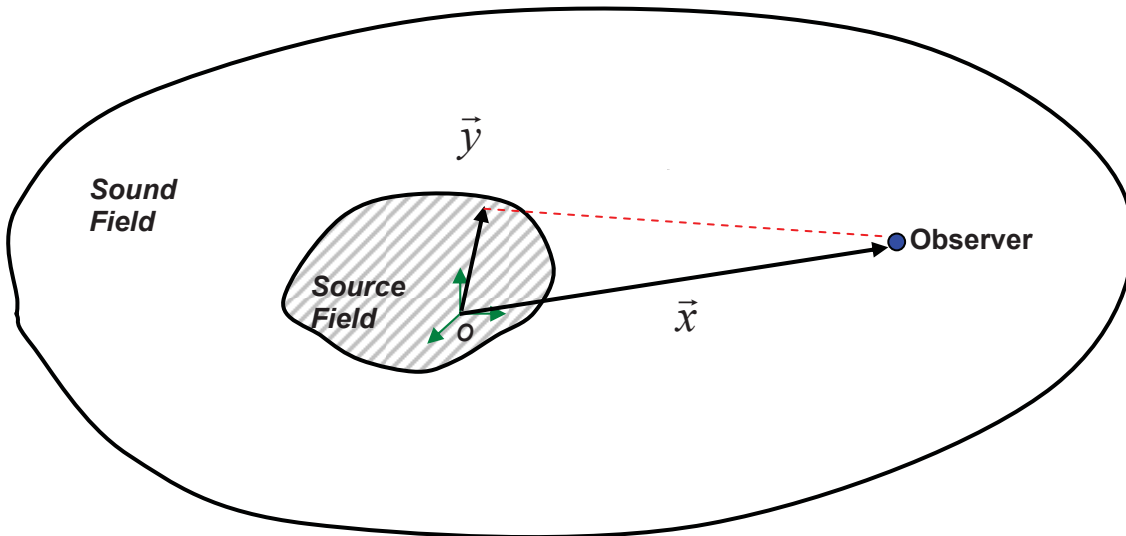


Figure 2.1: Schematic representation of a source field and the sound field induced by this source.

If the source is acoustically compact (e.g. source dimensions are small compared to the wavelength of the emitted sound), the source can be considered a point source, i.e., monopole source. In this case, the propagation times from different parts of the source to the observer are essentially the same. The source function for the compact source located at \bar{x}_s becomes:

$$q(\bar{x}, t) = q(t) \delta(\bar{y} - \bar{x}_s) \quad (2.9)$$

where $q(t)$ is called the monopole source strength. Substitution of equation (2.9) into equation (2.7) yields

$$p(\bar{x}, t) = \int_V \frac{q(t - |\bar{x} - \bar{y}|/c) \delta(\bar{y} - \bar{x}_s)}{4\pi |\bar{x} - \bar{y}|} d^3y. \quad (2.10)$$

Evaluation of the integral of equation (2.10) results in

$$p(\bar{x}, t) = \frac{q(t - |\bar{x} - \bar{x}_s|/c)}{4\pi |\bar{x} - \bar{x}_s|}, \quad (2.11)$$

which is the expression for the acoustic pressure induced by a stationary monopole source in free field.

2.2 Acoustic Field of a Moving Monopole Source

To find an expression for the acoustic pressure induced by a moving monopole source with time dependent position $\bar{x}_s(t)$, the source function can be written as

$$q(\bar{x}, t) = q(t) \delta(\bar{y} - \bar{x}_s(t)) \quad (2.12)$$

Substitution of equation (2.12) into equation (2.6) yields an expression for the acoustic pressure induced by this moving monopole source,

$$p(\vec{x}, t) = \int_{-\infty}^{\infty} \int_V \frac{q(t_s) \delta(\vec{y} - \vec{x}_s(t_s)) \delta(t - t_s - |\vec{x} - \vec{y}|/c)}{4\pi |\vec{x} - \vec{y}|} d^3\vec{y} dt_s. \quad (2.13)$$

Evaluation of the spatial integral yields,

$$p(\vec{x}, t) = \int_{-\infty}^{\infty} \frac{q(t_s) \delta(t - t_s - |\vec{x} - \vec{x}_s(t_s)|/c)}{4\pi |\vec{x} - \vec{x}_s(t_s)|} dt_s. \quad (2.14)$$

Since the argument of the Delta function is a function of t_s , the evaluation of the time integral is now more complicated. To this end, the Delta function must be re-expressed as

$$\delta[g(t_s)] = \sum_i \frac{\delta(t_s - \tau_i)}{\left| \frac{dg(t_s)}{dt_s} \right|_{t_s=\tau_i}} \quad (2.15)$$

where τ_i are the roots of the argument, e.g. $g(\tau_i) = 0$ [25]. The summation is over the number of physically meaningful roots, e.g. assuming there are more than one non-spurious root. Here the function $g(t_s)$ is

$$g(t_s) = t - t_s - \frac{|\vec{x} - \vec{x}_s(t_s)|}{c} \quad (2.16)$$

The derivative of equation (2.16) with respect to t_s is given by (see Appendix A2.1)

$$\left| \frac{dg(t_s)}{dt_s} \right| = |1 - M_{so}(t_s)| \quad (2.17)$$

where M_{so} is the component of the source velocity \vec{v} (in Mach) in the source-to-observer direction. That is,

$$M_{so}(t_s) = \frac{1}{c} \frac{(\vec{x} - \vec{x}_s(t_s))}{|\vec{x} - \vec{x}_s(t_s)|} \cdot \vec{v} \quad (2.18)$$

Substitution of equations (2.16) and (2.17) expressed in the form of equation (2.15) into equation (2.14) yields

$$p(\vec{x}, t) = \int_{-\infty}^{\infty} \frac{q(t_s)}{4\pi |\vec{x} - \vec{x}_s(t_s)|} \sum_i \frac{\delta(t_s - \tau_i)}{|1 - M_{so}(t_s)|} dt_s. \quad (2.19)$$

Evaluation of the integral in equation (2.14) is now straight forward, yielding

$$p(\vec{x}, t) = \sum_i \frac{q(\tau_i)}{4\pi |\vec{x} - \vec{x}_s(\tau_i)| |1 - M_{so}(\tau_i)|}, \quad (2.20)$$

where τ_i is obtained as the solution of

$$t - \tau_i = |\vec{x} - \vec{x}_s(\tau_i)| / c. \quad (2.21)$$

That is the roots of equation (2.21). Note that the summation in equation (2.20) should only include physically meaningful roots.

For subsonic motion, the term $|1 - M_{so}(\tau_i)|$ in equation (2.20) represents an amplification factor of the sound produced by the source motion. This effect is known as the Doppler amplification.

So far, equation (2.20) has been derived from a purely mathematical approach. In this equation, the source strength, $q(\tau_i)$, and source position, $\vec{x}_s(\tau_i)$, are defined in terms of the

emission time, τ while the pressure at the observer location is given in the reception time, t . To describe the physical significance of the various variables involved in equation (2.20), the case of linear and rotational motion of the source will be investigated.

2.2.1 Linear Motion

Consider a source of sound moving in a linear trajectory with constant velocity U . For simplicity, it is assumed to move along the 1-direction, $\vec{v}_s = U\vec{e}_1$, as shown in

Figure 2.2. The positions of the source and of the observer are defined by the fixed reference system shown. The source is assumed to radiate as a monopole. To analyze this situation, both the emission time, τ , and the reception time, t , when the sound arrives at the observer need to be tracked.

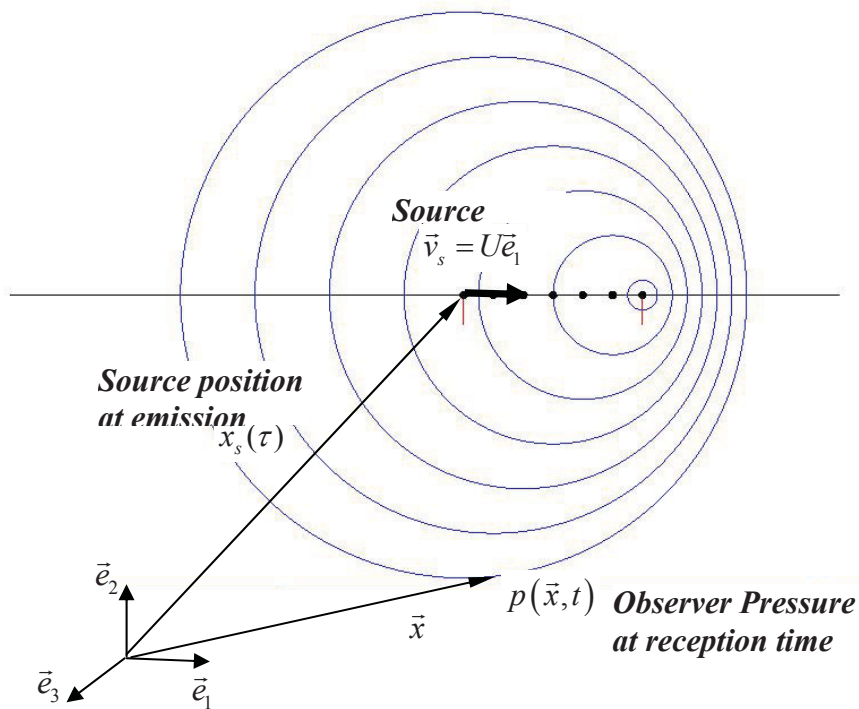


Figure 2.2: Sound perceived by a stationary observer from a source of sound moving in a linear path at constant speed.

To compute the Doppler amplification factor $|1 - M_{so}(\tau)|$, the velocity in the direction of the source-to-observer can be computed by the inner product of the unit vector in the source-to-observer direction (at the emission time) and the source velocity (see Figure 2.3). That is:

$$|1 - M_{so}(\tau)| = \left| 1 - \frac{\vec{x} - \vec{x}_s(\tau)}{|\vec{x} - \vec{x}_s(\tau)|} \cdot \frac{\vec{v}_s}{c} \right|. \quad (2.22)$$

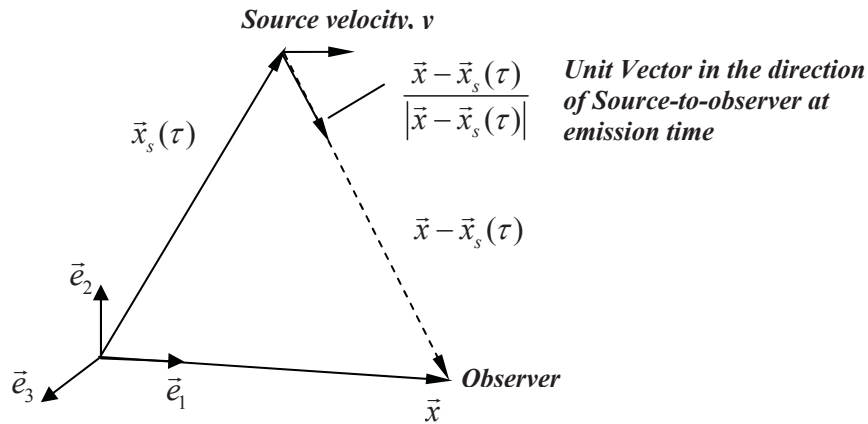


Figure 2.3: Component of the source velocity in the direction of source-to-observer at emission time.

In addition to the Doppler amplification, there is a second, more important effect on the level and frequency content of the sound due to the motion of the source. This is illustrated in Figure 2.4. This effect has been explained by previous researchers such as Dowling and Ffowcs Williams (1983) and Howell et.al. (1986). In this figure, the source emits sound pulses at equally spaced intervals of time, $\Delta\tau$, between an initial time τ_i and final time τ_f . These pulses of sound are recorded by three fixed microphones m_1 , m_2 , and m_3 . Without loss of generality, these microphones are assumed to be placed directly underneath the source path, e.g. 2-D problem.

The relative motion between the source and each of these microphones is obviously different. For microphone m_1 , as the source moves between time τ_i and time τ_f , it gets further away from microphone m_1 . Thus, the sound for subsequent pulses has to travel a longer distance

as the previous one. Therefore, the sound pulses emitted at regular time intervals, $\Delta\tau$, will be arriving to m_1 spaced at increasingly larger time intervals and lower levels as shown in Figure 2.4. For microphone m_3 , the opposite situation occurs since the source moves closer as time progresses from τ_i to τ_f . The spacing between pulses recorded by this microphone decreases. For microphone m_2 , at first the source approaches this microphone location, then it passes overhead, and finally it moves further away. Consequently, the sound pulses arrive at decreasing time intervals while approaching, and at increasing time intervals while receding. The main implication of this behavior is that the frequency content of the sound source is distorted depending on the location of the observer relative to the source. Assuming the source radiate harmonically at frequency ω , microphone m_1 will perceive a lower frequency since the signal is spread out while microphone m_3 will perceive a higher frequency.

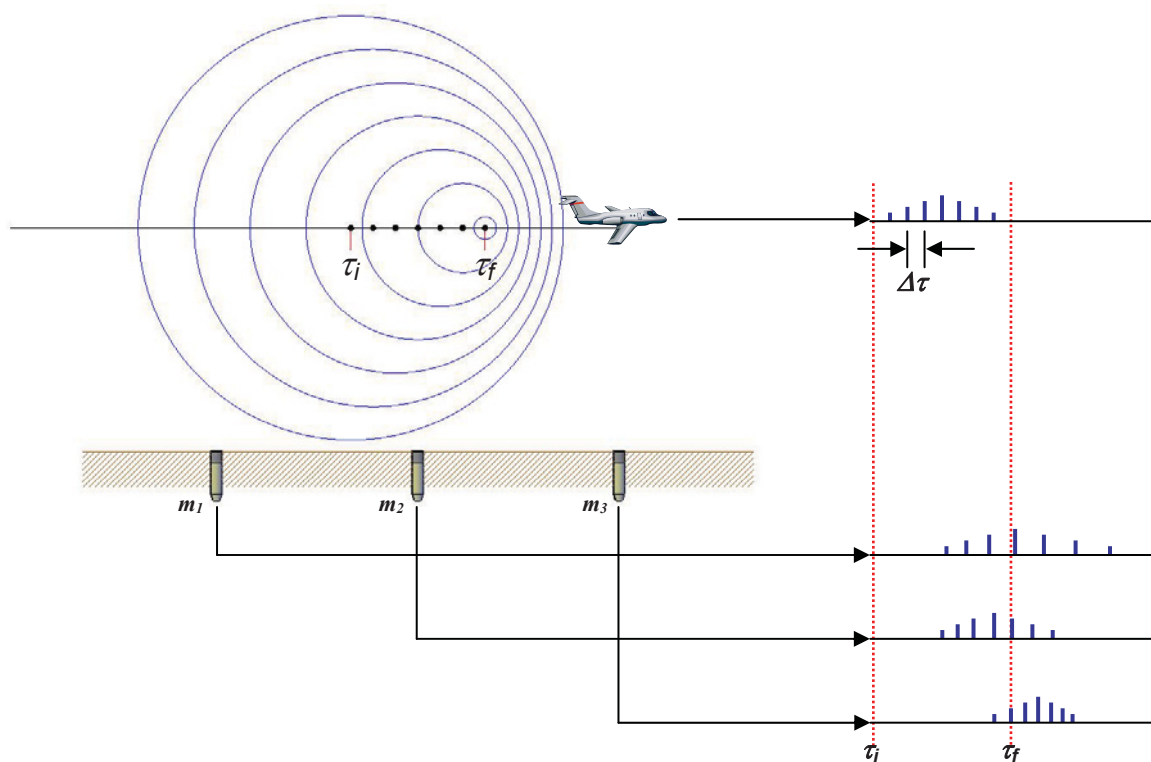


Figure 2.4: Effect of source motion on the acoustic field.

To further gain insight, the propagation time for the case of linear motion at constant speed U is shown using Figure 2.5. Assuming that at $\tau = 0$ the source is at the origin of the coordinate system $\vec{x}_s(0) = 0\vec{e}_1$, the propagation time is given as

$$t - \tau = \frac{|\vec{x} - \vec{x}_s(\tau)|}{c} = \frac{\sqrt{(x_1 - U\tau)^2 + x_2^2 + x_3^2}}{c}. \quad (2.23)$$

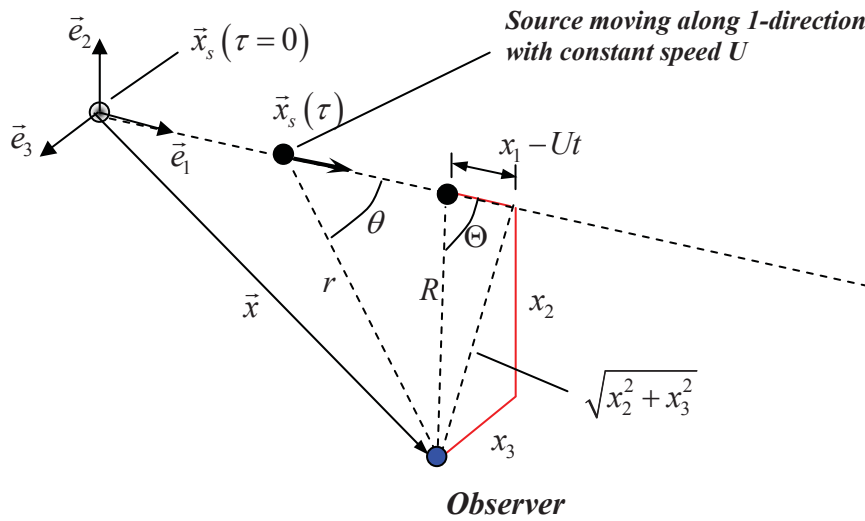


Figure 2.5: Monopole in linear constant speed motion.

As presented by Dowling and Ffowcs Williams [23], the emission time, τ , for a given reception time, t , can be explicitly obtained by squaring equation (2.21) and solving for the roots. That is,

$$\tau = \frac{ct - Mx_1 \pm \sqrt{(x_1 - Ut)^2 + (1 - M^2)(x_2^2 + x_3^2)}}{c(1 - M^2)}, \quad (2.24)$$

where M is the source speed in Mach, i.e. $M = U/c$.

Equation (2.24) shows that there are two solutions to the emission time, τ , for a given reception time, t . However, the negative value for the square root term leads to the only valid solution, e.g. $t > \tau$. The other is a spurious root and must be excluded.

Equation (2.24) yields the emission time, τ , for a given reception time, t , based on knowledge of the source position at the emission time, $\vec{x}_s(\tau)$. It should be noted that in practice, the position of the source at the emission time is known in microphone phased array measurements.

Though not useful for the issue addressed in this dissertation, the inverse problem of computing the emission time τ in terms of the reception time t and the knowledge of the source position at the reception time $\vec{x}_s(t)$ can be solved in a straight forward manner.

In Figure 2.5, the distance between the source position at reception time, $\vec{x}_s(t)$, and the observer position, \vec{x} , is referred to as R , and it is given by

$$R = |\vec{x} - \vec{x}_s(t)| = \sqrt{(x_1 - Ut)^2 + x_2^2 + x_3^2}. \quad (2.25)$$

Figure 2.5 also shows that the angle between the direction of source motion, i.e., the 1-direction, and the source-to-observer direction when the source is at $\vec{x}_s(t)$ is termed Θ , and is given by

$$\Theta = \frac{x_1 - Ut}{R}. \quad (2.26)$$

The distance R and the angle Θ are based in the position of the source at receiver time. For this reason, R and Θ are also referred to as reception time coordinates.

Rewriting equations (2.20) and (2.21) in terms of reception time coordinates yields,

$$p(\vec{x}, t) = \frac{q(\tau)}{4\pi R \sqrt{1 - M^2 \sin^2 \Theta}}, \quad (2.27)$$

where the emission time τ is given by

$$\tau = t - \left(\frac{RM \cos \Theta + R \sqrt{1 - M^2 \sin^2 \Theta}}{c(1 - M^2)} \right). \quad (2.28)$$

Reception time coordinates are coordinates in a reference frame that moves with the source. Therefore, in this reference frame, the distance R and the angle Θ are fixed, i.e., constant. Consequently, these coordinates are well suited for aeroacoustic wind tunnel testing where the source, i.e., the test model, and the observer, i.e., the microphone, are both stationary, and the air is convected past it.

2.2.2 Rotating Sources

It is also very illustrative to consider the case of a rotating source with constant angular speed, ω_r , as shown in Figure 2.6. For convenience, the stationary coordinate system is positioned at the center of rotation with directions 1 and 2 defining the plane of rotation. The source moves along a circular trajectory with radius R starting at $\vec{x}_s(\tau=0) = R\vec{e}_1$. Thus, the position of the source in terms of the emission time is $\vec{x}_s(\tau) = R \cos(\omega_r \tau) \vec{e}_1 + R \sin(\omega_r \tau) \vec{e}_2$. The source tangential velocity is assumed subsonic, i.e. $M_{tip} = \omega_r R / c < 1$. The source velocity vector is given by $\vec{v}_s(\tau) = -\omega_r R \sin(\omega_r \tau) \vec{e}_1 + \omega_r R \cos(\omega_r \tau) \vec{e}_2$.

Assume microphone m_l is located along the axes of rotation at a distance L from the plane of rotation, e.g. observer position $\vec{x} = L\vec{e}_3$. Therefore, at any instant of time, the distance between the rotating source and this microphone remains constant. The propagation time in this case is constant as

$$t - \tau = \frac{|\vec{x} - \vec{x}_s(\tau)|}{c} = \frac{\sqrt{(R \cos \omega_r \tau)^2 + (R \cos \omega_r \tau)^2 + L^2}}{c} = \frac{\sqrt{R^2 + L^2}}{c} \quad (2.29)$$

Thus, the signal from the source to this observer position is not affected by the source motion.

On the other hand, assuming microphone m_2 is located off the axis of rotation by a distance D , $\vec{x} = D\vec{e}_1 + L\vec{e}_3$, the propagation time is now a function of emission time, i.e. $\vec{x} - \vec{x}_s(\tau)$.

That is

$$\begin{aligned} t - \tau &= \frac{|\vec{x} - \vec{x}_s(\tau)|}{c} = \frac{\sqrt{(D - R \cos \omega_r \tau)^2 + (R \sin \omega_r \tau)^2 + L^2}}{c} \\ &= \frac{\sqrt{D^2 + R^2 + L^2 - 2DR \cos \omega_r \tau}}{c} \end{aligned} \quad (2.30)$$

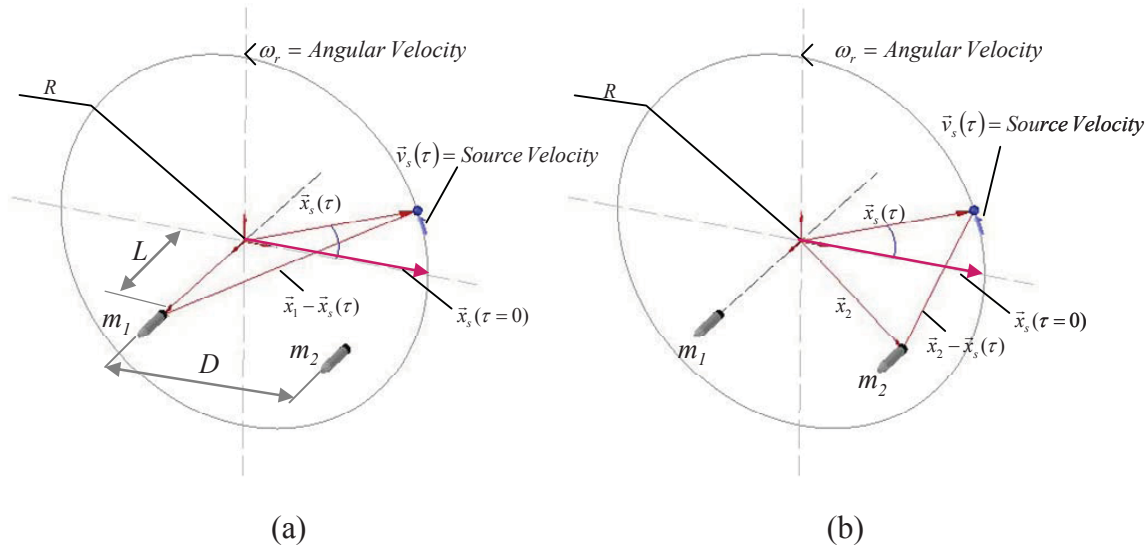


Figure 2.6: Monopole source moving in a circular trajectory. Position and velocity vectors with respect to (a) microphone m_1 , and (b) microphone m_2 .

Figure 2.7a illustrates the propagation time from the source to microphones m_1 and m_2 , whereas Figure 2.7b shows the acoustic pressure recorded by microphones m_1 and m_2 at equally

spaced intervals of observer time. The sampling frequency in this example is 25.6 kHz, e.g. $\Delta\tau = 1/25600 = 0.039$ msec, and the source is radiating harmonically at 500 Hz. From these figures, the effect of motion on the radiated sound is apparent. As expected, the propagation time for microphone m_1 is constant. On the other hand, the propagation time is not constant for microphone m_2 . As the source moves half a revolution from $\omega_r\tau = 0$ to $\omega_r\tau = \pi$, i.e. the source moves away from m_2 , the observed frequency is lower than the source frequency. On the other hand, when the source moves from $\omega_r\tau = \pi$ to $\omega_r\tau = 0$, i.e. the source moves towards m_2 , the observed frequency is higher than the source frequency. The effect of the Doppler amplification factor, $|1 - M_{so}(\tau)|$, becomes increasingly important as the microphone gets closer to the plane of rotation of the source.

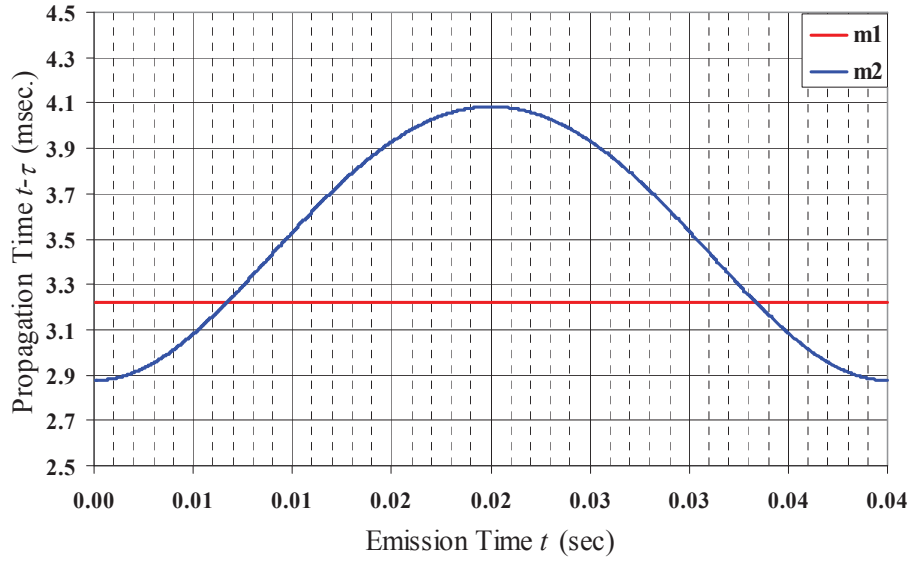
For this particular case, given any emission time τ and the corresponding source position $\vec{x}_s(\tau)$, equation (2.21) can be solved explicitly to yield the reception time t at which the sound arrives to the observer. However, the opposite is not true, i.e., given any observer time t , equation (2.21) cannot be solved explicitly to yield the emission time value τ at which the sound was emitted. Since equation (2.30) is a transcendental equation in τ , it can still be solved numerically. To this end, equation (2.30) is squared and after some mathematical manipulation leads to

$$c^2(t - \tau)^2 = |\vec{x}|^2 - 2DR \cos \omega_r\tau \quad (2.31)$$

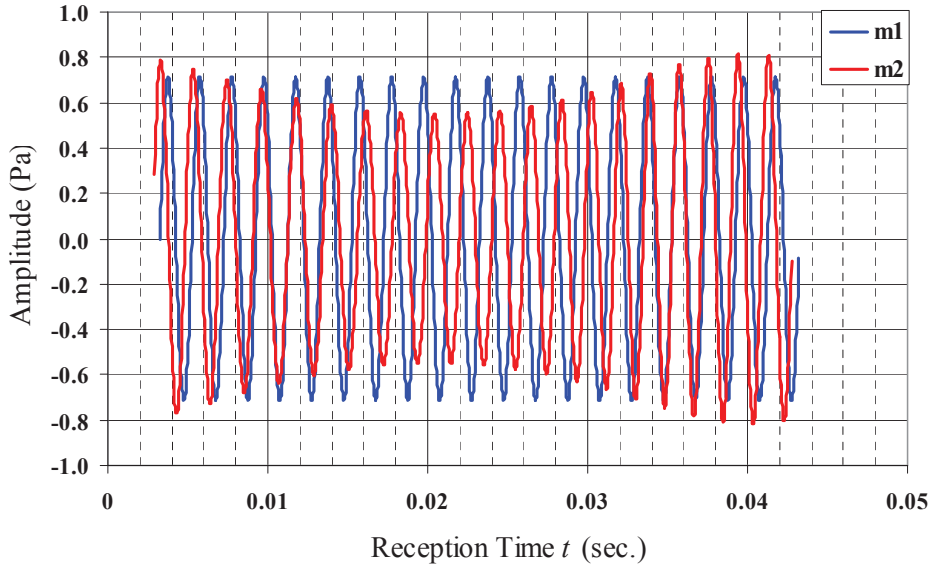
Figure 2.8 shows the right hand side and left hand side of the transcendental equation as a function of the emission time τ . The two roots are clearly shown in this figure. It also shows that there is only one valid root, e.g. the lower one where $\tau < t$.

An approximate approach to find a closed form solution to the emission time from the reception time is by expanding the cosine term in equation (2.31) in series as

$$\cos(\omega_r \tau) \approx 1 - \frac{(\omega_r \tau)^2}{2!} + \frac{(\omega_r \tau)^4}{4!} \dots \quad (2.32)$$



(a) Propagation time for microphones m_1 and m_2 .



(b) Amplitude of the signals recorded by m_1 and m_2 .

Figure 2.7: Effect of motion on the acoustic field of a monopole source - $\omega = 500 \times 2\pi \text{ rad/s}$, $\omega_r = 1500 \times 2\pi / 60 \text{ rad/s}$, $R=0.5 \text{ m}$, $L=1 \text{ m}$, $M_{tip} = \omega_r R / c = 0.22$.

However, this expansion is accurate only for small arguments $\omega_r \tau < \pi$ or half a revolution of the source if only few terms are used and probably not of much use. Another approach would be to find piecewise a closed form solution by assuming a linear motion of the source over equal intervals along a rotation.

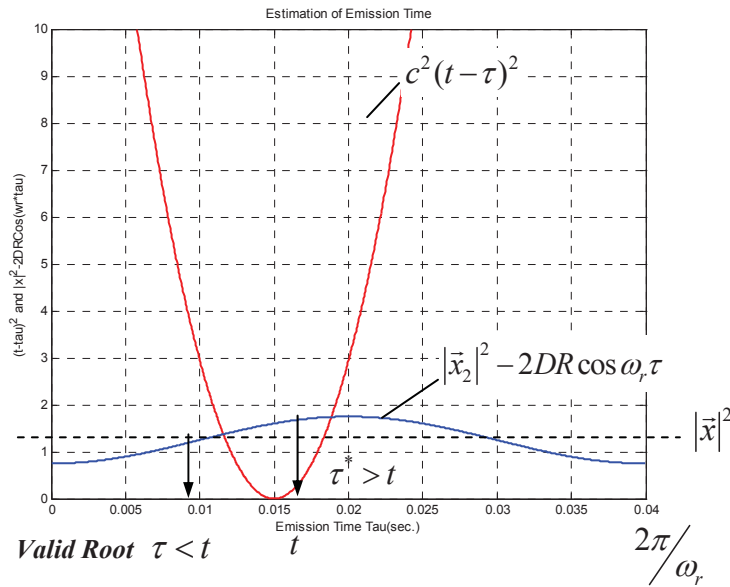


Figure 2.8: Schematic of the transcendental equation to find emission time from reception time for a rotating source.

It is interesting to note that the approach to compute the pressure at the microphones is trivial for any type of motion of the source. It basically involves assuming evenly spaced emission times and computing the pressure at the observer at the uneven reception time intervals. However, in practice one has the microphone data recorded at evenly spaced intervals of reception times, e.g. associated to the sampling frequency. Moreover, the position of the source is also known at the reception times. The inverse problem of solving the source strength time history, in terms of emission times, is more difficult since it requires to solve the transcendental equation (2.30) for τ . This issue will be revisited in the next chapter since it is central to the beamforming methods.

Therefore, it can be seen that the effect of motion on the acoustic field of a point monopole source is twofold:

- i) On the one hand, it compresses and/or expands the time between two consecutive wavefronts, i.e. it changes the frequency of the signal received at the observer location.
- ii) On the other hand, it changes the amplitude of the source signal received at the observer location due to both distance and the Doppler amplification factor $|1 - M_{so}(\tau)|$.

2.3 De-Dopplerization Technique

As explained in section 2.2, when a microphone samples the acoustic field of a moving source of sound, the data are distorted in amplitude and frequency. In this section, a technique to recover the original (undistorted) source signal is described. The objective of de-Dopplerization of the observer (microphone) signal is to remove the Doppler effects. It can be interpreted as seeking to estimate the source signal at the equal intervals of emission time. In other words, to estimate the signal at a reference observer position as it is moving with the source.

Figure 2.9 illustrates the de-Dopplerization concept for a source in linear motion. Note that the signal received by the observer, e.g. microphone, is sampled at equal time intervals, e.g. $\Delta t = 1/f_s$, where f_s is the sampling frequency. However, these reception time samples do not correspond to equal spacing of emission times, i.e. $\tau_j - \tau_{j-1} \neq \Delta t$. Conversely, equal spacing of the emission times, $\Delta \tau$, do not correspond to equal spacing of the reception times, $t_j - t_{j-1} \neq \Delta \tau$. This implies that in order to compute the de-Dopplerized signal p_d at equal time intervals, either the original (Dopplerized) microphone signals, or the computed (de-Dopplerized) microphone signals will need to be interpolated as shown later.

The conventional approach is to estimate the sound from the source as measured by a microphone that moves with it at a reference position \vec{x}_{ref} , e.g. without the Doppler effects. The process requires estimation of the original source strength signal at the emission times $Q(\tau)$.

This can be accomplished using the relationship between emission, τ , and reception times, t . The next step is to then estimate the sound $p_d(\vec{x}_{ref}, \hat{t}_j)$ as measured by a microphone position at \vec{x}_{ref} (moving with the source) without Doppler effects at new reception times, \hat{t}_j , corresponding to the emission times, τ_j .

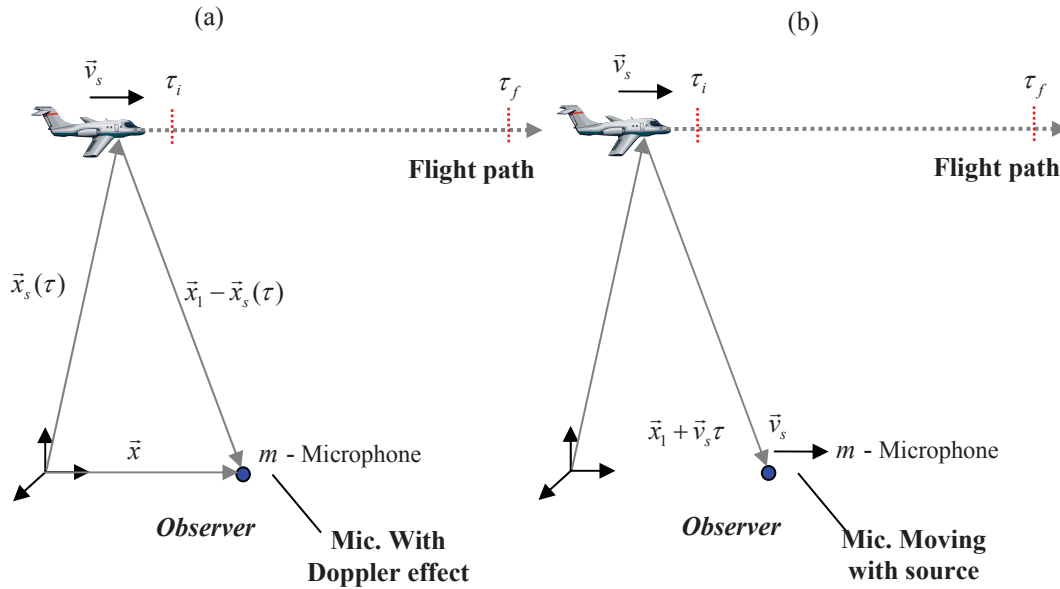


Figure 2.9: Physical interpretation of de-Dopplerization: (a) stationary microphone with signal affected by the Doppler effect and (b) microphone moving with the source (e.g. stationary relative to the source) with signal de-Dopplerized.

In practice, the source position and the microphone signals are sampled simultaneously. Let t_{sp} be the sampling time. Then, the signals sampled simultaneously are the source position $\vec{x}_s(t_{sp})$ and the microphone signals $p(\vec{x}, t_{sp})$ where $sp = 1, 2, \dots, N_{sp}$. The sampling time t_{sp} is the emission time if considered in the source (moving) reference frame. In the same manner, t_{sp} is the reception time if considered in the observer (stationary) reference frame.

Depending on whether the sampling time t_{sp} is treated as emission time (in the source reference frame), or as reception time (in the observer reference frame), there are two options to de-Dopplerize the microphone signals: a) In terms of emission time, and b) in terms of reception time.

2.3.1 De-Dopplerization in Terms of Emission Time

Since the de-Dopplerization process involves computation of the original source signal at emission times $q(\tau)$, the sampling time t_{sp} in this option will be treated as emission time τ ; in other words, $t_{sp} = \tau$. The source strength signal can be obtained from equation (2.20) where the microphone signals are in terms of reception times, $t_j, j = 1, 2, 3, \dots, J$. That is,

$$q(\tau_j) = p(\bar{x}, t_j) 4\pi |\bar{x} - \bar{x}_s(\tau_j)| |1 - M_{so}(\tau_j)|. \quad (2.33)$$

However as seen in Figure 10b, the actual sampled microphone signals are in terms of emission time $p(\bar{x}, \tau_j)$. Therefore, in order to obtain the microphone signal in terms of reception time, the following calculations are required. First, the reception time t_j corresponding to the emission time τ_j is computed using equation (2.21) as (see Figure 2.10a)

$$t_j = \tau_j + \frac{|\bar{x} - \bar{x}_s(\tau_j)|}{c}. \quad (2.34)$$

Then, the microphone signal required for equation (2.33) is obtained by shifting the sampled microphone signals by a delay equal to $|\bar{x} - \bar{x}_s(\tau_j)|/c$, i.e. $p(\bar{x}, \tau_j + |\bar{x} - \bar{x}_s(\tau_j)|/c)$. It is generally the case that the microphone signal at the required reception time t_j will not coincide with a sampled microphone signal data point, as shown in Figure 2.10b. Therefore, $p(\bar{x}, \tau_j + |\bar{x} - \bar{x}_s(\tau_j)|/c)$ needs to be approximated by interpolation using the most immediate sample points as $p(\bar{x}, \tau_j + |\bar{x} - \bar{x}_s(\tau_j)|/c) \approx \tilde{p}(\bar{x}, t_j)$, where the “ \sim ” denotes that the microphone signal was obtained using interpolation. Figure 2.10 shows the sampled data points marked with an “x”, whereas the interpolated values are marked with an “o”.

Knowing the microphone signal at reception time $\tilde{p}(\vec{x}, t_j)$, the source strength can then be obtained as (see Figure 2.10c)

$$q(\tau_j) \approx \tilde{p}(\vec{x}, t_j) 4 \pi |\vec{x} - \vec{x}_s(\tau_j)| |1 - M_{so}(\tau_j)| \quad (2.35)$$

Using the computed source strength signal, the pressure at any reference observer position, \vec{x}_{ref} , assuming the reference observer is moving with the source, is simply computed as

$$p_d(\vec{x}_{ref}, \hat{t}_j) = \frac{q(\tau_j)}{4 \pi |\vec{x}_{ref} - \vec{x}_s|}, \quad (2.36)$$

where the reception time \hat{t}_j is computed as

$$\hat{t}_j = \tau_j + \frac{|\vec{x}_{ref} - \vec{x}_s|}{c}. \quad (2.37)$$

Finally, the De-Dopplerized microphone signal is

$$p_d(\vec{x}_{ref}, t_j) = \frac{\tilde{p}(\vec{x}, t_j) 4 \pi |\vec{x} - \vec{x}_s(\tau_j)| |1 - M_{so}(\tau_j)|}{4 \pi |\vec{x}_{ref} - \vec{x}_s|} = \tilde{p}(\vec{x}, t_j) \frac{|\vec{x} - \vec{x}_s(\tau_j)|}{|\vec{x}_{ref} - \vec{x}_s|} |1 - M_{so}(\tau_j)| \quad (2.38)$$

Figure 2.10a through Figure 2.10d show the steps required to de-Dopplerize the microphone signal for data point $t_{sp} = \tau_j$ assuming the sampled data are given in terms of emission time. Similarly, Figure 2.10e through Figure 2.10h show the steps required to de-Dopplerize the microphone signal for data point $t_{sp} = \tau_{j+1}$.

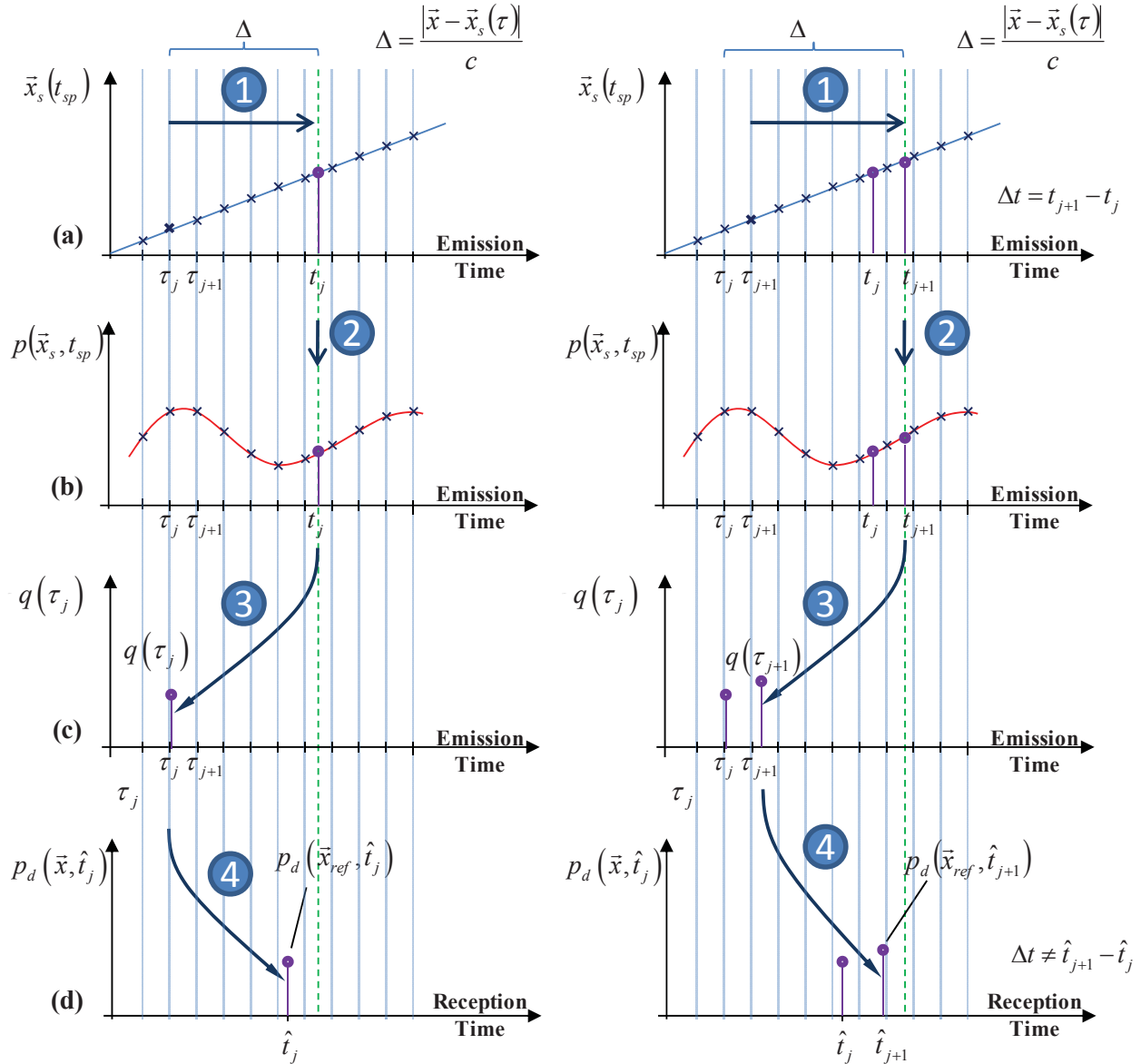


Figure 2.10: Steps involved in the de-Dopplerization of the signal in terms of emission time: (a) original source position, and (b) original microphone signal measured at equal interval of emission times, (c) estimated source strength signal at emission times, and (d) estimated sound signal at reference observer position.

2.3.2 De-Dopplerization in Terms of Reception Time

In this option, the sampling time t_{sp} is treated as reception time. In other words, $t_{sp} = t$. By this change in variables, the sampled source position and the sampled microphone signals are given in terms of reception time as $\bar{x}_s(t)$ and $p(\bar{x}, t)$.

The source strength signal can be obtained from equation (2.20) evaluated at the reception times, $t_j, j = 1, 2, 3, \dots, J$. That is,

$$q(\tau_j) = p(\bar{x}, t_j) 4\pi |\bar{x} - \bar{x}_s(\tau_j)| |1 - M_{so}(\tau_j)|. \quad (2.39)$$

To evaluate this expression, the emission time τ_j corresponding to the reception time t_j is required and it is obtained from equation (2.24) for the case of a source with linear motion (see Figure 2.11a) and by solving the following transcendental equation,

$$c^2(t_j - \tau_j)^2 = |\bar{x}|^2 - 2DR \cos \omega_r \tau_j \quad (2.40)$$

for the case of a source moving along a circular trajectory.

Then, the source position at emission time τ_j is obtained from the sampled source position $\bar{x}_s(t_j)$ by applying a delay $\Delta = t_j - \tau_j$. That is, $\bar{x}_s(\tau_j) = \bar{x}_s(t_j - \Delta)$. However, if the source position at the required emission time do not coincide with a sampled source position data point, then interpolation is used to approximate its value. The estimated source position at emission time is then used to compute the value of the source velocity (in Mach) in the direction source-to-observer using equation (2.18).

Knowing the emission time τ_j^* , the source position at emission time $\bar{x}_s(\tau_j^*)$, and the value of $M_{so}(\tau_j^*)$, the source strength can then be obtained as (see Figure 2.11c)

$$q(\tau_j^*) = p(\bar{x}, t_j) 4\pi |\bar{x} - \bar{x}_s(\tau_j^*)| |1 - M_{so}(\tau_j^*)|. \quad (2.41)$$

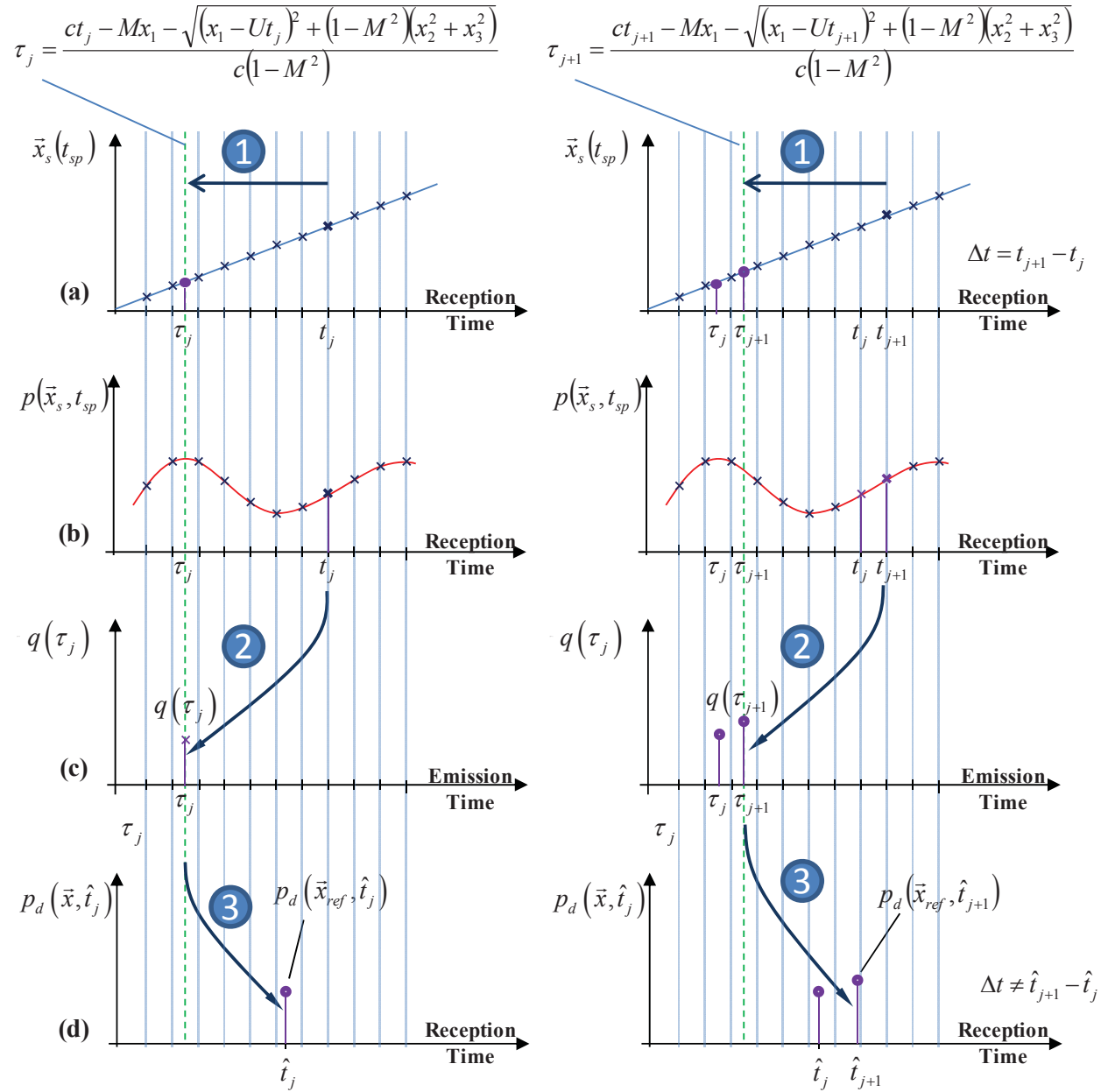


Figure 2.11: Steps involved in the de-Dopplerization of the signal in terms of reception time: (a) original source position signal, and (b) microphone signal measured at equal interval of reception times, (c) estimated source strength signal at emission times, and (d) estimated sound signal at reference observer position.

Using the computed source strength, the pressure at any reference observer position, \bar{x}_{ref} , assuming the source is moving with the source is obtained from

$$p_d(\bar{x}_{ref}, \hat{t}_j) = \frac{p(\bar{x}, t_j) 4\pi |\bar{x} - \bar{x}_s(\tau_j^*)| |1 - M_{so}(\tau_j^*)|}{4\pi |\bar{x}_{ref} - \bar{x}_s|} = p(\bar{x}, t_j) \frac{|\bar{x} - \bar{x}_s(\tau_j^*)| |1 - M_{so}(\tau_j^*)|}{|\bar{x}_{ref} - \bar{x}_s|} \quad (2.42)$$

Note that the new reception times are different than the original reception times, e.g. $\hat{t}_j \neq t_j$.

2.4 Interpolation of the de-Dopplerized Signal

To analyze the frequency content of the de-Dopplerized signal, it must be transformed to the frequency domain. The most common tool to perform this transformation is the Discrete Fourier Transform (DFT) which requires the time signal samples at equally spaced intervals of time. However, as it was shown in Section 2.3.2, the new reception times \hat{t}_j of the de-Dopplerized signal are not equally spaced. Therefore, the de-Dopplerized signal must be interpolated at equally spaced intervals of time.

On the other hand, in section 2.3.1, the original microphone signals need to be interpolated at the corresponding reception times t_j in order to estimate the source strength signal at equally spaced intervals of time. Therefore, independently of the selected de-Dopplerization option, the received (microphone) signals need to be interpolated, also known as re-sampling of the signals.

There are several interpolation methods available. However, from a computational perspective, two of the simpler methods are: 1) Use of the nearest available sample, and 2) linear interpolation using one sample on either side. Howel et al [2], investigated the effect of these two interpolation methods on the signal-to-noise ratio. To this end, they conducted a simulation of a band-limited random noise radiated by an airplane flying at a speed of 0.3 Mach, at an altitude of 300 ft. The microphone signal was sampled at 5 kHz. Upon de-Dopplerization of the microphone signal, the nearest available sample and linear interpolation were used to re-sample the signal at equal intervals of time. When the nearest available sample was used, a modest signal-to-noise ratio of 10 dB was obtained. However, when linear interpolation was used, an 18 dB signal-to-noise ratio was achieved.

Additionally, their study included the effect of increasing the sampling rate to 10 kHz and 50 kHz, i.e. oversampling by a factor of two and ten times the original frequency. When linear interpolation and oversampling by a factor of two was used, a 35 dB signal-to-noise ratio was obtained. Furthermore, linear interpolation and oversampling by a factor of ten yielded a 60 dB signal-to-noise ratio.

It is clear from this section that the interpolation of the de-Dopplerized signals is necessary for the calculation of the DFT and thus this process is computationally intensive. As shown by Howell et al. [2], the method also requires oversampling of the signals to improve the signal-to-noise ratio. These issues are the main drawbacks of the time domain approach.

Chapter 3

Current Beamforming Methods

In general, there are currently two beamforming methods used for noise source identification: The Time Domain (TD) and the Frequency Domain (FD) beamforming methods. The TD beamforming is used exclusively to locate sources of sound in moving objects such as airplanes and wind turbines, whereas FD beamforming is used to locate sound sources in stationary objects. The FD beamforming offers many advantages over TD beamforming. However, the main limitation of this method is its lack of ability to locate sources of sound in moving objects.

This chapter presents the theoretical formulation of both the TD and the FD beamforming methods currently available for noise source identification.

3.1 Time Domain Beamforming for Stationary Sound Sources

This is the most simple and straight forward method to understand the process of beamforming from a physical point of view. Consider the array of N -microphones shown in Figure 3.1. The microphones in this array are located at \vec{x}_n ($n = 1, 2, \dots, N$). For convenience, the origin of the coordinate system is located at the center of the array.

If a monopole source is located at \vec{x}_s as shown in Figure 3.1, then the acoustic pressure recorded by the n^{th} microphone of the array is given by

$$p(\vec{x}_n, t) = \frac{q(\tau)}{4\pi |\vec{x}_n - \vec{x}_s|} = \frac{q(t - |\vec{x}_n - \vec{x}_s|/c)}{4\pi |\vec{x}_n - \vec{x}_s|} \quad (3.1)$$

where $p(\vec{x}_n, t)$ is the acoustic pressure in Pa of the n^{th} microphone at the reception time, $q(\tau)$ is the source strength of the monopole in kg/s^2 , t is the time at which the sound arrives to the observer location, *reception time*, c is the speed of sound in m/s, and \vec{x}_n and \vec{x}_s are the observer and the source position vectors in meters, respectively. The argument of the source strength represents the time at which the sound was emitted and thus it is known as the *emission time* denoted by τ . The time for a sound signal to propagate from the source to the observer location is given by the ratio of the distance between them and the speed of sound, e.g. *propagation time* and given as

$$\Delta t_n = \frac{|\vec{x}_n - \vec{x}_s|}{c} \quad (3.2)$$

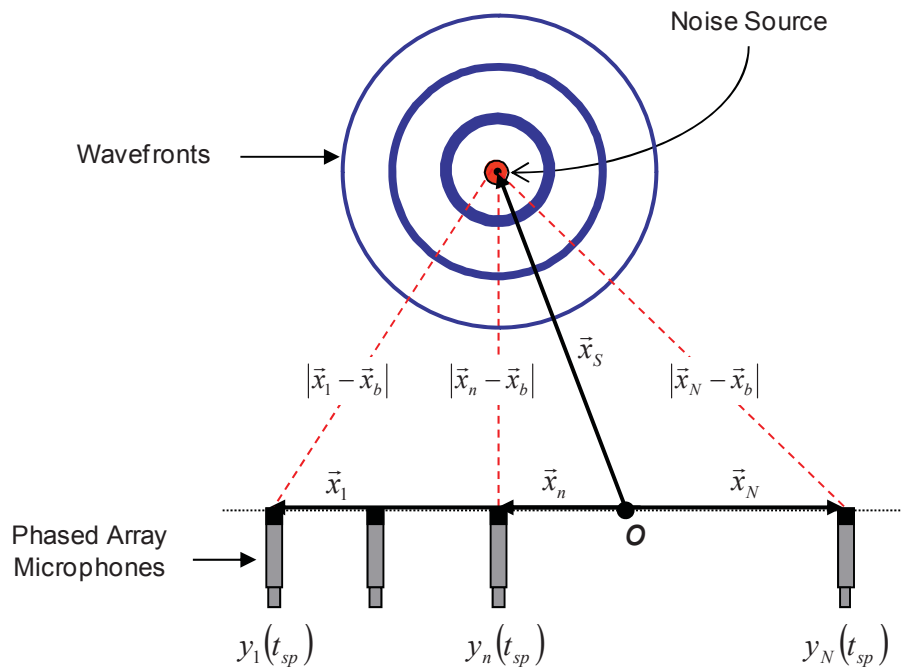


Figure 3.1: Array of microphones sampling the acoustic field of a stationary monopole source.

Let the location of the source be unknown, and let $p_n(t_{sp})$ be the time series of the acoustic pressure recorded by the n^{th} microphones of the array at a sampling frequency f_s .

Then, a beamforming algorithm is used to determine the source location \vec{x}_s . The approach is to assume a source at a potential source location \vec{x}_b as shown in Figure 3.2.

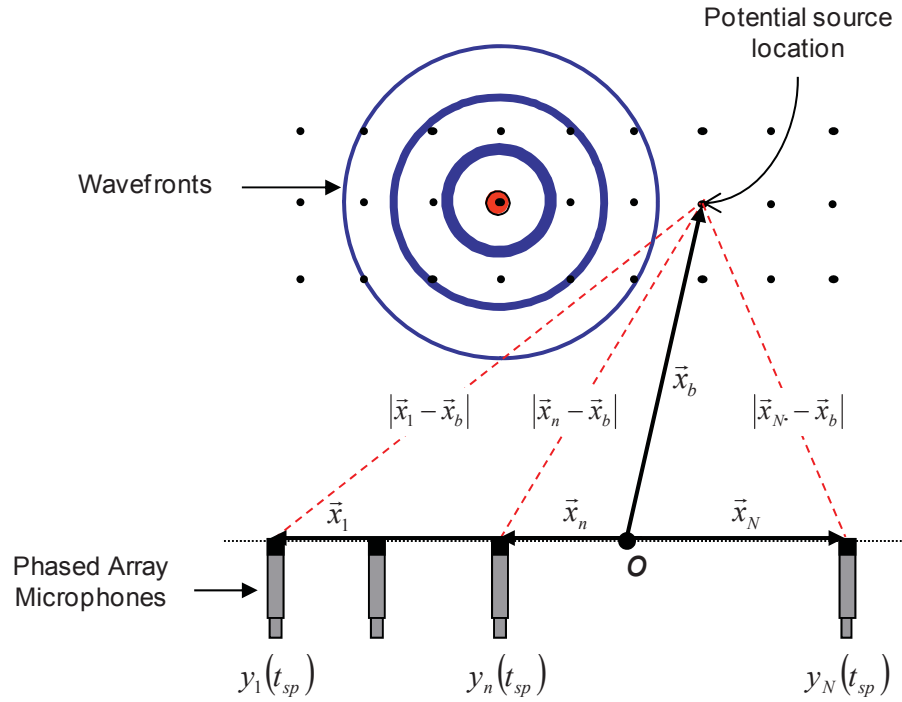


Figure 3.2: Beamforming to a potential source location \vec{x}_b .

Then, the time delay and amplitude of the microphone data are adjusted in such a way as if they originated at \vec{x}_b and received at the array center o , and then added up as follows

$$z(t) = \frac{1}{N} \sum_{n=1}^N w_n p_n(t - \Delta_n) \quad (3.3)$$

where $z(t)$ is termed the beamforming output, and Δ_n is the time delay given by

$$\Delta_n = \frac{|\vec{x}_b| - |\vec{x}_n - \vec{x}_b|}{c} \quad (3.4)$$

The term w_n in equation (3.3) is an amplitude adjustment factor given by

$$w_n = \frac{|\bar{x}_n - \bar{x}_b|}{|\bar{x}_b|} \quad (3.5)$$

The beamforming is then implemented by replacing equations (3.1), (3.4), and (3.5) into equation (3.3) yielding

$$\begin{aligned} z(t_j) &= \frac{1}{N} \sum_{n=1}^N \frac{|\bar{x}_n - \bar{x}_b|}{|\bar{x}_b|} p_n \left(t_j - \frac{|\bar{x}_b| - |\bar{x}_n - \bar{x}_b|}{c} \right) \\ &= \frac{1}{N} \sum_{n=1}^N \frac{|\bar{x}_n - \bar{x}_b|}{|\bar{x}_b|} \frac{q \left(t - \frac{|\bar{x}_n - \bar{x}_s|}{c} - \frac{|\bar{x}_b| - |\bar{x}_n - \bar{x}_b|}{c} \right)}{4\pi |\bar{x}_n - \bar{x}_s|} \end{aligned} \quad (3.6)$$

Note that since the actual source location \bar{x}_s is unknown, and thus, the actual source strength q is also unknown. However, the beamforming output can still be computed from the microphone signals $p_n(t_j - \Delta_n)$ using the top equation in (3.6).

From the bottom equation in (3.6) it can be seen that if the potential source location coincides with the actual source location, i.e., $\bar{x}_b = \bar{x}_s$, then the beamforming output is

$$z(t_j) = p(\bar{x}_s, t_j) = \frac{q \left(t_j - \frac{|\bar{x}_s|}{c} \right)}{4\pi |\bar{x}_s|} \quad (3.7)$$

Equation (3.7) represents the acoustic pressure emitted by the source at \vec{x}_s and perceived at the array center o . On the other hand, if the potential source location does not coincide with the actual source location, i.e., $\vec{x}_b \neq \vec{x}_s$ then the beamforming output is that given by equation (3.6) which will have a value less than that given by equation (3.7).

It should be mentioned that the time domain beamforming presented in this section has a limitation regarding the time delay Δ_n . The method accepts only time delays that are integers of the sampling frequency, e.g. $\Delta_n = K\Delta t$ where K is a positive integer. To relax this limitation, the sampling frequency must be increase. This is not an issue in the frequency domain beamforming as it will be discussed later.

The time domain beamforming approach presented is known as delay-and-sum and estimates the sound produced by the source at the center of the array. Another variation of the approach is to estimate the source strength time history in the emission time scale, $q(\vec{x}_b, \tau)$, of an assumed source positioned at the grid point \vec{x}_b . This is accomplished by using a different set of time delay and amplitude adjustment factors. To this end, the time delay is given by

$$\Delta_n = -\frac{|\vec{x}_n - \vec{x}_b|}{c} \quad (3.8)$$

which represents the time it takes for the sound emitted to arrive to the n^{th} microphone. The amplitude adjustment factor is obtained from the following expression:

$$w_n = 4\pi |\vec{x}_n - \vec{x}_b| \quad (3.9)$$

To evaluate the performance of this second approach, equations (3.1), (3.8), and (3.9) are replaced into equation (3.3). This yields,

$$\begin{aligned}
z(t) &= \frac{1}{N} \sum_{n=1}^N 4\pi |\bar{x}_n - \bar{x}_b| p_n \left(\bar{x}_n, t + \frac{|\bar{x}_n - \bar{x}_b|}{c} \right) \\
&= \frac{1}{N} \sum_{n=1}^N 4\pi |\bar{x}_n - \bar{x}_b| \frac{q \left(t - \frac{|\bar{x}_n - \bar{x}_s|}{c} + \frac{|\bar{x}_n - \bar{x}_b|}{c} \right)}{4\pi |\bar{x}_n - \bar{x}_s|}
\end{aligned} \tag{3.10}$$

Equation (3.10) shows that when the potential source location coincides with the actual source location, i.e., $\bar{x}_b = \bar{x}_s$ the beamforming output equals the strength of the actual source, i.e. $z(t) = q(t)$. However, when the potential source location does not coincide with the actual source location, i.e., $\bar{x}_b \neq \bar{x}_s$ the beamforming output will have a value less than the actual source strength.

For this particular case when the source is stationary, the sampling period in all the signals is the same, e.g. microphones and source. In other words, if the source emits pulses of sound at equally spaced intervals of time, these pulses will arrive to the observer, i.e. microphone, with the same equally spaced intervals of time.

To analyze the frequency content of the sound emitted by the source, the general approach is to take the beamforming output time signal and convert it to the frequency domain using the DFT as

$$Z(\bar{x}_b, f_k) = DFT \{z(\bar{x}_b, t)\} \tag{3.11}$$

Then, the mean square value (msv) of this transformed signal is estimated using the following expression:

$$z_{rms}^2(\bar{x}_b, f_k) = \frac{1}{2} \frac{1}{N_b} \sum_{N_b} |Z(\bar{x}_b, f_k)|^2 = \frac{1}{2} \left\langle |Z(\bar{x}_b, f_k)|^2 \right\rangle \tag{3.12}$$

where $\langle \rangle$ denotes average, and N_b is the number of data blocks used in the estimation of the average msv. Finally, the decibel values of the average msv beamforming output are computed and plotted as acoustic maps.

Figure 3.3 is an example of acoustic maps showing noise radiated from the Virginia Tech Stability Wind Tunnel fan. In these maps, the scanning plane was located parallel to the rotor plane at the trailing edge of the stator vanes. A grid resolution of 0.0127-m was used in both the x and y directions. The results of this test clearly identified a dominate noise source at the blade tip.

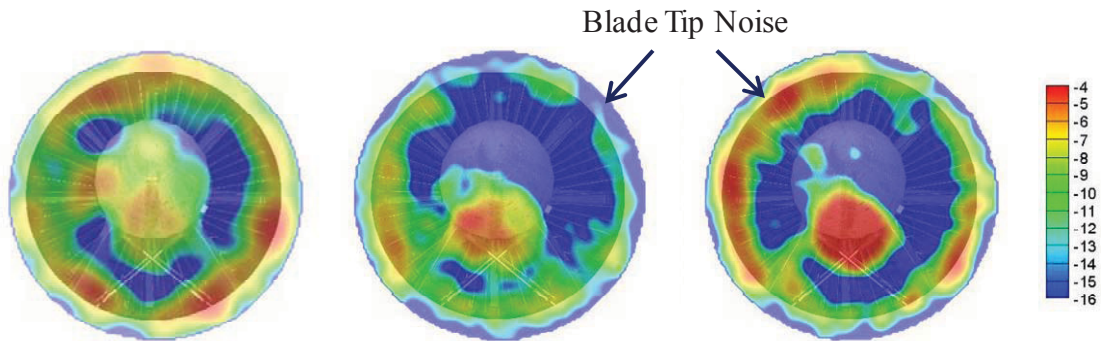


Figure 3.3: Example of acoustic maps obtained using a frequency domain beamforming algorithm.

3.2 Time Domain Beamforming for Moving Sound Sources

The Time Domain beamforming method for moving sources of sound combines the delay-and-sum algorithm for stationary sound sources with the de-Dopplerization technique described in Chapter 2. This is the only currently available method to locate moving sources of sound. In this section, the Time Domain beamforming method is explained for the case of a source with linear motion first and then extended for the case of a source with circular motion.

The sound emitted by this monopole source is sampled simultaneously by an array of N -microphones located at $\vec{x}_n, n=1,2,\dots,N$. The data acquisition system records the microphone time signals at a sampling frequency f_s . The position of the source is also recorded at the same sampling times as the microphone signals by a sensor such as GPS, optical, etc. As illustrated in Figure 3.4, data acquisition starts at time $t_{sp} = 0$, when the source is located at $\vec{x}_s(0)$, and it ends at time $t_{sp} = t_f$, when the source is located at $\vec{x}_s(t_f)$. The total number of samples is $N_s = t_f f_s$. Figure 3.5a,b illustrate the source position and microphone signals sampled at equal intervals of time. In this figure, the j^{th} sample for the n^{th} microphone is $y_n(t_{sp-j})$ while for the source position it is $\vec{x}_s(t_{sp-j})$. As explained in Section 2.3, the sampling time for the microphone and source position signals can be treated as emission time (e.g. if considered in the source reference frame) or as reception time (e.g. if considered in the observer reference frame). Generally, in time domain beamforming, the sampling time for the microphone signals and source position signal are treated as emission time.

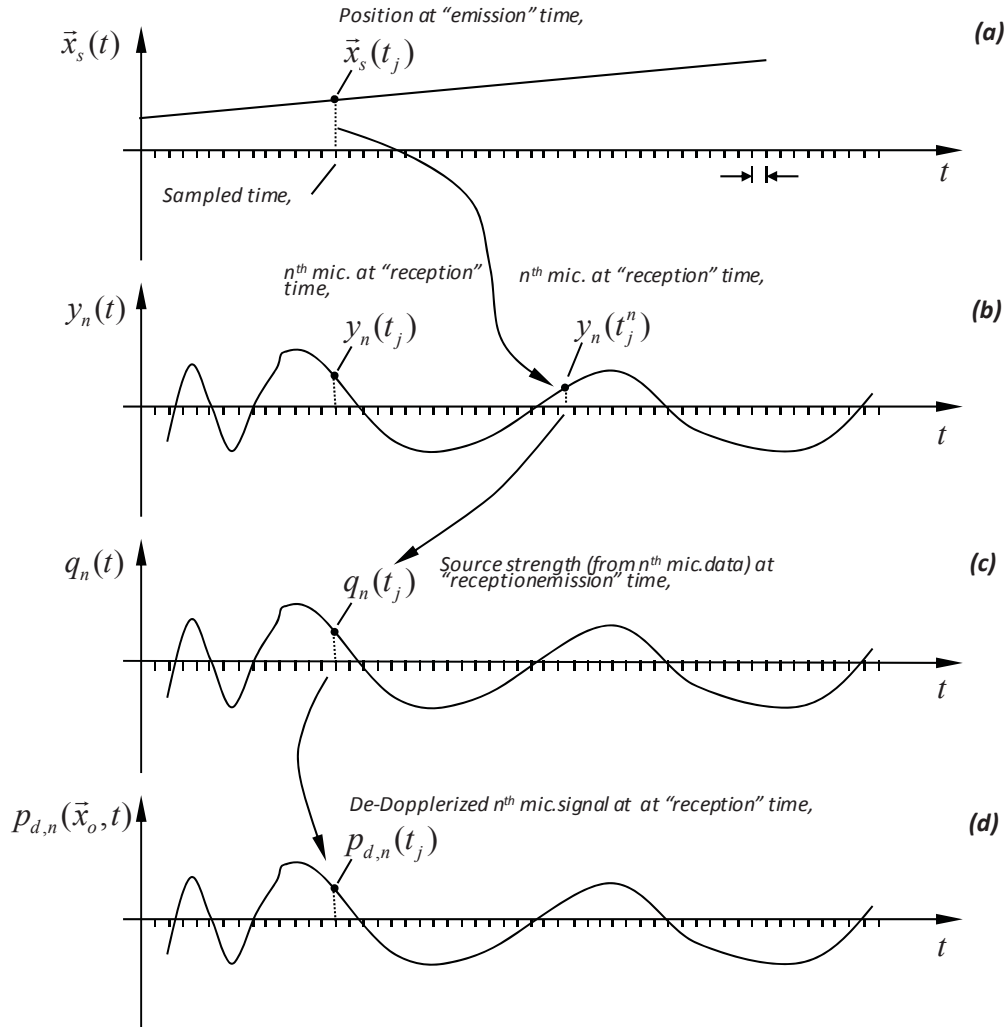


Figure 3.5: Illustration of (a) source position signal, (b) n^{th} microphone signals, (c) estimated source strength, and (d) n^{th} de-DeplORIZATION microphone signal for reference location of source.

Time Domain beamforming can be performed either at the source, i.e. to estimate the source strength, or at a reference observer, i.e. to estimate the pressure at an observer moving with the source. These approaches are explained in the next two sections.

3.2.1.1 Time Domain Beamforming for Source Strength Estimation

In this approach, the first step consists of computing the source strength $q(\tau_j)$ at the emission times $\tau_j, j = 0, \dots, N_s$ corresponding to the equally spaced samples of source position $\bar{x}_s(t_{sp-j})$ from the microphone signals. In other words, for each sampled source position, the corresponding source strength is computed from the microphone signals. The calculations

involved in this step are the same calculations described in Section 2.3.1 to de-Dopplerize the microphone signal based on emission time. That is, the reception time for each microphone of the array t_j^n at the moment the source is at $\bar{x}_s(t_{sp-j})$ is computed using equation (2.21). That is

$$t_j^n = t_{sp-j} + \frac{|\bar{x}_n - \bar{x}_s(t_{sp-j})|}{c} \quad (3.13)$$

Then the source strength at the emission time is computed for every point in the scanning grid using equation (2.20) as

$$q_n(t_{sp-j}) = y_n(t_j^n) 4\pi |\bar{x}_n - \bar{x}_s(t_{sp-j})| |1 - M_{so}(t_{sp-j})| \quad (3.14)$$

However, due to the discrete number of samples, it will usually be the case that a sample of the acoustic pressure at the required observer time, $y_n(t_j^n)$, will not be available. Or in other words, the reception time t_j^n doesn't coincide with a data point in the microphone record. In this case, the required amplitude of the acoustic pressure is obtained by linear interpolation using the two closest available samples. This first step, i.e. the estimation of the source strength signal at emission time, involves a change of reference frame from the observer reference frame to the source reference frame. This change of reference frame, i.e. temporal coordinates, eliminates the Doppler effects caused by the source motion. Once the de-Dopplerized source strength has been estimated from the microphone signals, the next step is to compute the average source strength over the array microphones as

$$z(t_{sp-j}) = \frac{1}{N} \sum_{n=1}^N q_n(t_{sp-j}). \quad (3.15)$$

which is the time-domain beamforming output.

3.2.1.2 Time-Domain Beamforming for Acoustic Pressure Estimation

The first step in this approach is identical to the first step in time-domain beamforming for source strength estimation presented in the previous section. That is, the de-Dopplerized source strength $q_n(t_{sp_j})$ is estimated from the microphone signals using equation (3.14). Then, the second step consists of computing the acoustic pressure at the array center O as if the array would be moving with the same velocity and in the same direction as the monopole source. This is accomplished using equation (2.10) that yields the acoustic pressure at the microphone location of a monopole source at rest (relative to the array) from the source strength recovered from each array microphone, $q_n(t_{sp_j})$. To this end, the source must be located at a reference location $\bar{x}_s(t_{ref})$ or the source position at a reference time t_{ref} . That is

$$p_{d,n}(\bar{x}_o, t_j) = \frac{q_n\left(t_j - \frac{|\bar{x}_o - \bar{x}_s(t_{ref})|}{c}\right)}{4\pi|\bar{x}_o - \bar{x}_s(t_{ref})|} \quad (3.16)$$

where $p_{d,n}(t_j)$ is the pressure at the center of the array from the n^{th} source strength at the sampled time t_j .

Finally, the de-Dopplerized acoustic pressure obtained from the N microphone signals are summed to yield the Time-Domain beamforming output as

$$z(t_j) = \frac{1}{N} \sum_{n=1}^N p_{d,n}(\bar{x}_o, t_j) \quad (3.17)$$

From this process, it is clear that the actual “delay-and-sum beamforming process” takes place in equations (3.14) and (3.15) for source strength estimation, and in equations (3.14) and (3.17) for acoustic pressure estimation for the delay and sum, respectively. Furthermore, this process is repeated for every point of the scanning grid. Each grid point is treated as a potential

source where the location is slightly different, i.e. $\vec{x}_s(t_j)$ is different for each grid point. To this end, every data point of the time series of every microphone of the array needs to be interpolated to estimate the de-Dopplerized source strength for every grid point. Interpolation requirement makes the time domain beamforming method extremely computationally intensive.

3.2.2 Rotational Motion

Consider now the case of a monopole source moving along a circular trajectory as shown in Figure 3.6. An array of N -microphones samples the acoustic field of this source as it undergoes several revolutions. As before, the microphone positions are defined by $\vec{x}_n, n=1,2,\dots,N$.

To determine the spatial location of the source as a function of time, a rotation sensor is used to sample the angular position of the source at each sampled time, t_{sp_j} . Obviously the angular velocity, ω_r , can also be easily determined. Once again both microphone and detection sensor data are sampled simultaneously. Without loss of generality, the additional assumption here is that there are an integer number of samples with a revolution of the source. Therefore, the sampling frequency, number of samples in a revolution, and angular velocity are related as $f_s = N_s \omega_r / 2\pi$. Time domain beamforming involves several steps requiring careful tracking of the source signal at emission times, microphone signals at the receiving times, and position of the source in its circular pattern.

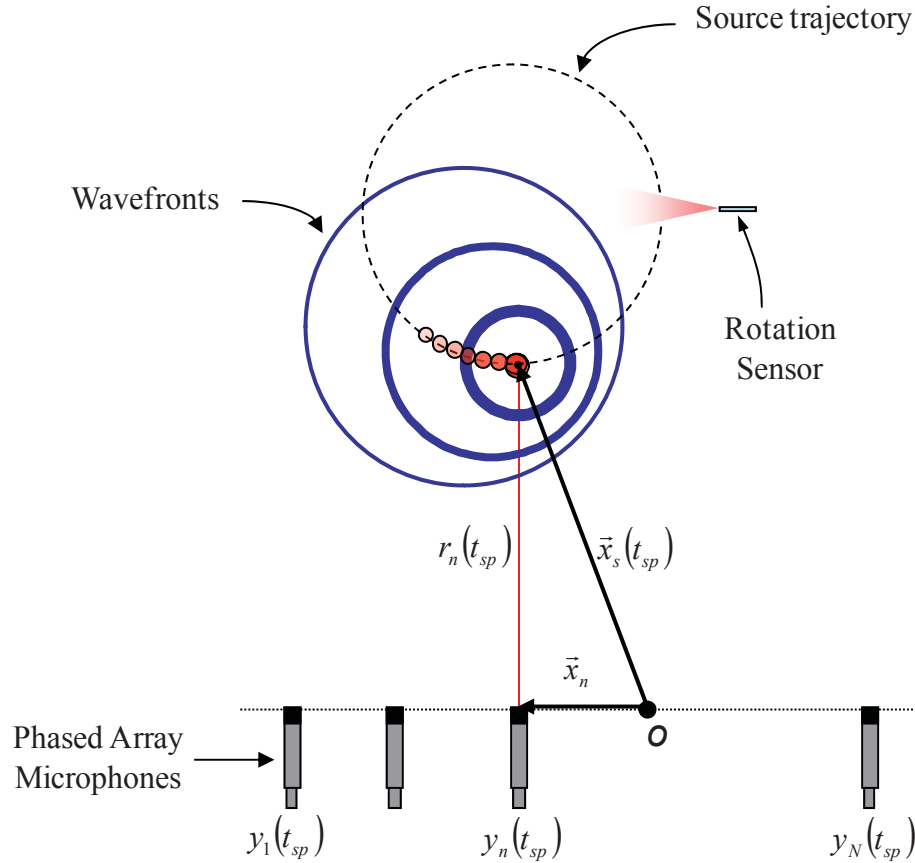


Figure 3.6: Sound field of a rotating source recorded by an array of microphones.

As in the case of the source with linear motion, time domain beamforming for rotating sources can also be performed at the source, i.e. to estimate the source strength, or at a reference observer, i.e. to estimate the pressure at an observer rotating with the source. Each of these two approaches are explained in the next sections.

3.2.2.1 Time Domain Beamforming for Source Strength Estimation

The first step of this approach consists of identifying the period of source revolution. This is accomplished using the rotation sensor signal, i.e. the number of pulses per revolution multiplied by the time elapsed between two consecutive pulses. Then, the time period corresponding to each source revolution is divided into an equally spaced number of points t_{sp-j} , $j = 1, 2, 3, \dots, N$, representing emission times. a shows the rotation sensor signal as one per revolution pulse.

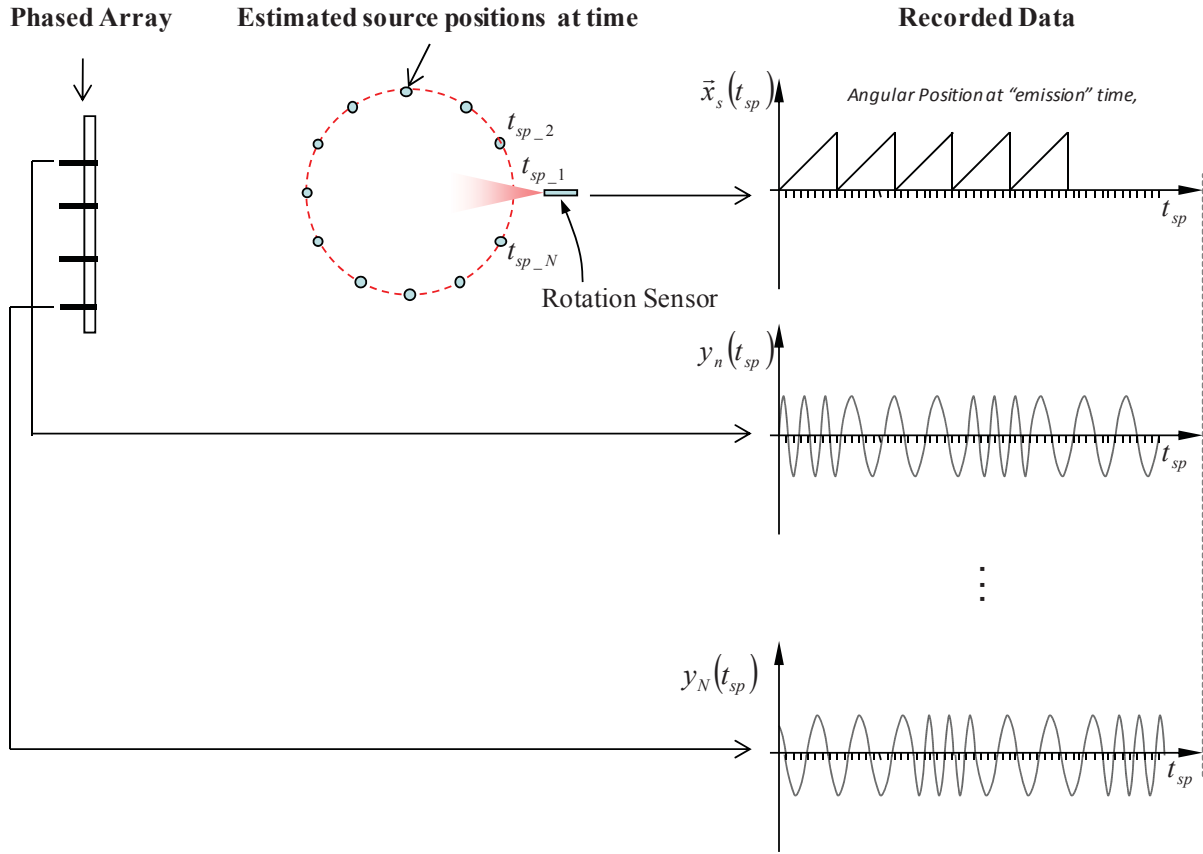


Figure 3.7: First step in the TD beamforming algorithm: A period of revolution is identified and divided into a set of J equally spaced emission times.

For each emission time t_{sp-j} , the corresponding propagation time from the source to the n^{th} microphone in the array is computed as

$$t_j^n = t_{sp-j} + \frac{|\bar{x}_n - \bar{x}_s(t_{sp-j})|}{c} \quad (3.18)$$

The second step of the algorithm consists of computing an estimate of the de-Dopplerized strength of an assumed source at the emission time t_{sp-j} from the acoustic pressure data recorded by each microphone y_n . This is accomplished as follows,

$$q_n(t_{sp-j}) = y_n(t_j^n) 4\pi |\bar{x}_n - \bar{x}_s(t_{sp-j})| |1 - M_{so}(t_{sp-j})| \quad (3.19)$$

where $M_{so}(t_{sp_j})$ is the source velocity component in the direction source-to-receiver.

The fact that N source strength functions, q_n , are obtained could be misleading since only a single source was assumed at \vec{x}_b . However, each of these source strength functions are an estimate of the assumed source strength at \vec{x}_b obtained from the data sampled by the n -th microphone. Figure 3.8 shows this calculation process for the emission times t_{sp_j} . From this figure it can be seen that, as pointed before, a sampled data point may not necessarily be available at the desired observer time t_n . In this case, there are several options, two of which were discussed in Chapter 2. One option involves the use of the closest sampled data value, whereas another option consists of performing a linear interpolation using the two closest sampled data values.

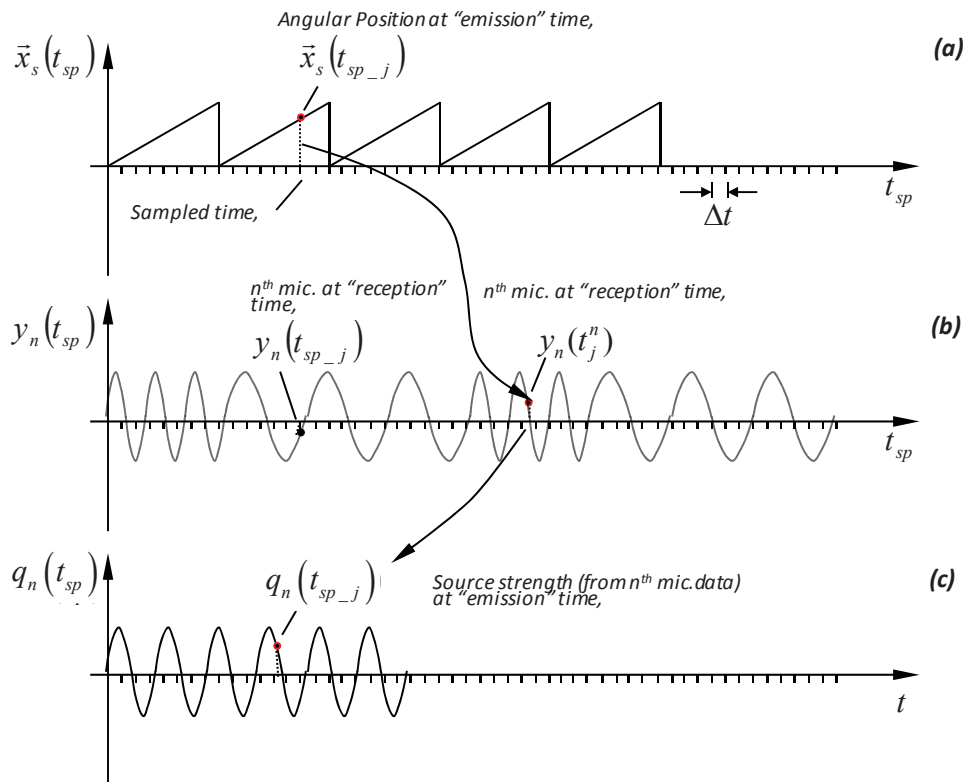


Figure 3.8: Illustration of (a) angular source position signal, (b) n th microphone signals, and (c) estimated de-Dopplerized source strength.

Once the de-Dopplerized source strength has been computed from every microphone, the next step involves the computation of the average source strength over the microphones of the array as

$$z(\vec{x}_b, t) = \frac{1}{N} \sum_{n=1}^N q_n(t_{sp}) \quad (3.20)$$

which is the time domain beamforming output in terms of source strength for rotating sources of sound.

3.2.2.2 Time Domain Beamforming for Acoustic Pressure Estimation

The first two steps for this approach are identical to the first two steps for time domain beamforming for source strength estimation presented in the previous section. That is, the de-Dopplerized source strength $q_n(t_{sp_j})$ is computed using equation (3.19). The next step consists of computing the acoustic pressure at the array center induced by the assumed source at \vec{x}_b from the estimated source strength functions $q_n(t_{sp})$, $n=1, \dots, N$, according to:

$$z(\vec{x}_b, t) = \frac{1}{4\pi \|\vec{x}_b(\tau_1)\| N} \sum_{n=1}^N q_n(t_{sp}) \quad (3.21)$$

which is the beamforming output in terms of the de-Dopplerized acoustic pressure at the array center.

Independently of the time domain beamforming approach selected, i.e. for source strength or acoustic pressure estimation, in practical situations the frequency content of the source under consideration is desired. To this end, the beamforming output is transformed to the frequency domain using the DFT and the mean square value (msv) of this transformed beamforming output is estimated using the following expression:

$$z_{rms}^2(\bar{x}_b, f_k) = \frac{1}{2} \frac{1}{N_b} \sum_{N_b} |Z(\bar{x}_b, f_k)|^2 = \frac{1}{2} \langle |Z(\bar{x}_b, f_k)|^2 \rangle \quad (3.22)$$

where N_b is the number of blocks used in the averaging process. For the particular case where the source is moving along a circular trajectory, each block contains data for one source revolution.

To understand the output of the algorithm, substitute the unknown pressure field expression given by equation (3.1) into equation (3.19) as,

$$\bar{q}_n(\tau_j) = 4\pi \|\bar{x}_n - \bar{x}_b(\tau_j)\| \cdot \|1 - Mr_{n,j}\| \frac{q \left(t - \frac{\|\bar{x}_n - \bar{x}_s(\tau_j)\|}{c} + \frac{\|\bar{x}_n - \bar{x}_b(\tau_j)\|}{c} \right)}{4\pi \|\bar{x}_n - \bar{x}_b(\tau_j)\| \cdot \|1 - Mr_{n,j}\|} \quad (3.23)$$

From equation (3.23) it can be seen that when $\bar{x}_b(\tau_j) = \bar{x}_s(\tau_j)$ then the estimated source strength approximates the actual source strength $q(\tau) \cong \bar{q}(\tau)$. However, if $\bar{x}_b(\tau_j) \neq \bar{x}_s(\tau_j)$ then $q(\tau)$ and $\bar{q}(\tau)$ are out of phase by a delay F given by:

$$F = \frac{1}{c} \left(\|\bar{x}_n - \bar{x}_s(\tau_j)\| + \|\bar{x}_n - \bar{x}_b(\tau_j)\| \right) \quad (3.24)$$

In terms of the beamforming output, if the assumed source location coincides with the actual source location then the signals are in phase and the beamforming output approximates the acoustic pressure at the array center induced by the actual source. On the other hand, if the assumed source location does not coincide with the actual source location, then the signals are out of phase and the beamforming output is distorted and diminished.

3.3 Frequency Domain Beamforming for Stationary Sound Sources

In this section, the concept of delay-and-sum beamforming is extended to the frequency domain for only the case of source strength estimation. However, before proceeding with the explanation of the frequency domain method, the Fourier Transform which is used to transform the microphone signals from the time domain to the frequency domain is first presented.

3.3.1 Transformation of Time Domain Data into the Frequency Domain

The equations that allow to transform microphone time data into the frequency domain and vice versa are the so-called Discrete Fourier Transform pair given as

$$y(n) = \frac{1}{N} \sum_{k=1}^{N-1} Y(k) e^{i\omega k \Delta t} \quad (3.25)$$

where,

$$Y(\omega) = \sum_{n=0}^{N-1} y(n) e^{-i\omega k \Delta t} \quad (3.26)$$

Equations (3.25) and (3.26) are known as the Inverse Discrete Fourier Transform (IDFT) and the Discrete Fourier transform (DFT) equations, respectively. See Appendix A.1.4 for a detailed derivation of equations (3.25) and (3.26).

Equation (3.26) is the starting point of any frequency domain analysis as it allows representing any non-periodic time domain discrete signal of finite duration as a combination of sinusoidal basis functions. The property that makes possible this transformation is the orthogonality of the basis functions which can be expressed as:

$$\sum_{n=0}^{N-1} \left(e^{i\omega k \Delta t} \right) \cdot \left(e^{-i\omega k' \Delta t} \right) = N \delta_{kk'} \quad (3.27)$$

where $\delta_{kk'}$ is the Dirac function.

3.3.2 Conventional Frequency Domain Beamforming

To proceed with the explanation of the mathematical formulation of the frequency domain beamforming method, assume the source of interest is a monopole located at \vec{x}_s . Taking the Fourier Transform of the sound field of a monopole source in equation (3.1) yields the acoustic field in the frequency domain as

$$P(\vec{x}, f) = \frac{Q(f)}{4\pi |\vec{x} - \vec{x}_s|} \cdot e^{-i2\pi f \Delta t} \quad (3.28)$$

where $Q(f)$ is the Fourier Transform of the monopole source strength $q(t)$, and the exponential term $e^{-i2\pi f \Delta t}$ accounts for the phase difference between the source and the microphone signal which is related to the propagation time

$$\Delta t = \frac{|\vec{x} - \vec{x}_s|}{c}$$

Therefore, equation (3.28) is the frequency domain version of equation (3.1). For simplicity, equation (3.28) can be re-written as

$$P(\vec{x}|\vec{x}_s, f) = Q(f) \cdot G(\vec{x}|\vec{x}_s, f) \quad (3.29)$$

where P , Q , and G are complex, and G is given as

$$G(\vec{x}|\vec{x}_s, f) = \frac{e^{-i2\pi f|\vec{x}-\vec{x}_s|/c}}{4\pi|\vec{x}-\vec{x}_s|} \quad (3.30)$$

Equation (3.30) is the free-field Green's function of a monopole source.

As shown in section 3.1, time domain beamforming is achieved by delaying the microphone signals, adjusting their amplitude and summing the signals over the array microphones to steer the array to a particular location \vec{x}_b , where a potential source might be present. The equivalent of a time delay in the time domain is a phase shift in the frequency domain. Therefore, beamforming in the frequency domain is achieved by applying phase shifts and amplitude adjustments to the microphone signals to steer the array to a particular location \vec{x}_b .

The source strength estimated from the signal of the n -th microphone can be obtained from equation (3.29) as

$$Q_n(f) = \frac{G(\vec{x}|\vec{x}_s, f)^* P(\vec{x}|\vec{x}_s, f)}{|G(\vec{x}|\vec{x}_s, f)|^2} \quad (3.31)$$

where the “*” denotes complex conjugate. Therefore, the beamforming output from the N microphones of the array can be obtained from the following expression,

$$Z(\vec{x}_b, f) = \frac{1}{N} \sum_{n=1}^N Q_n(f) \quad (3.32)$$

Equation (3.32) is then used to compute the mean square value as,

$$Z_{rms}^2(\vec{x}_b, f) = \frac{1}{2} \langle |Z(\vec{x}_b, f)| \rangle = \frac{1}{2N^2} \left\langle \sum_{m=1}^N \sum_{n=1}^N Q_m(f) Q_n(f)^* \right\rangle \quad (3.33)$$

Substituting equation (3.31) into equation (3.33) yields,

$$Z_{rms}^2(\bar{x}_b, f) = \frac{1}{2N^2} \left\langle \sum_{m=1}^N \sum_{n=1}^N \frac{G_m(\bar{x}|\bar{x}_s, f)^*}{|G_m(\bar{x}|\bar{x}_s, f)|^2} P_m(\bar{x}|\bar{x}_s, f) P_m(\bar{x}|\bar{x}_s, f)^* \frac{G_m(\bar{x}|\bar{x}_s, f)}{|G_m(\bar{x}|\bar{x}_s, f)|^2} \right\rangle \quad (3.34)$$

which is the expression for the beamforming output for conventional frequency domain beamforming.

Chapter 4

A New Frequency Domain Beamforming Method

Frequency-domain beamforming is a very powerful method for noise source identification due to its robustness and its computational efficiency. As it is explained in Chapter 3, this method exploits mainly the phase difference between the various microphones of the array to identify the spatial location of the sound source. Unfortunately this method does not work for moving sources of sound.

There are two reasons why frequency-domain beamforming does not work to locate moving sources of sound. First, as a sound source moves in space, the relative phase between the various microphones of the array changes as a function of source location. Secondly, as explained in Chapter 2, the sound field of a moving sound source is distorted by the Doppler effect. As a result, the signals received by the array microphones are non-stationary signals.

In conventional frequency domain beamforming of static sound sources, the first step involves the transformation of the time domain microphone data into the frequency domain by means of the Discrete Fourier Transform (DFT) equation. However, when the sources of sound are not static, the use of the DFT equation to transform the time series of a moving sound source yields a distorted frequency spectrum. This spectrum does not resemble that of the sound source and in many cases the original source frequency can be completely missed as it will be shown later in this chapter.

If the time series of the acoustic pressure recorded by the microphones of an array from a moving sound source could be transformed into the frequency domain and the Doppler effect be removed yielding the correct frequency and phase spectra, then the frequency domain beamforming method could be used to locate moving sources of sound.

This is precisely the approach presented in this chapter to develop a frequency domain beamforming method for moving sound sources. First a de-Dopplerization technique capable of recovering the correct frequency and phase spectra of a moving sound source is presented. Then, this technique is implemented into a frequency domain beamforming algorithm.

4.1 Introduction to the New Method

The new method is performed completely in the frequency domain. In general terms, the approach proposed here consists in breaking down the motion of the source in short time periods. For each time period, the corresponding time window at each microphone in the array is isolated from the knowledge of the source position at the emission times. The Doppler effect from the isolated microphone signal is removed using the translation and rescaling properties of the Fourier Transform. The amplitude decay of the signal due to the spherical spreading is also compensated for using the linear property of the Fourier Transform. These transform properties allow to estimate the source spectrum. Thus, the de-Dopplerization and amplitude compensation of the microphone signal is carried out in the frequency domain. The source spectrum due to each microphone in the array is now used to find the source location as if it is stationary. In other words, a conventional frequency domain beamformer at the source is implemented using this approach. This approach will be developed for both linear and rotational motion of the source.

4.2 Linear, Translation, and Scaling Properties of the Fourier Transform

The linear, translation, and scaling properties of the Fourier Transform for a continuous stationary signal are described in the Appendix. Since the linear, translation, and scaling properties of the Fourier Transform are used here to perform the de-Dopplerization of the microphone signals, these properties are presented in detail for the finite duration signals.

Figure 4.1 shows a signal, $p(t)$, with a finite duration time, T . This signal is then multiplied by a constant κ , translated by α seconds, and time scaled at a linear rate of β to result in a distorted signal, $p_d(t) = \kappa p(\alpha + \beta t)$. The time window where the distorted signal doesn't vanish is thus βT . For reasons that will become clear later, the center point of the time window is used here as the reference to identify the translation, e.g. the center of the window is at $t=0$.

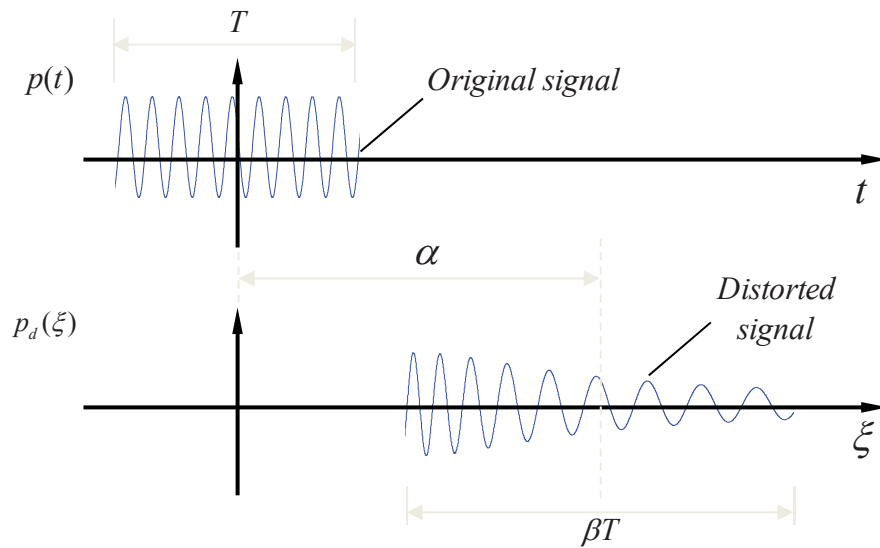


Figure 4.1: (a) Original and (b) translated and scaled signals.

The Fourier Transform of the distorted signal is

$$P_d(f) = \int_{-\infty}^{\infty} p_d(\xi) e^{-j2\pi f\xi} d\xi = \int_{-\infty}^{\infty} p(\alpha + \beta t) e^{-j2\pi ft} dt \quad (4.1)$$

Following the same derivations as in Appendix A.1.5, the following change of variables is used

$$\xi = \alpha + \beta t \quad (4.2)$$

to express the FT of the distorted signal in terms of the original one.

Replacing equation (4.2) into equation (4.1) leads to

$$P_d(f) = \kappa \int_{-\infty}^{\infty} p(\xi) e^{-j2\pi f \left(\frac{\alpha - \xi}{\beta} \right)} \frac{d\xi}{\beta} \quad (4.3)$$

or

$$\begin{aligned} P_d(f) &= \kappa \int_{-\infty}^{\infty} p(\xi) e^{-j2\pi f \left(\frac{\alpha - \xi}{\beta} \right)} \frac{d\xi}{\beta} \\ P_d(f) &= \kappa \frac{e^{-j2\pi f \left(\frac{\alpha}{\beta} \right)}}{\beta} \int_{-\infty}^{\infty} p(\xi) e^{j2\pi \frac{f}{\beta} \xi} d\xi = \kappa \frac{e^{-j2\pi \hat{f} \alpha}}{\beta} P(\hat{f}) \end{aligned} \quad (4.4)$$

where $\hat{f} = f/\beta$.

This implies that the spectrum of the original signal can be obtained from the FT of the amplified, translated, and scaled signal. The spectrum needs to be corrected by adjusting the frequency, phase, and amplitude using the factors $\hat{f} = f/\beta$, $e^{j2\pi \hat{f} \alpha}$, and both κ and β , respectively. That is,

$$P(\hat{f}) = \frac{\beta}{\kappa} e^{j2\pi \hat{f} \alpha} P_d(f) \quad (4.5)$$

Note that in the computation of the FT in equation (4.3), the integral limits must be sufficiently long to encompass both the original and distorted signals. The lower and upper limits can be easily computed as $t_{lower} = -T/2$ and $t_{upper} = \alpha + \beta T/2$, respectively.

In the proposed de-Dopplerization method here, the FT of the distorted signal will be computed and used to estimate the original signal. For convenience, the FT will be carried out only over the window the signal doesn't vanish. That is,

$$P_d(f) = \int_{\alpha - \beta T/2}^{\alpha + \beta T/2} p_d(\xi) e^{-j2\pi f \xi} d\xi \quad (4.6)$$

In this case, the phase correction term induced by the translation must not be included in the computation of the FT of the original signal. Therefore, the FT becomes simply

$$P(\hat{f}) = \frac{\beta}{\kappa} P_d(f) \quad (4.7)$$

under the condition that $P_d(f)$ is computed using equation (4.6).

4.3 Frequency Domain de-Dopplerization

The linear, translation, and rescaling properties of the FT constitute the main approach to perform the frequency domain de-Dopplerization and compensation of the microphone signals. Thus, this section presents how they are used in the problem at hand. As shown in Figure 4.2, consider a source moving along the 1-direction whose position is defined by the vector $\vec{x}_s(\tau)$. The source emits sound with source strength, $q(\vec{x}_s(\tau), \tau)$, at emission time τ . The sound is sensed with a fixed microphone placed at \vec{x}_n . The signal observed by the microphone is $p_n(t)$ at the reception time t . The source position and microphone signals are recorded simultaneously at the same sampling frequency.

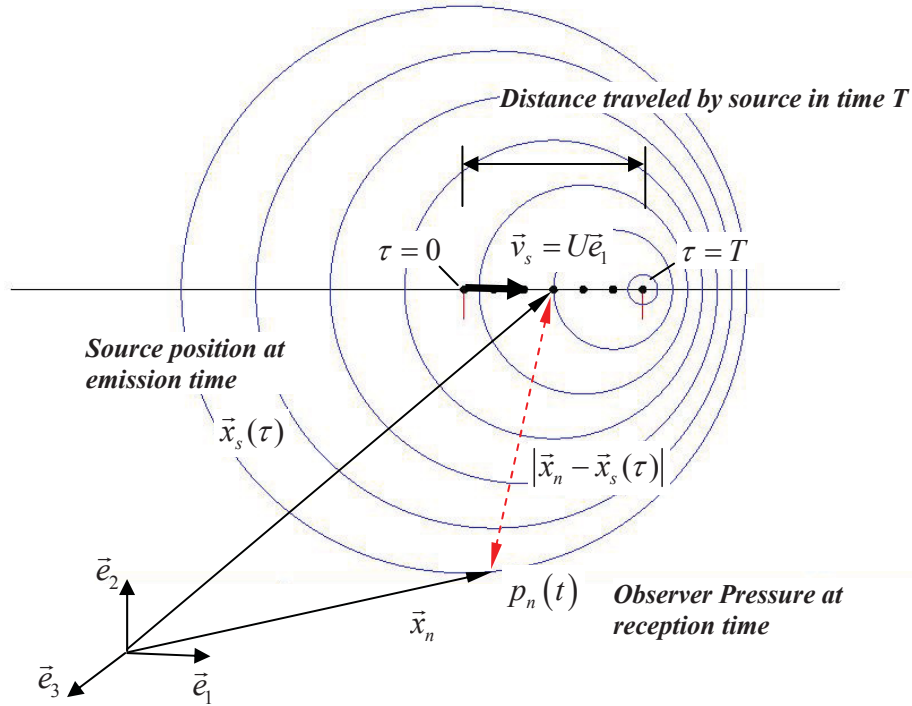


Figure 4.2: Source of sound moving along the 1-direction, sensed by a fixed microphone located at \vec{x}_n .

Note that the source position is known at the emission times while the microphone signal is recorded at the reception times. Since the signal recorded by the microphone is non-stationary, we consider the motion of the source over a short duration of time T . For convenience, this time window is selected such that $-T/2 \leq \tau \leq T/2$, e.g. at $\tau = 0$ the source is at the center of the window. For a given sampling frequency f_s , the number of sampled points in the window is $N_s = f_s T$. Thus, the sampled emission times are $\tau_k = k\Delta t$ for $k = 0, 1, \dots, N_s - 1$.

The microphone time history is given as

$$p_n(t) = \frac{q(\tau)}{4\pi |\vec{x}_n - \vec{x}_s(\tau)| |1 - M_{so}(\tau)|} \quad (4.8)$$

where the emission and reception times are related as

$$t = h_n(\tau) = \tau + \frac{|\vec{x}_n - \vec{x}_s(\tau)|}{c} \quad (4.9)$$

To implement the Fourier Transform properties here, the microphone signal plays the roll of the distorted signal while the source strength of the original signal in section 4.2, i.e. $p_n(t) \leftrightarrow p_d(\xi)$ and $q(\tau) \leftrightarrow p(t)$.

This implies that the sound emitted by the source over time T can be related to the time window that the sound is observed by the microphone, $T_{reception}$, as shown in Figure 4.3. The reception times at the beginning and end of the time window are simply $t_{start} = h_n(-T/2)$ and $t_{end} = h_n(T/2)$. Also note that the time window at reception times, is different than the time window at the emission times, e.g. $T_{reception} = t_{end} - t_{start} \neq T$. In other words, the number of samples within this reception time window is $N_{s-reception} = T_{reception} / \Delta t$ that is different than the number of samples over time T .

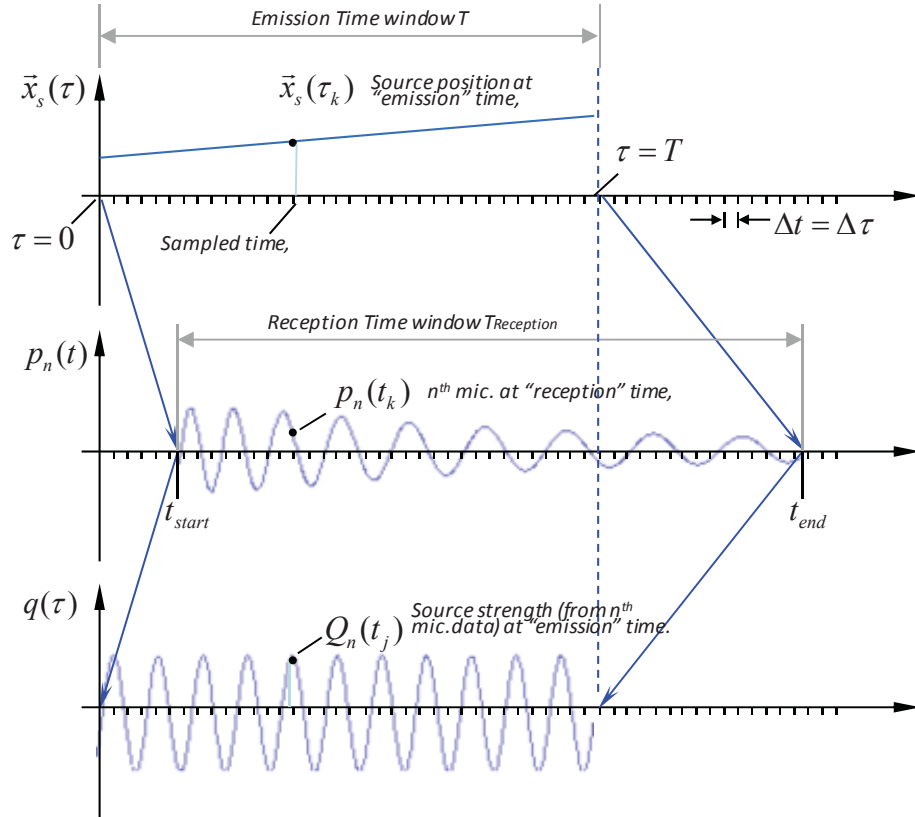


Figure 4.3: Emission time window and its correspondent reception time window over a short time period.

For the linear motion assumed here and assuming the coordinate system to be located at the source at time $\tau = 0$, $h_n(\tau)$ has a closed form expression given by

$$t = h_n(\tau) = \tau + \frac{\sqrt{(x_{1n} - U\tau)^2 + x_{2n}^2 + x_{3n}^2}}{c} \tag{4.10}$$

where $\vec{x}_n = x_{1n}\vec{e}_1 + x_{2n}\vec{e}_2 + x_{3n}\vec{e}_3$.

The translation and rescaling properties of the FT can be used if the reception/emission time relationship $t = h_n(\tau)$ is linear. Thus, using Taylor' series expansion around τ_o , this relationship can be written as a linear function as (See Appendix A.1.6)

$$t = h_n(\tau) \approx h_{no} + \frac{dh_n}{d\tau} \tau = h_{no} + h_{nr} \tau \quad (4.11)$$

For $h_n(\tau)$ defined as in equation (4.10) and the expansion taken at the mid-point of the time window T or $\tau_o = 0$ results in a closed form expansion as

$$t \approx \frac{|\bar{x}_n|}{c} + \left(1 - M \frac{x_{1n}}{|\bar{x}_n|}\right) \tau \quad -T/2 \leq \tau \leq T/2 \quad (4.12)$$

with $M=U/c$.

The linear term, $h_{no} = |\bar{x}_n|/c$, of the expansion is just the delay time from the source to the microphone at $\tau = 0$. The scaling term, $h_{nr} = 1 - M x_{1n}/|\bar{x}_n|$, is related to the projection of the source velocity in the source-microphone direction, $M_{sn}(0)$ at the expansion time $\tau = 0$. Note that when the microphone is directly underneath the source $h_{nr} = 1$ then the Doppler amplification factor vanishes.

Thus, the goal is to estimate the FT of the stationary source strength signal from the FT of the Dopplerized (non-stationary) microphone signal using the linear, translation, and scaling properties of the FT. This computation is performed by relating the source strength signal and the microphone signal to the original signal and the scaled signals shown in , respectively. Furthermore, as the signal propagates from the source to the microphone its amplitude decreases due to spherical spreading by $1/4\pi |\bar{x}_n - \bar{x}_s|$. Therefore, the original source strength signal and the Dopplerized microphone signal are related as,

$$q(\tau) = p_n(t) 4\pi |\bar{x}_n - \bar{x}_s(\tau)| \quad \begin{cases} -T/2 \leq \tau \leq T/2 \\ -T_{reception}/2 \leq t \leq T_{reception}/2 \end{cases} \quad (4.13)$$

where the range for the emission and reception times are explicitly indicated in equation (4.13).

We can now approximate the source strength signal in terms of the emission time using equation (4.11). That is

$$p_n(t) \approx \left(\frac{1}{4\pi |\bar{x}_n - \bar{x}_s(\tau)|} \right) q(h_{no} + h_{nr}\tau) \quad (4.14)$$

Note that in eq.(4.14), the term $1/4\pi |\bar{x}_n - \bar{x}_s(\tau)|$, is the multiplying factor κ in eq.(4.1).

To relate the FT of the source signal to the FT of the microphone signal, we need to take the FT of equation (4.14) over the reception time window $T_{reception}$. To this end, we need to extract from the total microphone signal only the part that is produced by the source over the time window T prior to taking the FT. This reception time window can be computed exactly using equation (4.10) rather than the approximation in equation (4.11). This process is schematically illustrated in Figure 4.4.

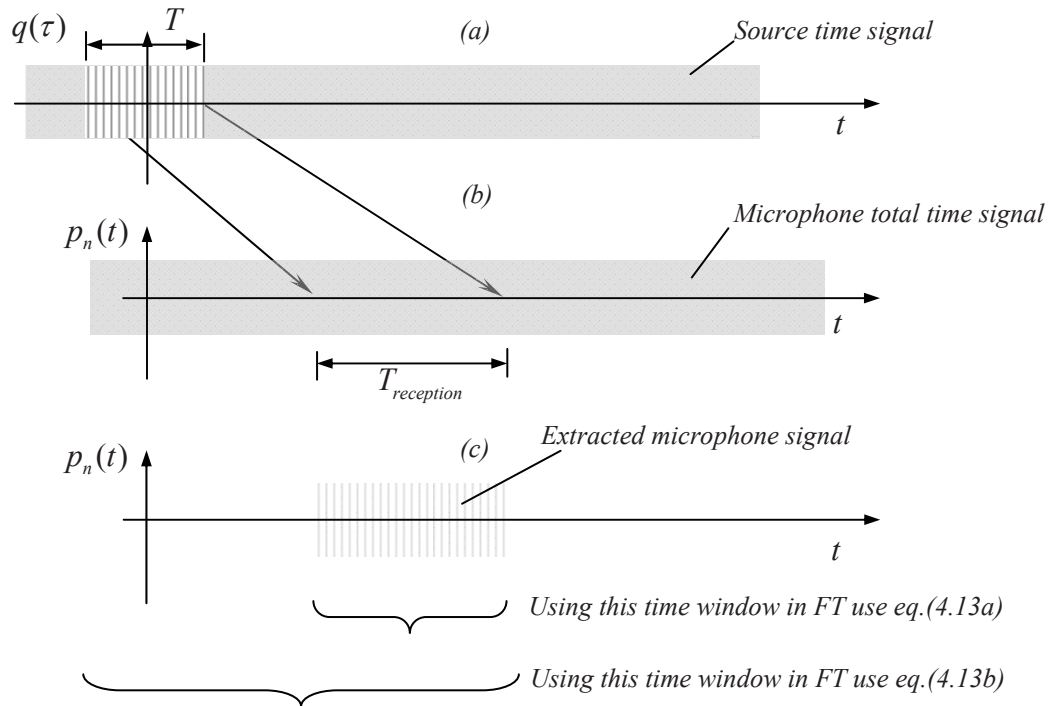


Figure 4.4: Extraction of the microphone signal that is associated to the emitted sound by the source during time window T .

The time dependence of the source-microphone distance complicates the computation of the FT. The simplest approach is to approximate the source-microphone distance by using time independent quantities such as taking its value at the mid-point of the trajectory over the time interval T . This approach is acceptable since for beamforming the relative phase between microphones is more important than the magnitude of the signals. That is,

$$|\bar{x}_n - \bar{x}_s(\tau)| \approx |\bar{x}_n - \bar{x}_s(0)| \quad (4.15)$$

Note that $\bar{x}_s(0) = 0$ since we selected to place the origin of the coordinate system at the source at time $\tau = 0$. Then, taking the FT of the microphone extracted signal (Figure 4.4c) over only the time window $T_{reception}$ leads to

$$FT\{p_n(t, T_{reception})\} \approx \left(\frac{1}{4\pi |\bar{x}_n - \bar{x}_s(0)|} \right) FT\{q(h_{no} + h_{nr}\tau, T)\} \quad (4.16)$$

and using the linear, translation, and rescaling properties of the FT described in section 4.2, the FT of the stationary source strength signal is obtained according to equation (4.5) as

$$Q\left(\frac{f}{h_{nr}}, T\right) \approx \frac{h_{nr}}{\left(\frac{1}{4\pi |\bar{x}_n - \bar{x}_s(0)|}\right)} P_n(f, T_{reception}) \quad (4.17)$$

if the FT is computed over the time window $T_{reception}$, or

$$Q\left(\frac{f}{h_{nr}}, T\right) = \frac{h_{nr}}{\left(\frac{1}{4\pi |\bar{x}_n - \bar{x}_s(0)|}\right)} e^{j2\pi\left(\frac{f}{h_{nr}}\right)h_{no}} P_n(f, T_{reception}) \quad (4.18)$$

if the FT is computed over a time window encompassing both the time window T and $T_{reception}$ as illustrated in Figure 4.4.

Comparing eq.(4.6) to (4.18), it is clear that the term $1/4\pi|\bar{x}_n - \bar{x}_s(\tau)|$, h_{no} , and h_{nr} in eq.(4.18) correspond to κ , α , and β in eq.(4.6), respectively.

It is also important to mention that in equations (4.17) and (4.18), the value of the term $h_{nr} = (1 - M_{sn}(0))$ is always positive. Furthermore, $h_{nr} < 1$ for the source approaching the microphone, $h_{nr} = 1$ when the source is immediately above the microphone, and $h_{nr} > 1$ for the source moving away from the microphone. More relevant is that this term is thus identical to the Doppler amplification factor in equation (4.8) evaluated at the center of the time window, e.g. $|1 - M_{sn}(0)|$. Thus, it can be observed that the proposed approach automatically removes the Doppler amplification factor at least in an approximated way.

In equations (4.17) and (4.18), the FT of the source strength is estimated from the microphone FT including the Doppler effect. However, using the translation and scaling properties of the FT it was removed without the need to de-Dopplerize the time signal. In other words, the de-Dopplerization was carried out in the frequency domain without the need to resample the data.

It is important to understand the advantages, approximations, and limitations in this formulation. They are:

- a. Firstly, the shorter the emission time window the reception-emission relationship is closer to be linear. However, the frequency resolution for the DFT will be degraded. Thus, there is a trade-off between frequency resolution, accuracy, and computation effort.
- b. Secondly, unlike in the time domain approach there is no interpolation of the data which is the time consuming part of the time domain approach. This suggests that we will still need to sample at relative high frequency, i.e. oversample.
- c. Thirdly, a source moving at variable speed can be easily accounted for such as by taken the average speed in the time window. Finally, the obvious advantage is the computationally efficiency of the frequency domain approach.

For convenience, the source was assumed to be a monopole in this derivation. However, directivity of the source can be easily included in the derivation by multiplying the source strength by the directivity index in the direction of the source-microphone, e.g. $d_{sn}(\tau)$. Once again the value of the directivity index can be taken to be constant at the mid-point of the time window. Generally, the directivity of the sought sources is unknown and thus a monopole assumption is typical.

4.4 Beamformer Implementation

The approach described in the previous section allowed estimating the FT of the source signal from the FT of the microphone signal. However, the number and position of the sources are unknown. So the estimate of the sources location and spectrum must be obtained by implementing a beamformer. Figure 4.5 shows a moving vehicle (airplane, car, etc.) generating noise from multiple sources moving in linear motion at a speed U . A grid of candidate source locations is shown attached to the vehicle. In other words, the grid has the same motion as the vehicle. A microphone phased array with N_{mic} elements is also shown to identify individual noise sources from the vehicle, e.g. source 1 and 2 in the illustration of Figure 4.5.

From the development in the previous section, it is clear that beamforming at the source is the most logical approach, e.g. the frequency domain de-Dopplerization developed in section 4.2. yields the FT of the source strength.

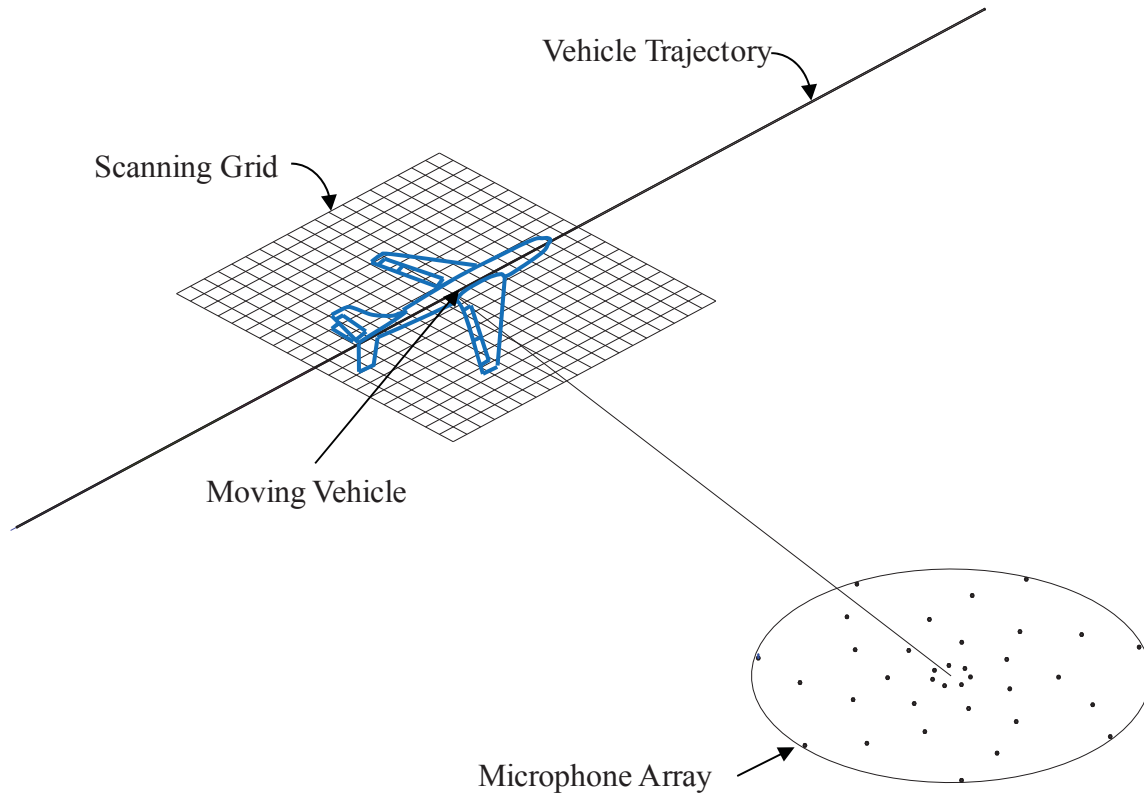


Figure 4.5: Schematic of grid moving with the vehicle over time window T .

To this end, the source trajectory is broken down into a series of short-time windows. Without loss of generality, the windows are all assumed to be of the same length. We consider the single s^{th} short-time window T where the vehicle and grid have moved a distance UT . The position of the vehicle/grid and the array shown in Figure 4.5 is assumed to be at the mid-point of the window. Thus, the emission time again ranges from $-T/2 \leq \tau \leq T/2$. Let us now consider an arbitrary grid point position at $\vec{x}_\ell(0)$ and a microphone in the array positioned at \vec{x}_n . Assuming that there is a source at this grid point, the FT of the source strength estimated from the n^{th} microphone is

$$Q_{\ell ns}(\hat{f}) = d_{\ell ns} \gamma_{\ell ns} P_{ns} \left(\frac{f}{h_{\ell-n\tau}} \right) \quad (4.19)$$

with

$$\begin{aligned}
d_{\ell ns} &= \frac{1}{e^{-j2\pi f/h_{nr} h_{no}}} \quad \text{or} \quad d_{\ell ns} = 1 \\
\gamma_{\ell ns} &= 4\pi |\bar{x}_{ns} - \bar{x}_{\ell s}(0)| h_{\ell ns\tau} \\
h_{\ell ns0} &= \frac{|\bar{x}_{ns} - \bar{x}_{\ell s}(0)|}{c} \\
h_{\ell ns\tau} &= \left(1 - M \frac{[x_{1ns} - x_{1\ell s}(0)]}{|\bar{x}_{ns} - \bar{x}_{\ell s}(0)|} \right)
\end{aligned} \tag{4.20a-d}$$

and the subscripts ℓns indicates the ℓ^{th} grid point, n^{th} microphone, and the s^{th} time window. The phase correction term $d_{\ell ns}$ to be used depends on how the FT is implemented as presented in the previous section in equations (4.13).

In addition, the de-Dopplerized frequency $\hat{f} = f/h_{\ell ns\tau}$ is theoretically the same for all microphones. That is

$$\hat{f} = f/h_{\ell,1\tau} = f/h_{\ell,2\tau} = \dots = f/h_{\ell,n\tau} = \dots = f/h_{\ell,M\tau} \tag{4.21}$$

It will be shown in the numerical examples in Chapter 5 that the frequencies estimated from the different microphones are not exactly the same due to the linear approximation. However, all of them are located within a narrow bandwidth. Moreover, in source localization of aerodynamic sources is common practice to work in frequency bands such as 1/12th, 1/3rd octave bands. Thus, from the practical point of view equation (4.19) is assumed valid, i.e. the de-Dopplerized frequencies are all within the bandwidth.

Equation (4.19) is now applied to all the microphones in the array and then the average FT source strength computed as

$$\bar{Q}_{\ell s}(\hat{f}, T) = \frac{1}{N_{mic}} \sum_{n=1}^{N_{mic}} \gamma_{\ell ns} d_{\ell ns} P_{ns}(\hat{f}) \quad (4.22)$$

The spectrum is then computed as

$$\begin{aligned} S_{\bar{Q}\bar{Q}, \ell s}(\hat{f}) &= \frac{1}{2} \bar{Q}_{\ell s}(\hat{f}) \bar{Q}_{\ell s}^*(\hat{f}) \\ S_{\bar{Q}\bar{Q}, \ell s}(\hat{f}) &= \left(\frac{1}{N_{mic}} \right)^2 \sum_{n=1}^{N_{mic}} \sum_{m=1}^{N_{mic}} \gamma_{\ell ns} d_{\ell ns} \gamma_{\ell ms}^* d_{\ell ms}^* \frac{1}{2} P_{ns}(\hat{f}) P_{ms}^*(\hat{f}) \end{aligned} \quad (4.23)$$

or in matrix form

$$S_{\bar{Q}\bar{Q}, \ell s}(\hat{f}) = \{w_{\ell s}\}^T \left[CSM_s(\hat{f}) \right] \{w_{\ell s}^*\} \quad (4.24)$$

where

$$\left[CSM_s(\hat{f}, T) \right] = \{P_s(\hat{f})\} \{P_s(\hat{f})\}^H \quad (4.25)$$

is the cross-spectral-matrix of the microphones for the s^{th} time window (no average),

$$\{P_s(\hat{f})\} = \{P_{1s}(\hat{f}), P_{2s}(\hat{f}), \dots, P_{ns}(\hat{f}), \dots, P_{N_{mic}s}(\hat{f})\}^T \quad (4.26)$$

is the vector of FT of the microphones for the s^{th} time window, and

$$\{w_{\ell s}\} = \{\gamma_{\ell 1s} d_{\ell 1s}, \gamma_{\ell 2s} d_{\ell 2s}, \dots, \gamma_{\ell ns} d_{\ell ns}, \dots, \gamma_{\ell N_{mic}s} d_{\ell N_{mic}s}\}^T \quad (4.27)$$

is the steering vector for the ℓ^{th} grid point and the s^{th} time window.

This process is then repeated for each of the s^{th} time windows and the spectrum averaged as

$$\langle S_{\bar{Q}\bar{Q},\ell}(\hat{f}) \rangle = \frac{1}{N_{seg}} \sum_{s=1}^{N_{seg}} S_{\bar{Q}\bar{Q},\ell,s}(\hat{f}) \quad (4.28)$$

The average source spectrum plotted for all grids point yields the acoustic maps at each frequency.

In practical application, the data in the $T_{\ell-rec}$ window must be smoothed using a filter, e.g. Hamming, Hanning, etc. filter. In addition, the time windows can be overlapped to generate a smother cross spectral matrix.

4.5 Application to Rotating Sources

The formulation for a source in linear motion developed in the previous sections can be extended to rotating sources in a straight forward manner. Figure 4.6 shows a schematic of a rotating system with angular velocity ω_r . As described in Chapter 2, the stationary coordinate system is positioned at the center of rotation on the plane of rotation. An array of grid points is defined at the plane of rotation moving with the same angular velocity.

Referring to Figure 4.7, the position and velocity of the ℓ^{th} grid point at the emission time τ is

$$\begin{aligned} \vec{x}_\ell(\tau) &= r_\ell \cos(\omega_r \tau + \phi_\ell) \vec{e}_1 + r_\ell \sin(\omega_r \tau + \phi_\ell) \vec{e}_2 \\ \vec{v}_\ell(\tau) &= -\omega_r r_\ell \sin(\omega_r \tau + \phi_\ell) \vec{e}_1 + \omega_r r_\ell \cos(\omega_r \tau + \phi_\ell) \vec{e}_2 \end{aligned} \quad (4.29a,b)$$

where r_ℓ and ϕ_ℓ are the grid point coordinates at $\tau = 0$.

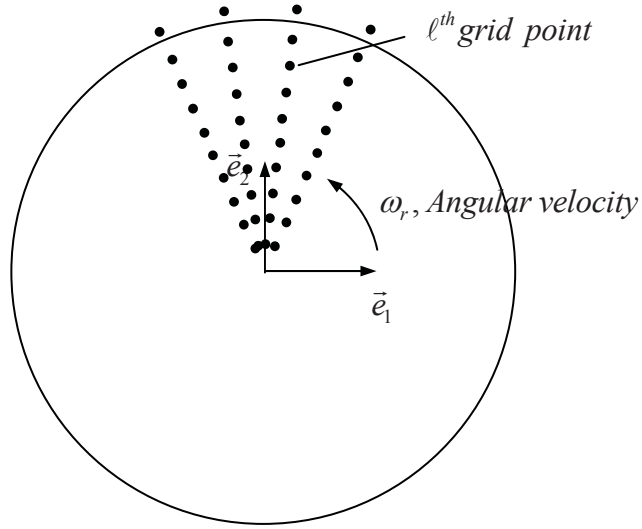


Figure 4.6: Schematic of the scanning grid points moving (rotating) with the same source angular speed.

The relationship between the emission and reception times for the ℓ^{th} grid point and the n^{th} microphone positioned at \bar{x}_n in the array is given as

$$t = \tau + \frac{|\bar{x}_n - \bar{x}_\ell(\tau)|}{c}$$

$$t = \tau + \frac{\sqrt{\{x_{1n} - r_\ell \cos(\omega_r \tau + \phi_\ell)\}^2 + \{x_{2n} - r_\ell (\omega_r \tau + \phi_\ell)\}^2 + x_{3n}^2}}{c} \quad (4.30)$$

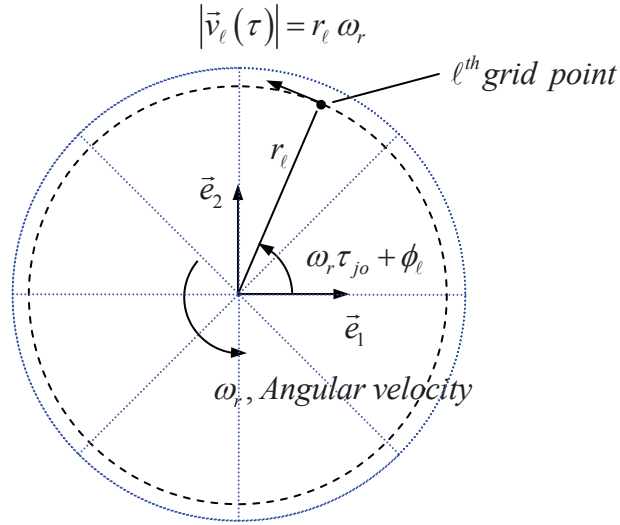


Figure 4.7: Schematic of the approximation of the circular trajectory into a sequence of linear segments.

To use the translation and scaling properties of the FT, the reception times must be expressed as a linear function of the emission times over a short-time window. To this end, the trajectory of the grid point is broken down in a set of N_{seg} equal intervals or segments over a revolution such as the 8 segments illustrated in Figure 4.7. Thus, the emission time window for a segment is given as

$$T = \frac{2\pi}{N_{seg} \omega_r} \quad (4.31)$$

The emission time at the center of the time windows is

$$\tau_{jo} = \frac{(2j-1)\pi}{N_{seg} \omega_r} \quad j = 1, 2, \dots, N_{seg} \quad (4.32)$$

while the upper and lower limits of the emission time window are

$$\tau_{j \begin{cases} \text{lower} \\ \text{upper} \end{cases}} = \frac{(2j-1)\pi}{N_{seg}\omega_r} \mp \frac{\pi}{N_{seg}\omega_r} \quad j=1,2,\dots,N_{seg} \quad (4.33a,b)$$

The corresponding lower and upper edge of the n th microphone reception time window is easily computed using equation (4.30) evaluated at the upper and lower emission limits from equations (4.33a,b). Figure 4.8 illustrates the correspondence between the emission and reception time windows over a revolution of the system.

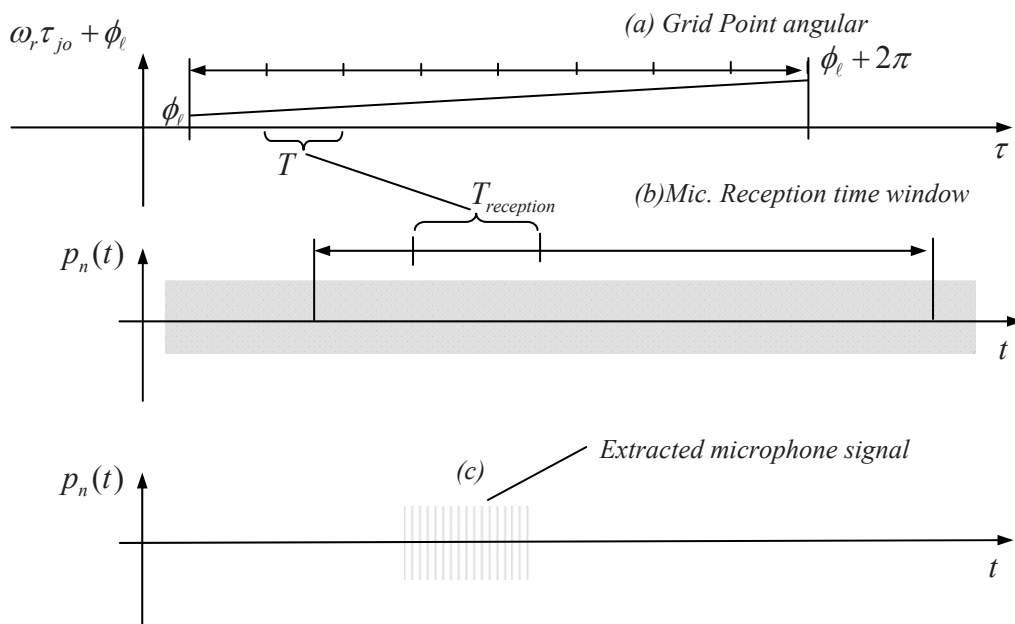


Figure 4.8: Extraction of the microphone data at reception time for each emission time window for a source moving along a circular trajectory.

As before, the microphone signal over the reception time window $T_{reception}$ must be extracted and then de-Dopplerized using the translation and scaling properties of the FT. To this end, a linear approximation to equation (4.30) is required. Taking the Taylor's series expansion around $\tau_0 = 0$, leads to (see Appendix A.1.6)

$$t \approx h_{no} + h_{nr}\tau \quad (4.34)$$

where

$$\begin{aligned}h_{no} &= \frac{|\vec{x}_n - \vec{x}_\ell(0)|}{c} \\h_{n\tau} &= 1 - M_{sn}(0)\end{aligned}\tag{4.35a,b}$$

The procedure to implement the beamformer is then the same as for the case of linear motion.

Chapter 5

Numerical Validation of the New Beamforming Method

This chapter presents a numerical validation of the new frequency domain beamforming method. The objectives of this validation are: 1) To demonstrate the accuracy of the linear approximation of the reception time for purposes of computing the relative phase between microphones, 2) to show the validity of the de-Dopplerization technique, 3) to assess the computational efficiency of the new method as compared to the traditional time domain beamforming method, 4) to assess the performance of the new frequency domain method with respect to various parameters such as source velocity, emission frequency, emission angle, noise in the microphone signals, multiple sources, and processing time compared to the traditional time domain beamforming approach.

A description of the methodology used to validate the new frequency domain beamforming code is first presented. Then, the various parameters are studied and finally the strengths and limitations of the new method are explained.

5.1 The Relative Phase between Microphones

From the point of view of beamforming, the most important information is the relative phase between the microphones in the array. This is the critical variable for an accurate beamforming. In the process of de-Dopplerization of the microphone signals using the linear approximation, the term $\frac{1}{e^{-j2\pi h_{no} f/h_{nr}}}$ in equation (4.18) corrects the phase of the microphone signal. From equation (4.12), it can be observed that the constant term of the linear expansion h_{no} is

$$h_{no} = \frac{|\vec{x}_n - \vec{x}_s(0)|}{c} \quad (5.1)$$

implying that the position of the source at $\tau = 0$ is used to determine the correction in the time delay from the source to the microphone, or phase delay.

To gain more insight, the linear approximation of the reception time in terms of the emission time is further analyzed here. To this end, a simple example for the case of two microphones positioned directly underneath the path of the source as shown in Figure 5.1 is analyzed. The n^{th} and m^{th} microphones are at $(40,0,60)$ and $(60,0,60)$, the time window is $T=0.3$ sec and the source is moving at 125 m/s ($M=0.364$). During the time window, the source moves from $-18.75 \vec{e}_1$ at $\tau = -T/2$ to $18.75 \vec{e}_1$ at $\tau = T/2$, e.g. $UT/2 = 18.75m$. The time delay between the source and microphones are shown in Figure 5.2 using the exact expression and the linear approximation. As expected the linear approximation degrades as the linear expansion moves away from the expansion point $\tau = 0$.

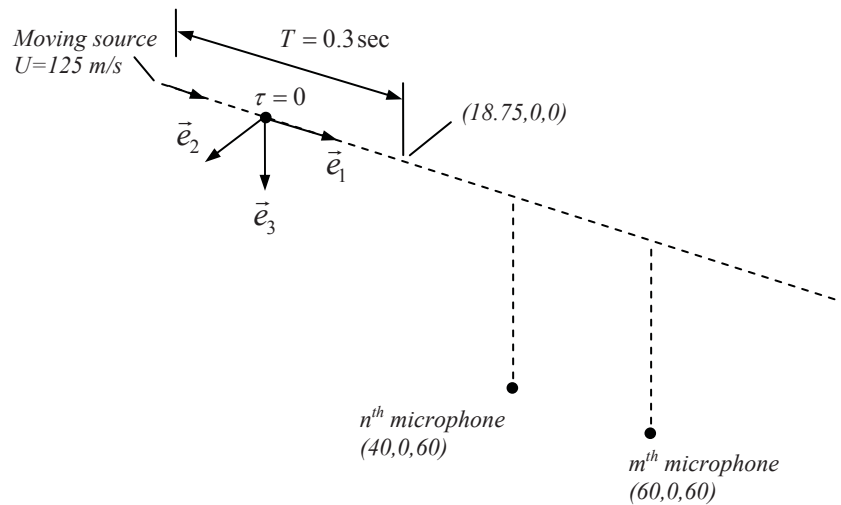


Figure 5.1: Example used to illustrate the relative phase between microphones using the linear approximation for the reception times.

Figure 5.3 shows the relative time delay between the microphones. From the beamforming point of view, this is the most important variable. It is again clear that for this case the linear approximation is very good near the expansion point.

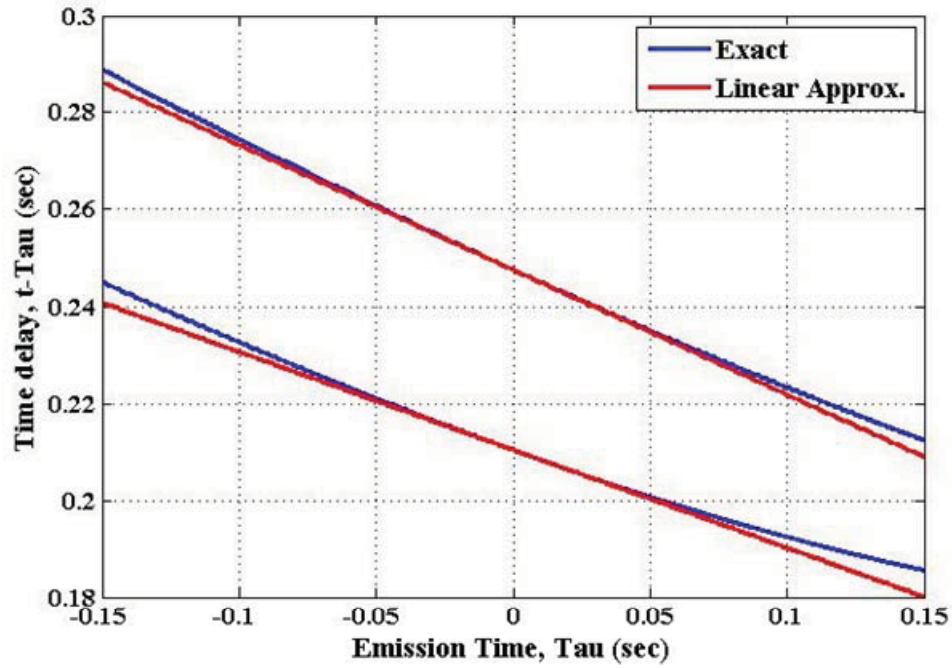


Figure 5.2: Time delay $|\bar{x}_n - \bar{x}_s(\tau)|/c$ as a function of the emission time τ exact and linear approximation.

Case: source at $x_{n1} = 40m$ and $x_{m1} = 60m$ at $\tau = 0$ and $T=0.3$ sec.

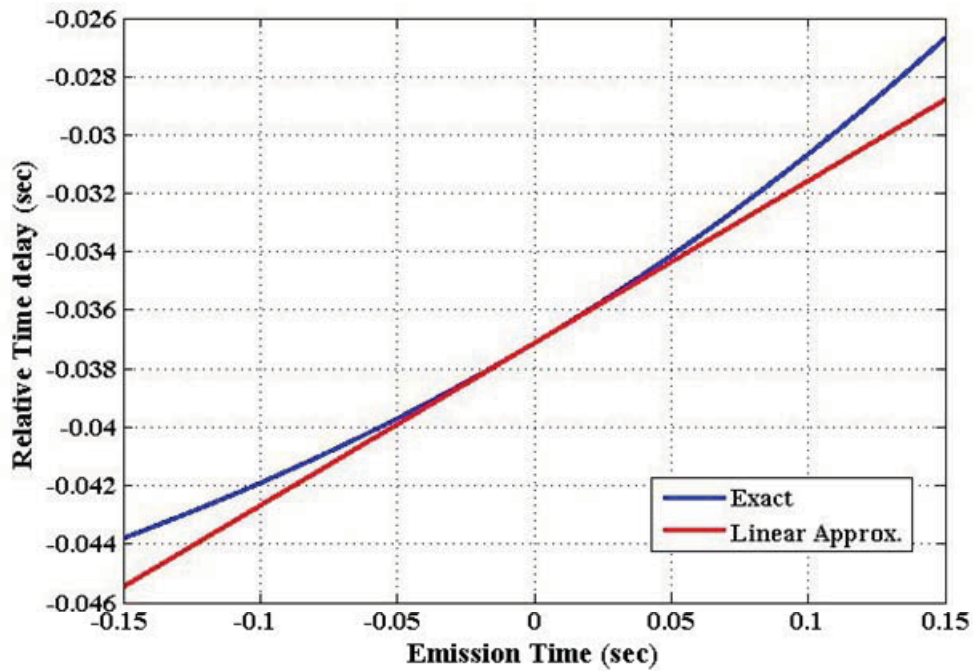


Figure 5.3: Relative time delay between microphones, $|\bar{x}_n - \bar{x}_s(\tau)|/c - |\bar{x}_m - \bar{x}_s(\tau)|/c$ as a function of the emission time τ exact and from linear approximations. Case: source at $x_{n1} = 40m$ and $x_{m1} = 60m$ at $\tau = 0$ and $T=0.3$ sec.

The same set of results is shown in Figure 5.4 through Figure 5.6 for the case of a new time window closer to the microphones, e.g. $x_{n1} = 0m$ and $x_{m1} = 30m$ at $\tau = 0$. In fact, during the time window T the source crosses the plane of the n th microphone (at $\tau = 0$ the source is directly on top of the n th microphone). Figure 5.5 shows that the linear approximation is only reasonable very close to the expansion point. However, the relative time delay between the microphones shown in Figure 5.6 is still very good. The main conclusion from this analysis is that the linear approximation is accurate for the purpose of computing the relative phase between the microphones.

Another important observation is that implementing a smoothing window to the data before the DFT, e.g. Hanning windows, eliminates the less accurate data in the processing.

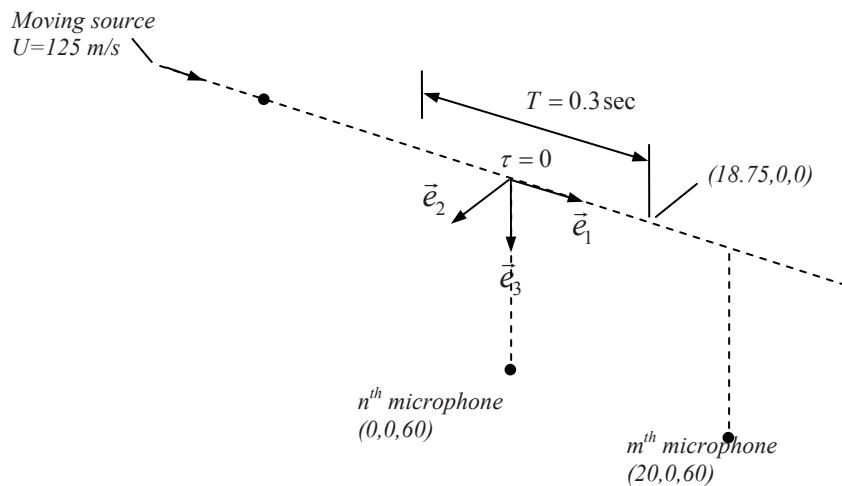


Figure 5.4: Example used to illustrate the relative phase between microphones using the linear approximation for the reception times (Source passing over one microphone).

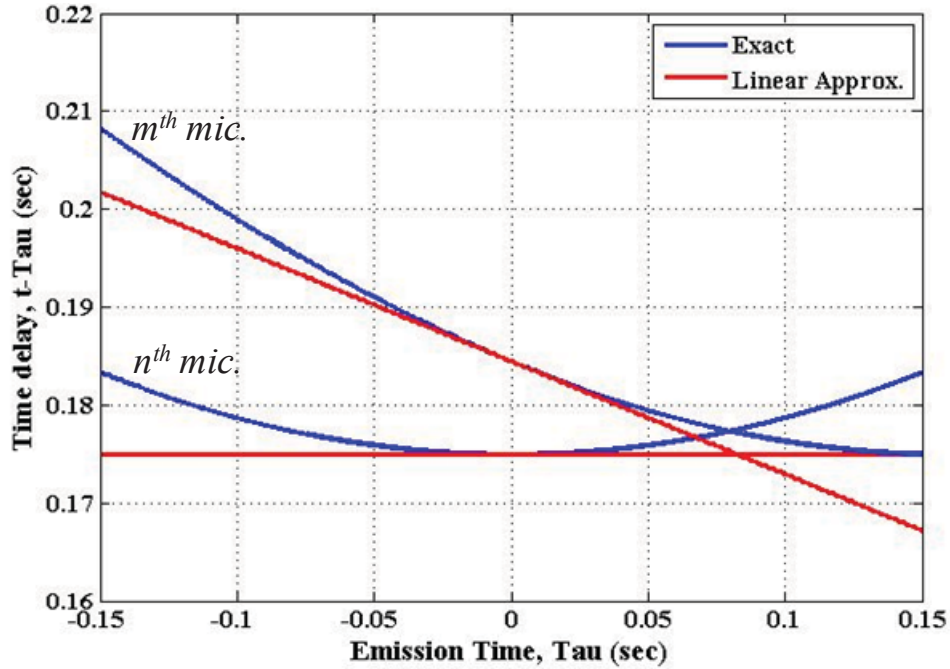


Figure 5.5: Time delay $|\bar{x}_n - \bar{x}_s(\tau)|/c$ as a function of the emission time τ exact and linear approximation.

Case: source at $x_{n1} = 0m$ and $x_{m1} = 20m$ at $\tau = 0$ and $T=0.3$ sec.

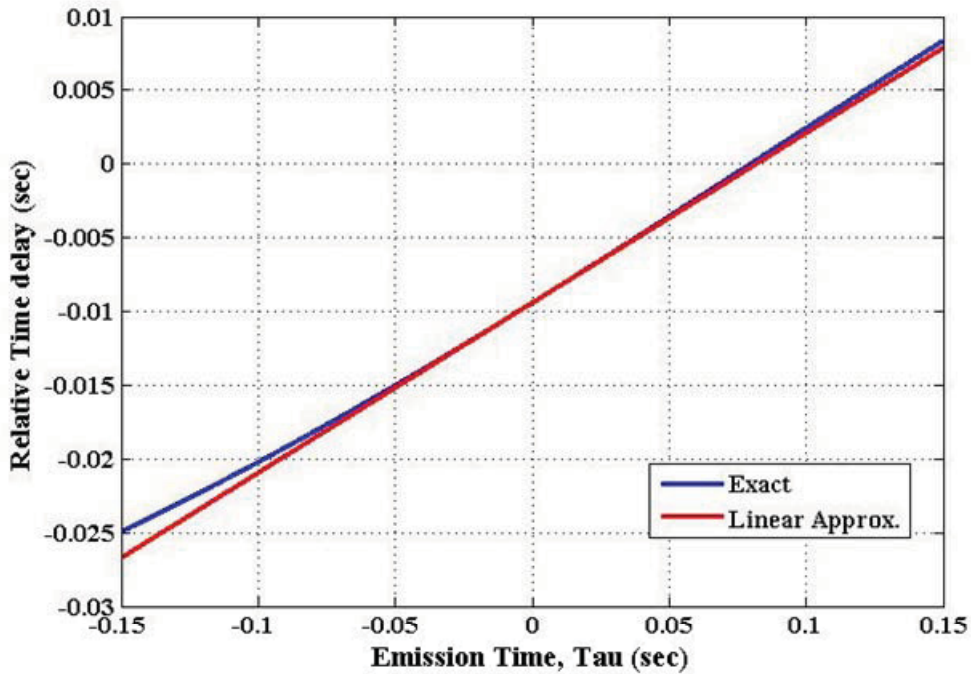


Figure 5.6: Relative time delay between microphones, $|\bar{x}_n - \bar{x}_s(\tau)|/c - |\bar{x}_m - \bar{x}_s(\tau)|/c$ as a function of the emission time τ exact and from linear approximations.

Case: source at $x_{n1} = 0m$ and $x_{m1} = 20m$ at $\tau = 0$ and $T=0.3$ sec.

5.2 Validation of the de-Dopplerization Technique

This section focuses on assessing the accuracy of the frequency domain de-Dopplerization technique. To this end, consider the source shown in Figure 5.7. The sound radiated by this source consists of three pure tones at 1000 Hz, 1250 Hz, and 1600 Hz with amplitudes of 10000, 9000, and 8000 Kg/s^2 , respectively. The source moves in the \bar{x}_1 -direction with a constant velocity of 100 m/s from position (0,0,0) to position (100,0,0), and passes over a single microphone located at (50,0,50) at an altitude of 50 meters. The source position signal and the microphone signal are both sampled simultaneously at a sampling frequency of 25600 Hz.

Figure 5.8a shows the time signal received by the microphone as the source moves 100 meters, i.e. from position (0,0,0) to position (100,0,0) whereas Figure 5.8b shows the Fourier transform of this signal. From Figure 5.8a, it can be seen that due to the source motion, the amplitude of the signal increases as the source approaches the microphone, and decreases as the source moves away from the microphone. From Figure 5.8b it is clear that the Doppler effect has distorted the frequency content of the original source signal, since the three tonal frequencies are not present in this spectrum.

To compute the de-Dopplerized source strength from the microphone signals, the source trajectory was divided into 25 segments of equal length, each segment was 4 meters long. This is equivalent to dividing the source position signal into 25 equal emission time windows of 0.04 seconds each, i.e. 1024 samples per time window. Then, the de-Dopplerized source strength signal is computed from the microphone data of the corresponding 25 reception time windows.

For clarity, the results of the de-Dopplerization computation are shown in Figure 5.9 for every other source trajectory segment. Furthermore, these results are presented in three groups as described in Figure 5.7: Approach (segments 1 through 9), Fly-over (segment 13), and Receding (segments 15 through 25).

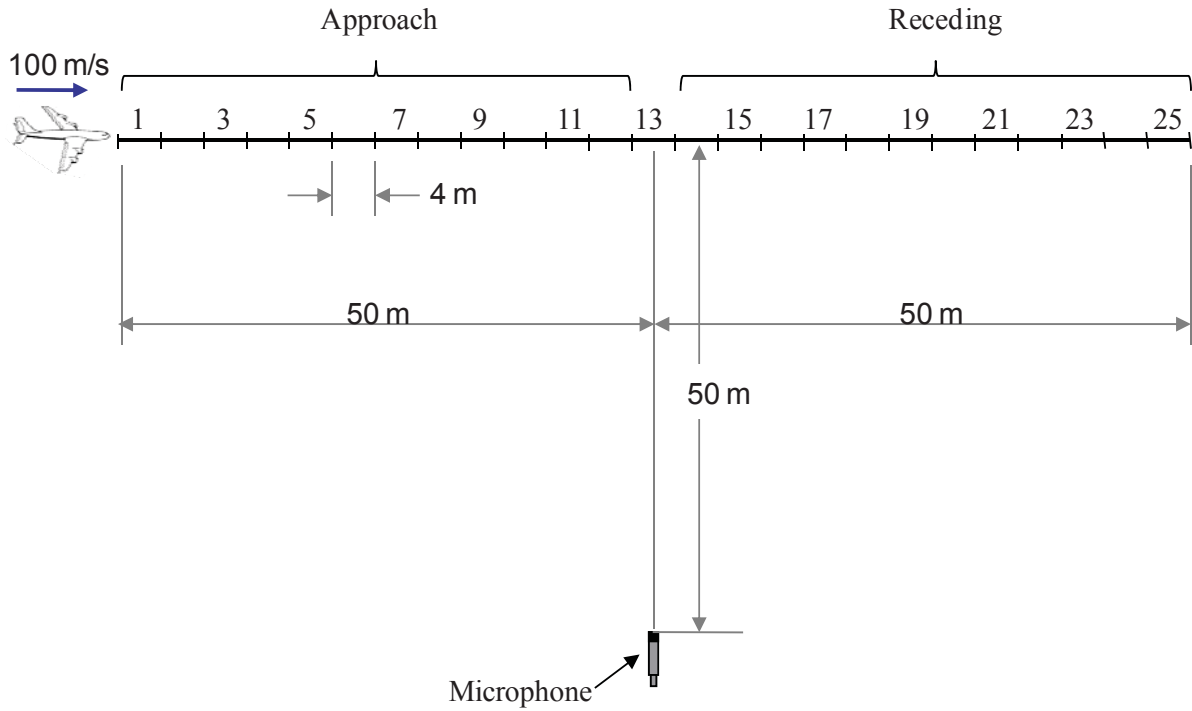


Figure 5.7: Simulated monopole source moving from position (0,0,0) to position (100,0,0), passing over a fixed microphone located at (50,0,50). The source emits sound at 1000 Hz, 1250 Hz and 1600 Hz with amplitudes of 10000, 9000, and 8000 Kg/s², respectively. To compute the de-Dopplerized source strength signal, the source trajectory is divided into 25 segments of equal length (4 meters each).

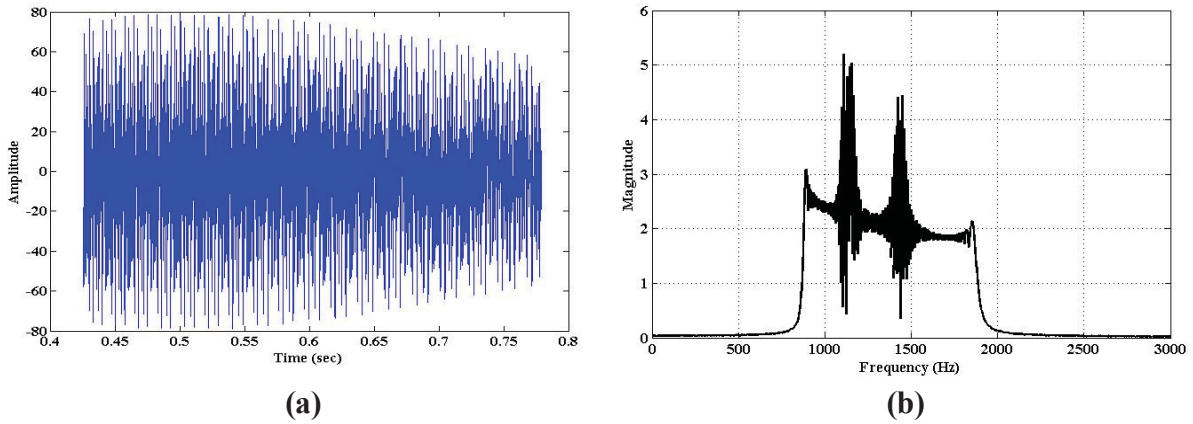


Figure 5.8: Data sampled by the microphone: (a) Original time signal sampled as the source moved 100 meters from position (0,0,0) to (100,0,0), and (b) Fourier transform of this signal.

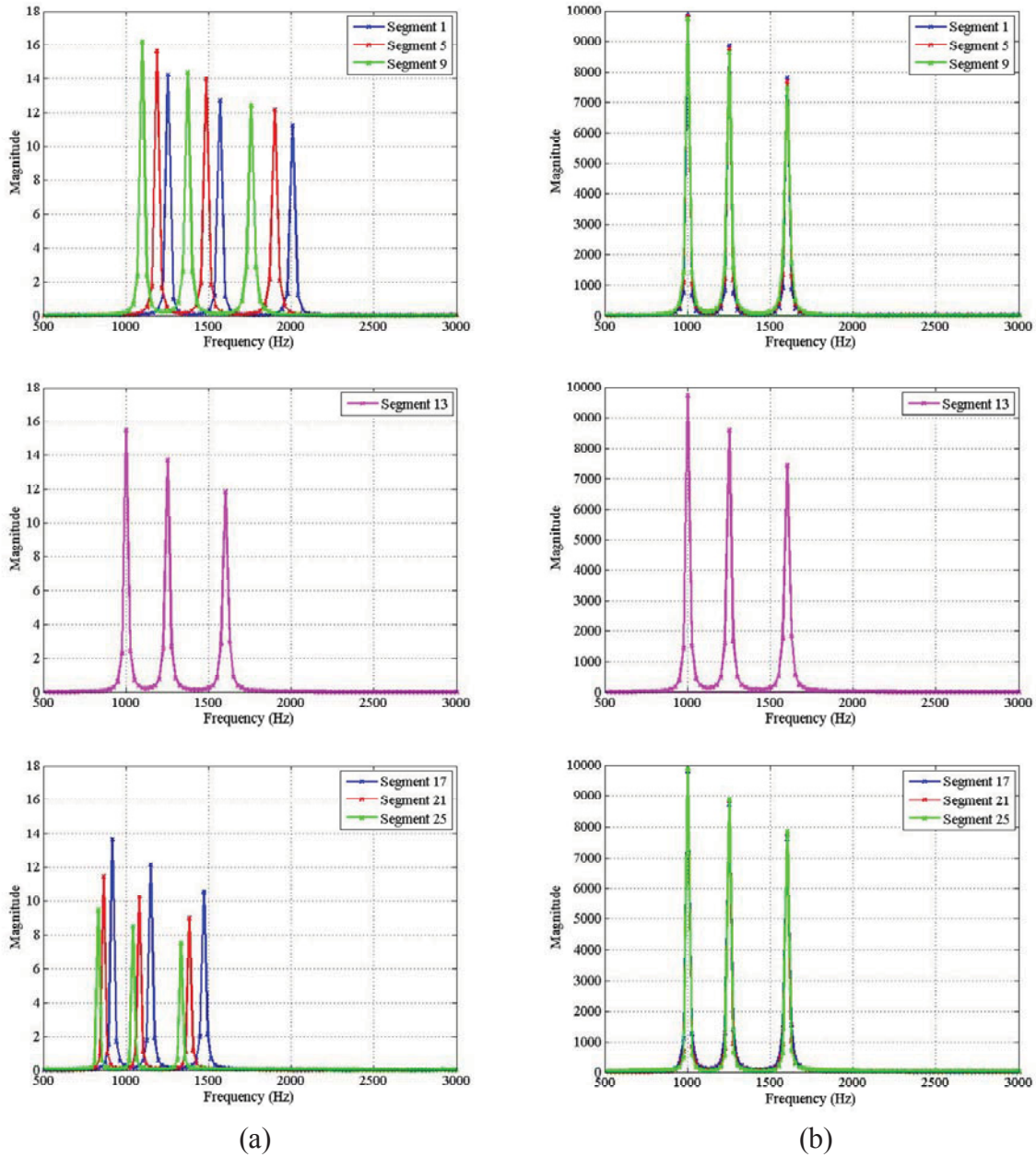


Figure 5.9: (a) Fourier transform of microphone signals with Doppler effect and (b) corresponding de-Dopplerized source strength spectra computed from each time window.

The left column of Figure 5.9 shows the Fourier transforms of the microphone signals computed from each other time window before adjusting the frequency shift and magnitude change due to the Doppler effect and also due to the spherical spreading of the acoustic signal. The figures on the right column of Figure 5.9 show the corresponding source strength Fourier transforms computed by de-Dopplerizing the microphone signals, e.g. adjusting for the

frequency shift and amplitude change. As expected, the perceived frequencies during approach (top left figure) are higher than the actual frequencies of the source. When the source is immediately above the array (Segment 13 in the middle left figure) the Fourier transform yields the correct frequencies. When the source recedes (lower left figure), the perceived frequencies are lower than the actual source frequencies. When the frequency and amplitude adjusting factors are used, all the FT shown in the left column of Figure 5.9 yield the correct source frequencies. Regarding the amplitude of the recovered source strength signals compared to the original signal, there is a reduction of approximately 0.20, 0.27, and 0.58 dB for the tones at 1000, 1250 and 1600 Hz, respectively.

5.2.1 Selection of the Time Window Length

In the previous example, the de-Dopplerization technique recovered the Fourier transform of the source strength signal for a source moving at 100 m/s (Mach 0.29) along a linear trajectory located at 50 meters from the observer (microphone). In that particular example, the source motion was divided into emission time windows of 0.04 seconds each. In this section, the effect of varying the length of the emission time window on the recovered Fourier transform of the source strength signal is studied.

The general approach for the frequency domain de-Dopplerization technique is to first divide the source trajectory into N-segments of equal length. However, there is a compromise between the time window length and the accuracy of the recovered source strength signal. In other words, the longer the time window used, the less accurate the recovered source strength signal.

The two parameters that determine the length of the time window to be used are: 1) The velocity of the source, and 2) the distance between the observer and the source trajectory. To quantify the effect of these two parameters, four different source velocities and 3 different observer-to-source trajectory distances were studied. The source velocities ranged from 50 m/s (Mach 0.15) to 200 m/s (Mach 0.58); whereas the observer-to-source trajectory distance ranged

from 30 meters to 100 meters. For all the studied cases a monopole source emitting sound in the form of a pure tone at 1000 Hz with amplitude of 10000 Kg/s^2 was simulated. The microphone and the source position signals were sampled simultaneously at 25600 Hz.

Figure 5.10 shows the de-Dopplerized Fourier transforms for the source emitting sound at 1000 Hz, plotted along with the Fourier transform of the original source strength signal. The source in this example moves at 100 m/s (Mach 0.29) along a linear trajectory located 30 meters above the observer. The de-Dopplerized Fourier transforms were computed using time window of 0.06 seconds each. Thus, during a time window the source travels 6 meters.

From Figure 5.10 it can be seen that as the source approaches and passes over the observer, the recovered Fourier transform of the source strength signal undergoes more distortion than when the source is away from the observer, either at approach or at recede. The observed distortion consists of the energy in the single spectral line at 1000 Hz in the original source strength to be leaked into the adjacent spectral line in the recovered source strength spectrum. This distortion is consistent with the observation made in Section 5.1 where the worst case scenario for the linear approximation is when the source passes over the observer. That is, as the source passes over the observer, the slope of the curve of the equation relating emission time and reception time changes from negative to positive. It is very interesting that the total power of the recovered source strength signal is preserved, i.e. the sum of the energy in the spectral lines at and around 1000 Hz is constant. Another important observation is that the dominant frequency content of the Fourier transform shown in Figure 5.10 is still correctly recovered.

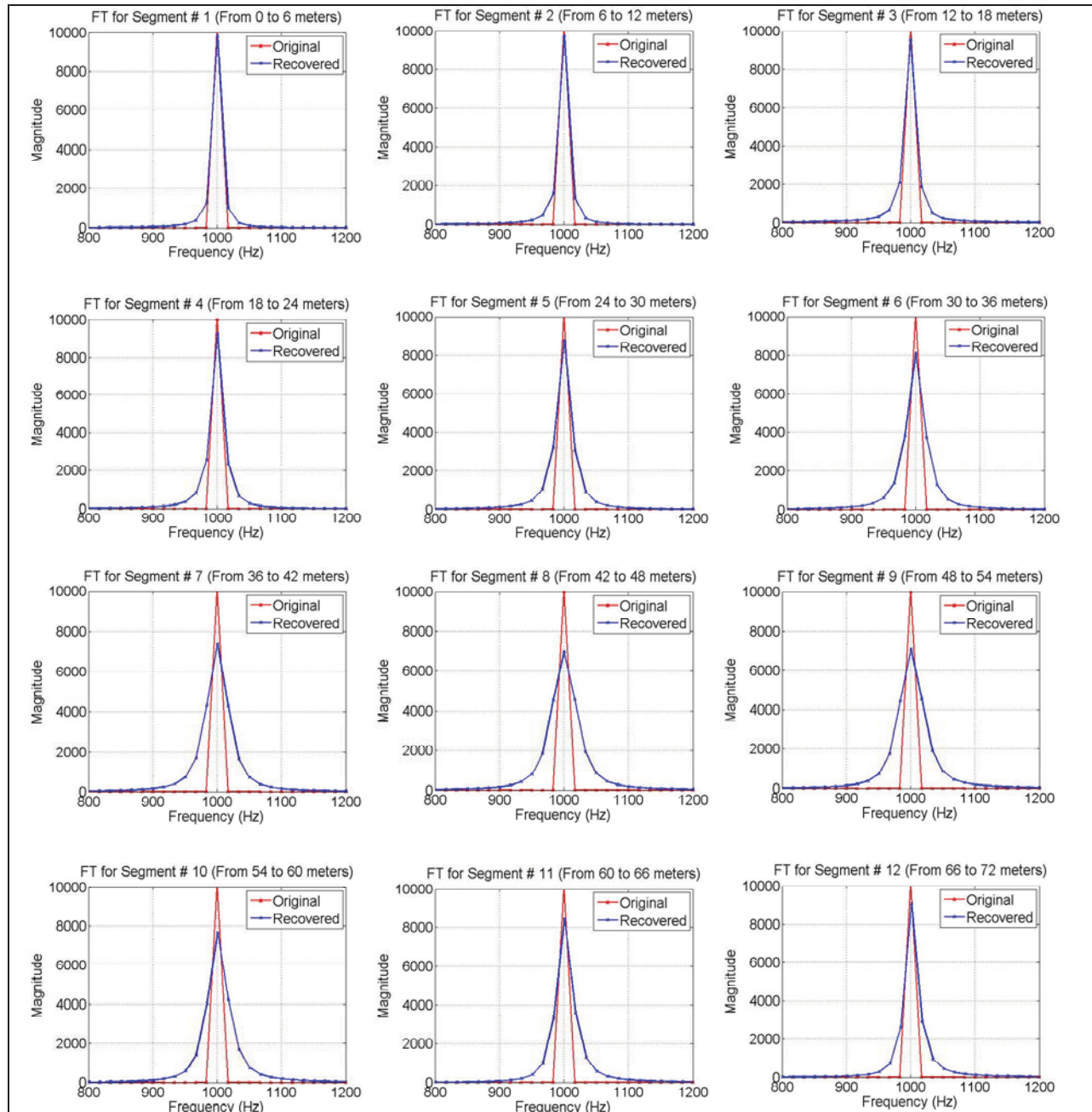


Figure 5.10: De-Dopplerized Fourier transforms of the source strength signal computed using emission *time windows of 0.06 seconds* each. (Source moving along the x-direction at 100 m/s (Mach 0.29) along a linear trajectory located at 30 meters from the observer).

Figure 5.11 shows the Fourier transforms of the de-Dopplerized source strength signal for the same case of the source moving at 100 m/s along the x-direction at 30 meters from the observer. However, these Fourier transforms were processed using emission time windows of 0.08 seconds each. From these plots, it can be seen that increasing the length of the time windows resulted in an adverse effect of the magnitude and the frequency content of the

recovered FT's of the source strength signals. From segment 5 to segment 8, the FT's of the recovered source strength signal miss the emission frequency (1000 Hz) of the original signal.

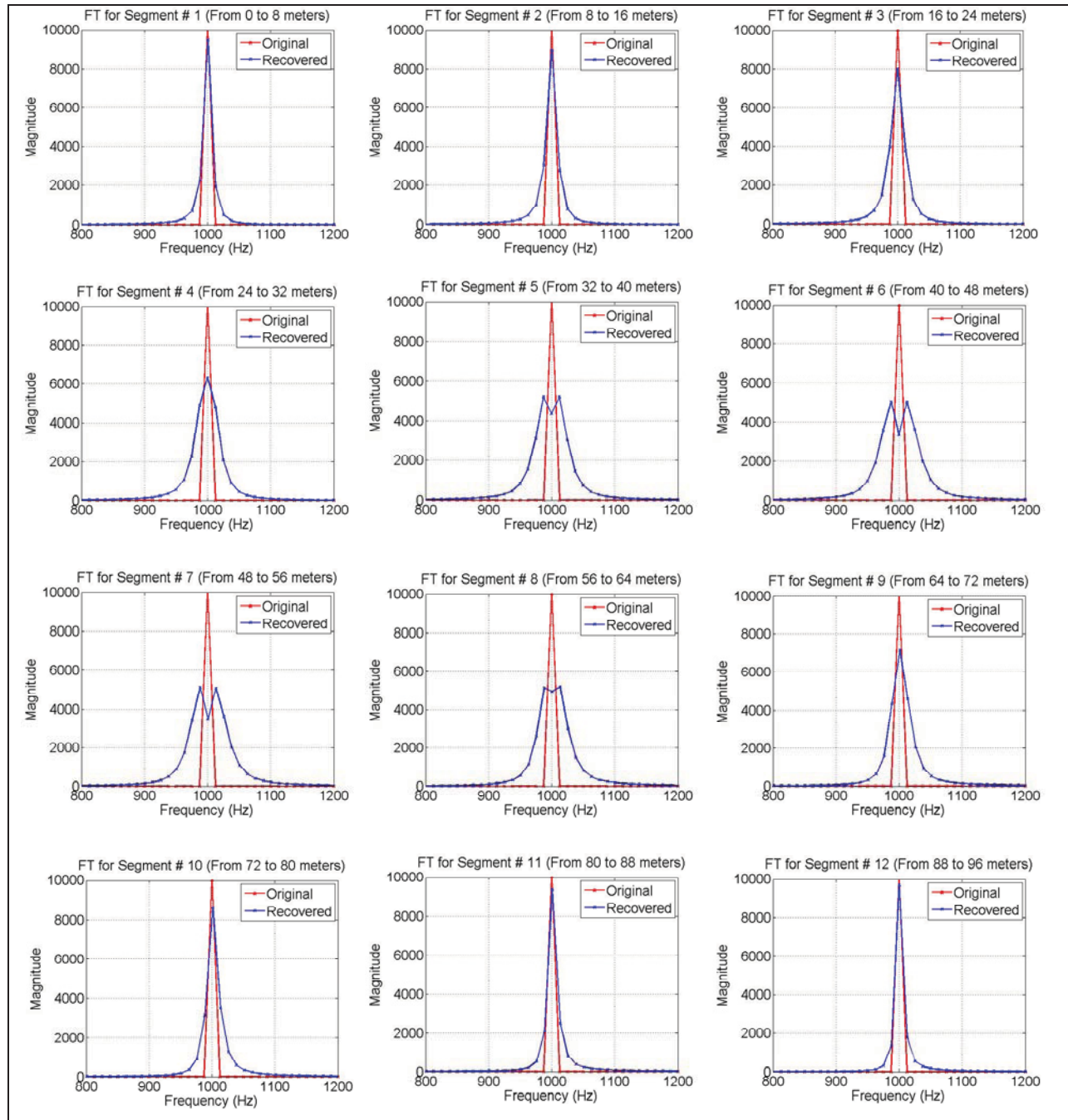


Figure 5.11: De-Dopplerized Fourier transforms of the source strength signal computed using emission *time windows of 0.08 seconds* each. (Source moving along the x-direction at 100 m/s (Mach 0.29) along a linear trajectory located at 30 meters from the observer).

The same type of analysis presented for the case of the source moving at 100 m/s was also performed for the source moving at three other velocities and moving along a linear trajectory located at three different distances from the observer. The criteria for determining the maximum time window length for each case was based on the distortion of the frequency content. That is, the maximum time window length is that which allows recovering the correct frequency content of the FT of the source strength signal such as that shown in Figure 5.10.

Figure 5.12 shows the maximum time window length as a function of source velocity (expressed in Mach) for the three different observer-to-source trajectory distances. In this figure, the criterion used to identify the maximum time window was based on the correct recovery of the source frequency.

From Figure 5.12, it can be seen that as the source velocity increases, the length of the time windows used in the de-Dopplerization technique should be decreased in order to recover the correct frequency content of the source strength signal. Note that the worst case scenario is the time window directly above the microphone (observer). On the other hand, the further the observer is from the trajectory of the source, the less pronounced is the Doppler effect. This means that longer time windows can be used also indicating that using time windows of different durations should be most effective rather than a constant one.

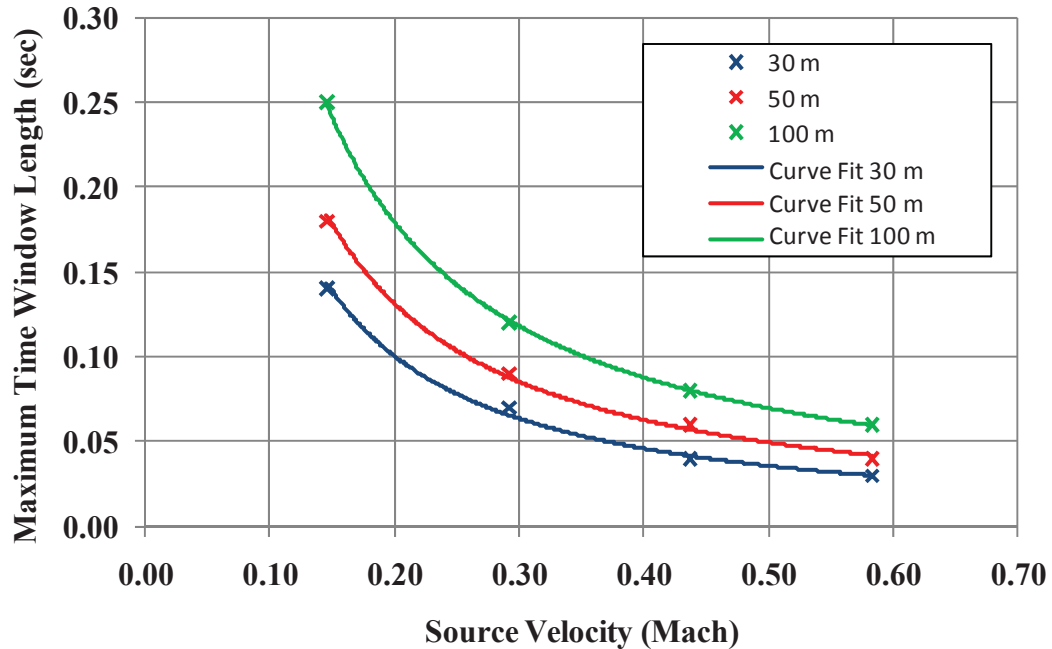


Figure 5.12: Maximum time window length for various source velocities and various observer-to-source trajectory distances. Selection of a window length below the curve for a particular source velocity allows recovering the correct frequency content of the FT of the source strength signal.

5.2.2 Uncertainty in Source Velocity

To de-Dopplerize the microphone signal, knowledge of the source position as a function of time is required. Using source position data, the velocity of the source can readily be computed. The source velocity is used to compute the Doppler amplification correction factor. In this section, the effect of uncertainty in the source velocity on the FT of the (de-Dopplerized) source strength signal is studied. To this end, a monopole source emitting sound at 1000 Hz and moving along the x-direction at four different velocities is simulated. For all these cases, the source moves from (0,0,0) to (100,0,0), while the microphone is fixed at (50,30,0).

Figure 5.13 shows the FT of the original source strength signal (red), the FT of the de-Dopplerized source strength signal using the correct source velocity (black), and the FT of the de-Dopplerized source strength signal using a source velocity that is 2% higher than the correct source velocity. From these figures it can be seen that the use of an incorrect source velocity results in a reduction of the magnitude and frequency shift of the dominant peak of the de-

Dopplerized FT of the source strength signal. However, despite the reduction of the magnitude of the dominant peak, the total energy is preserved. It can also be observed that most of the distortion in the FT of the de-Dopplerized source strength signals occurs as the source passes over the microphone.

To quantify the effect of an error in the source velocity on the computed FT of the source strength signal, a monopole source moving along the x-direction at four different velocities was simulated. Each dataset was then processed assuming an error in the source velocity ranging from 0% to 8%. For each case the maximum frequency shift between the FT of the original signal and the FT of the de-Dopplerized signal was measured. Figure 5.14 shows the maximum frequency shift between the FT of the original source strength signal and the FT of the de-Dopplerized signal due to error in the source velocity. From this figure it can be seen that the same percent error in the assumed source velocity will cause larger frequency shifts for sources moving at higher velocities, as expected. It should be noted that the error in the source velocity will affect equally both the time and frequency domain de-Dopplerization techniques.

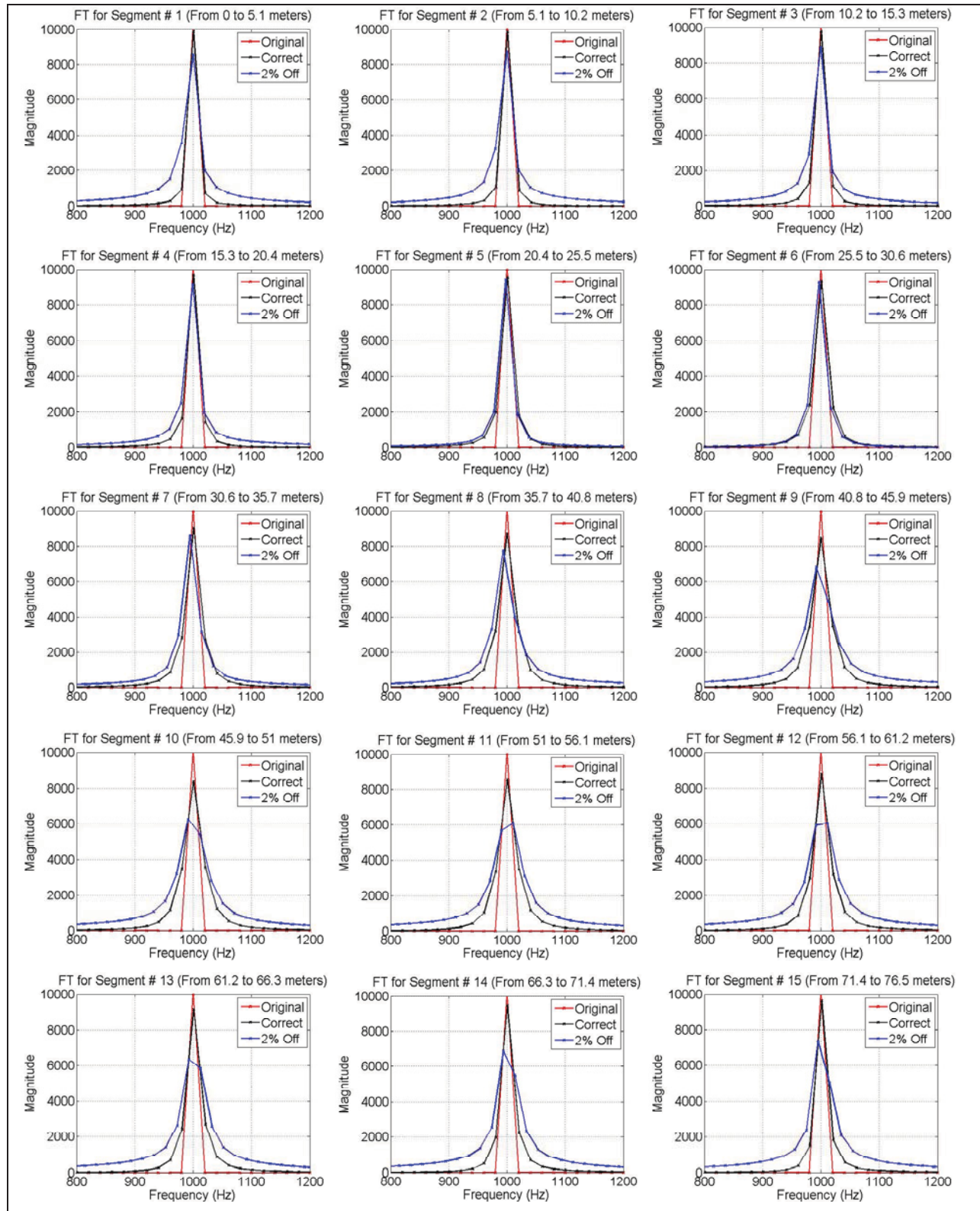


Figure 5.13: Original source strength signal (red), de-Dopplerized source strength signal using the correct source velocity (black), and de-Dopplerized source strength signal using a source velocity 2% greater than the correct source velocity. (Monopole source moving along the x-direction at 100 m/s)

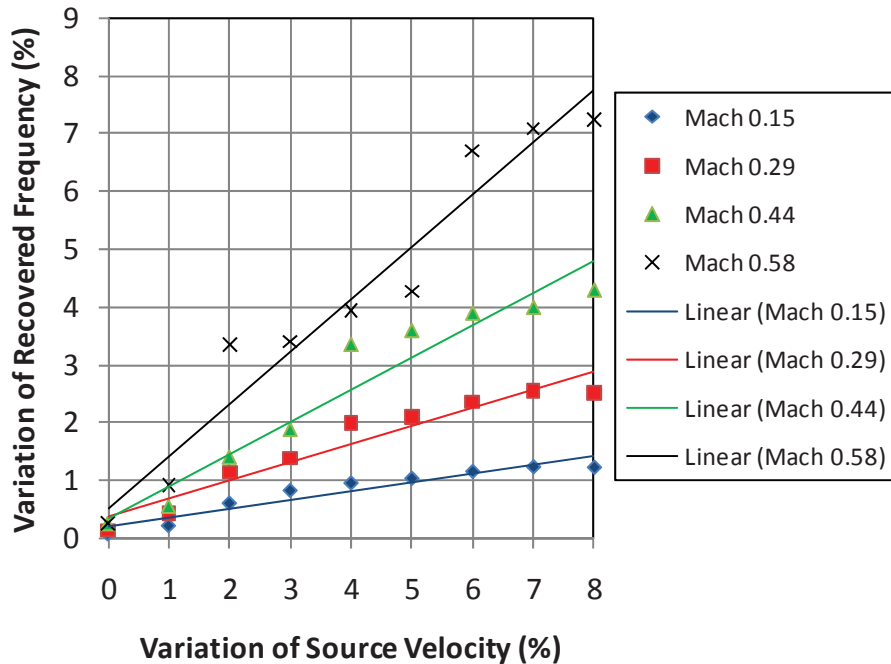


Figure 5.14: Maximum error in the adjusted frequency of the FT of the source strength signal due to uncertainty (expressed in percentage) on the source velocity.

5.2.3 De-Dopplerization of a Band-Limited Signal

In the previous sections, the de-Dopplerization technique was validated for a source emitting sound in the form of a pure tone. In this section, the validation of the de-Dopplerization technique is extended for the case of a source emitting sound in the form of a band-limited signal. To this end, a monopole source moving along the x-direction at 50 m/s emitting a band-limited random noise signal between 1000 Hz and 2000 Hz was simulated. The source moves from (0,0,0) to (100,0,0) while the observer (microphone) is fixed at (50,0,50), i.e. the microphone is located at 50 meters from the source trajectory. Both the microphone signal and the source position were sampled simultaneously at 25600 Hz.

Figure 5.15 shows the Fourier transform of the original source strength signal (red) and the de-Dopplerized source strength signal obtained from the microphone data (blue) as the source moves from (0,0,0) to (24,0,0). Similarly, Figure 5.16 shows the Fourier transform of the

original and de-Dopplerized source strength signals as the source moves from position (24,0,0) to position (48,0,0). The dataset to compute the Fourier transforms shown in Figure 5.15 and Figure 5.16 was processed by breaking down the source position signal into equal-length emission time windows of 0.04 seconds each. For the sampling frequency used of 25600 Hz, these time window lengths contain 1024 data points.

From Figure 5.15 and Figure 5.16, it can be seen that the de-Dopplerization technique recovers the original source strength signal with the correct frequency content, and in most of the cases with a small reduction in the magnitude.

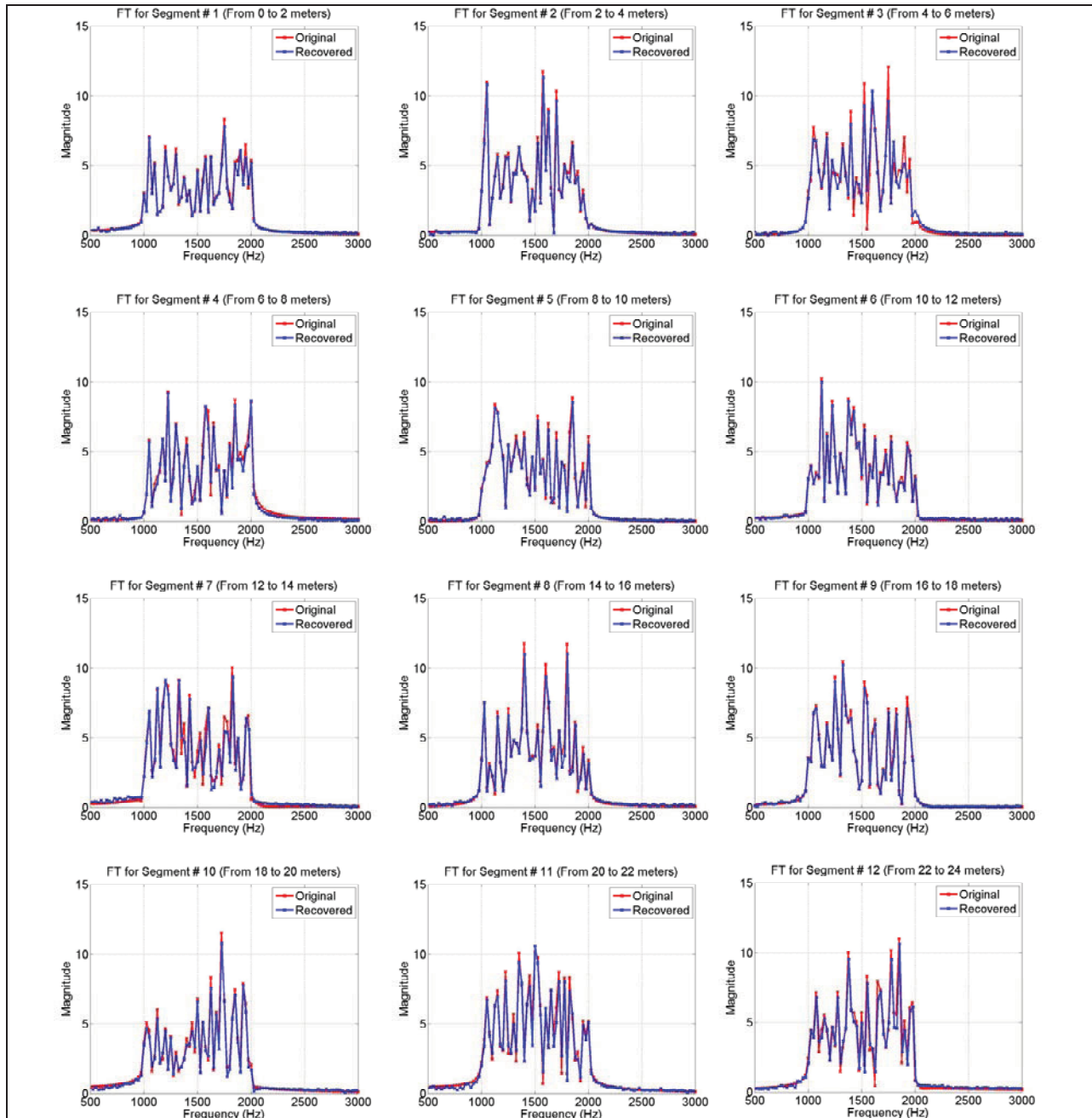


Figure 5.15: FT of the original source strength signal (red) and the de-Dopplerized signal obtained from the microphone data (blue) for a monopole source moving along the x-direction at 50 m/s and emitting sound between 1000 Hz and 2000 Hz, *as the source moves from (0,0,0) to (24,0,0)*. Data processed using equal-length emission time windows of 0.04 seconds each.

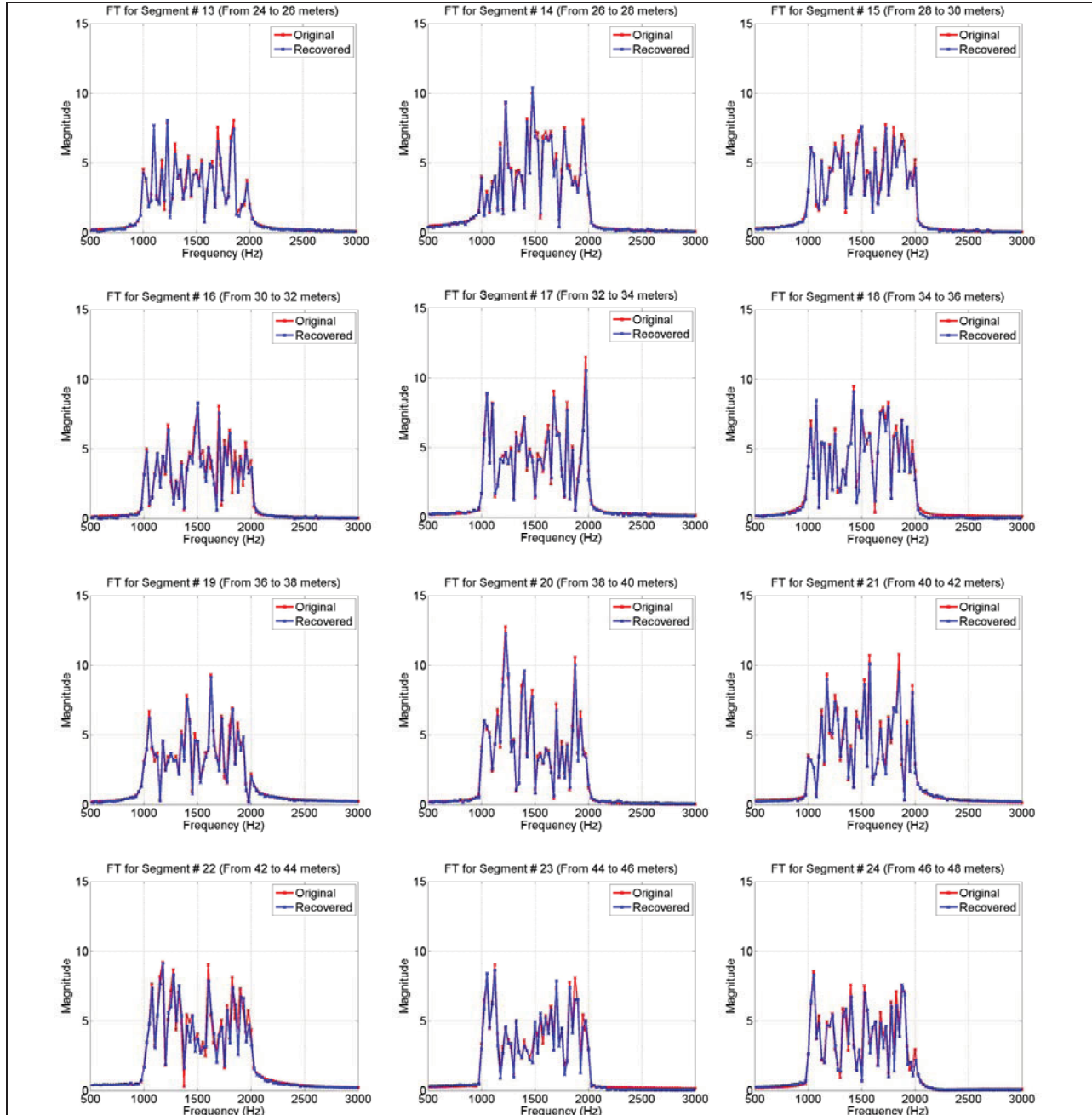


Figure 5.16: FT of the original source strength signal (red) and the de-Dopplerized signal obtained from the microphone data (blue) for a monopole source moving along the x-direction at 50 m/s and emitting sound between 1000 Hz and 2000 Hz, *as the source moves from (24,0,0) to (48,0,0)*. Data processed using equal-length emission time windows of 0.04 seconds each.

5.3 Validation of the Frequency Domain Beamforming Approach

The numerical validation was performed in two steps. First, a data generation computer program was written to simulate the acoustic pressure recorded by an array of microphones from a source moving in a plane parallel to the plane of the array. Then, the new frequency domain beamforming method was implemented in a computer code to process the simulated data.

Two cases of source motion that represent most practical applications were studied: Sources with linear motion and sources with rotational motion. The microphone array used for the numerical simulations of both cases consisted of 35 microphones distributed in 7 spiral arms with an external diameter of 10 meters. Figure 5.17 shows the microphone pattern of the array used for the numerical simulations.

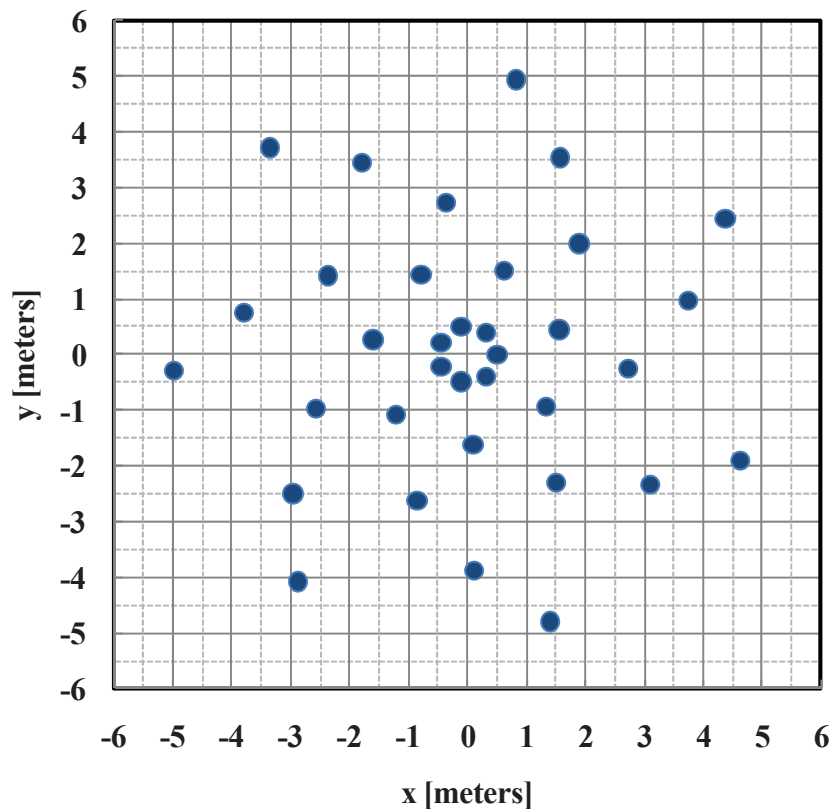


Figure 5.17: Array pattern used for the numerical simulations.

5.3.1 Data Generation Algorithm

The purpose of this algorithm is to generate data that simulates a real life situation where both the source position and the microphones signals are sampled simultaneously at equal intervals of time. To accomplish this task, the algorithm consists of the following three parts:

- 1) Generate an emission time vector, $\tau_j, j=1,2,\dots,N$ and select the initial source position, $\bar{x}_s(\tau=0)$.
- 2) For every emission time τ_j , compute the source position $\bar{x}_s(\tau_j)$, the propagation time from the source position to each microphone of the array $|\bar{x}_n - \bar{x}_s(\tau_j)|/c$, and the corresponding acoustic pressure received by the microphones, $p_n(\bar{x}_n, t_n)$. Note that the reception time for any two pairs of microphones m and n are different: $t_{m,j} \neq t_{n,j}$.
- 3) Using linear interpolation, compute the acoustic pressure received by the microphones at equally spaced intervals of time.

The output of this algorithm consists of the source position vector and the acoustic pressure at the microphones at equally spaced intervals of time.

5.3.2 New Frequency Domain Beamforming Algorithm

This algorithm is an implementation of the new frequency domain beamforming method into a computer program. The program reads the source position vector, and the microphone signals sampled at equal intervals of time. Then, for every potential source location in a scanning grid, the algorithm performs the following steps, which are shown schematically in Figure 5.18:

- 1) Divide the source position signal into M emission time windows.
- 2) For every emission time window compute the initial time t_{n_start} , and end time t_{n_end} , of the corresponding reception time window on every microphone signal.

- 3) Compute the Fourier Transform of the data contained in the reception time window and obtain a spectrum $p_n(f)$ from every microphone signal.
- 4) Apply the de-Dopplerization factors to every microphone spectrum $p_n(f)$ and obtain a de-Dopplerized source strength signal, $Q_n(f)$.
- 5) Add the spectral lines of the source strength signal, $Q_n(f)$ into 1/3-octave bands as,

$$Q_n^b(f_c) = \sum_{f=f_{lower}}^{f_{upper}} Q_n(f), \text{ where } f_c, f_{lower}, \text{ and } f_{upper} \text{ are the center, lower, and upper}$$

frequencies of the b^{th} octave band.

- 6) Add the 1/3-octave band source strength signals to obtain an average 1/3-octave band source strength signal as $\bar{Q}_l^b(f_c) = \frac{1}{N} \sum_{n=1}^N Q_n(f_c)$ for every l -th point in the scanning grid.
- 7) Compute the source strength mean square value for every point of the scanning grid.

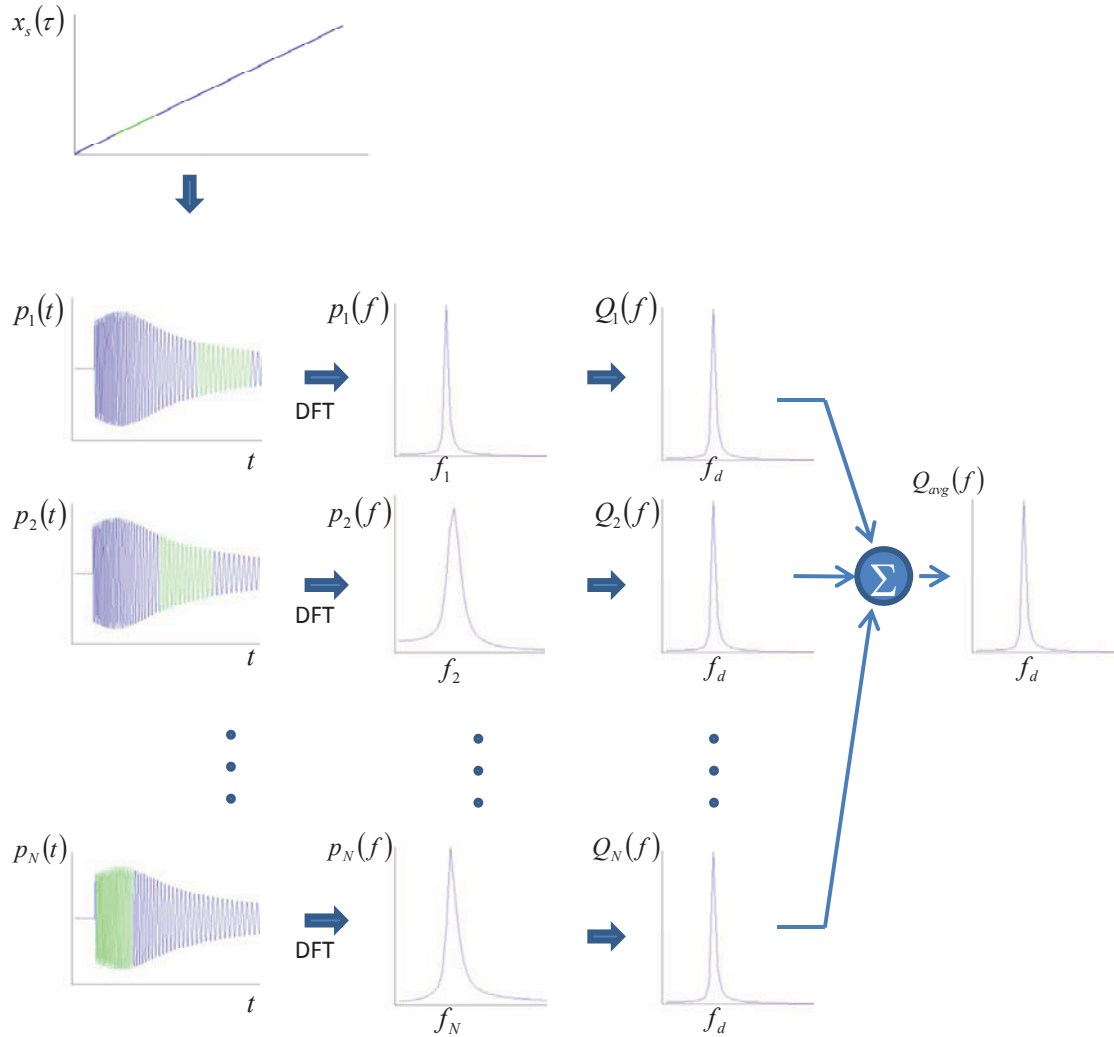


Figure 5.18: Schematic of the data processing of the new method.

The code allows selecting the number of emission time windows used in the computation, the number of data points in each emission time window, and the overlap between consecutive emission time windows.

The parameters that were compared for the time domain and the frequency domain methods are: a) Processing time and b) Spot-size. The processing time is the time required to complete the computation of each data set for similar processing parameters, i.e. number of time windows, window length, overlap between consecutive time windows, and number of grid points. The spot-size is the width of the main-lobe 3 dB down the peak, and it is a measure of the

resolution of the acoustic maps. The spot-size is also a function of the array dimensions; however, by using the same array for all simulations, this dependence of the spot-size on the array aperture was ruled out.

5.3.3 Linear Motion

For this type of source motion, the selection of the source-to-array distance, and source speed was based on airplane flyover measurements since these types of measurements are among the most common applications of phased array technology to locate moving sound sources. For comparison purposes, a few data sets were also processed using the currently available time domain beamforming algorithm. Figure 5.19 shows the acoustic maps for a monopole source emitting sound at 1000 Hz, moving along the x-direction with a constant velocity of 50 m/s, and flying over the microphone array at an altitude, i.e. array-to-source distance, of 30 meters. Figure 5.19a is the acoustic map obtained using the time domain beamforming algorithm for source strength estimation, whereas Figure 5.19b is the acoustic map obtained using the new frequency domain beamforming algorithm, also for source strength estimation. Both maps were processed using a scanning grid resolution of 0.1-meters. From this figure it can be seen that in terms of source location, both methods yield the location of the source at the (0,0) position. It also shows that the array resolution is slightly degraded in the new frequency domain approach.

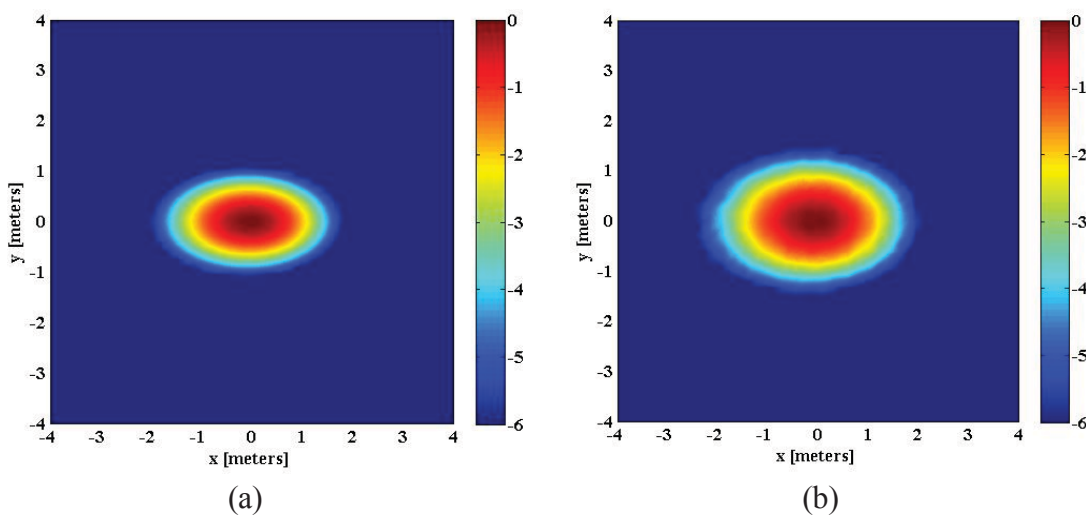


Figure 5.19: Acoustic maps of a monopole source radiating sound at 1000 Hz, moving in the x-direction at 50 m/s obtained with a) Time Domain beamforming, and b) Frequency domain beamforming for source strength estimation.

5.3.4 Rotary Motion

Sources moving along a circular trajectory, i.e. rotating sources, are found in several applications such as wind turbines, fans, propellers and jet engines. For this type of source motion, a monopole source rotating around the z -axis in the $z = 0$ plane was simulated.

Figure 5.20 shows the acoustic maps for a monopole source emitting sound in the form of a pure-tone at 2500 Hz, rotating at 600 rpm around the z -axis along a circular trajectory (shown with a gray dotted line) with a 1-meter radius. This rotational speed and radius correspond to a tip speed of 62.8 m/s (Mach 0.18). For comparison purposes, these maps were obtained using the time domain beamforming method and the new frequency domain beamforming method using the formulation developed in Section 4.5 for rotating source of sound. The scanning grid used to process the results with both methods consisted of 441 points with a grid spacing of 0.05 meters. The 35-microphone phased array was located on a plane parallel to the plane of rotation at a distance of 5 meters. Furthermore, the origin of the array was placed along the axis of rotation of the source. From this figure, it can be seen that both methods locate the source at the same position. However, for this particular case of source motion, the traditional time domain method yielded a higher resolution, i.e. smaller spot-size

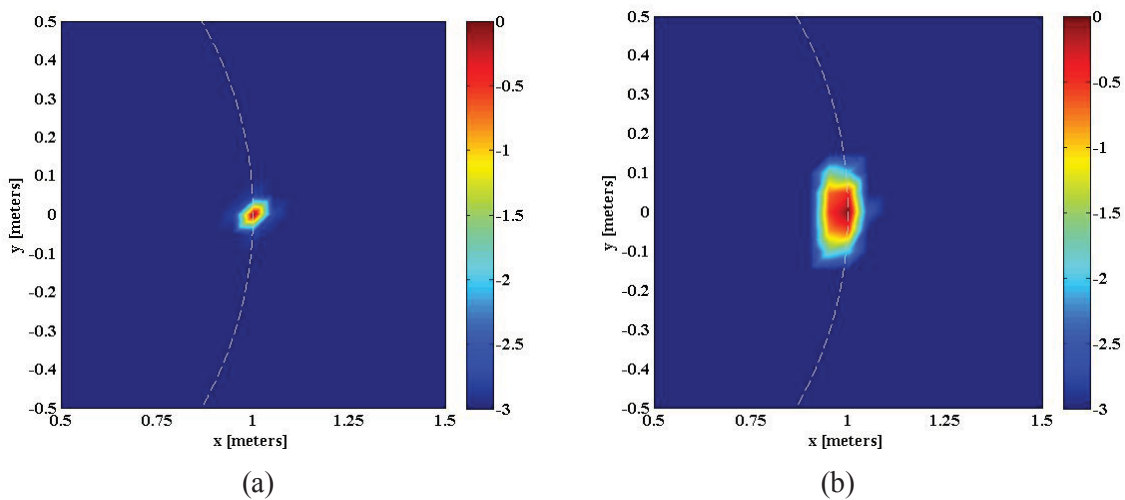


Figure 5.20: Acoustic maps of a monopole source radiating sound at 2500 Hz, rotating around the z -axis in the $z=0$ plane at 600 rpm, obtained with a) Time domain beamforming, and b) Frequency domain beamforming.

5.4 Parametric Studies

In the previous section it was shown that the new frequency domain beamforming method works with a single source under ideal conditions. In this section, the performance of the new frequency domain beamforming method is studied for less ideal conditions such as the contamination of the microphone signals with uncorrelated noise, or the presence of multiple correlated and uncorrelated noise sources. This section also studies the performance of the new frequency domain beamforming approach for various parameters, including the source velocity, resolution of the acoustic maps, and computational efficiency. For comparison purposes, a few selected cases were also processed using the traditional time domain beamforming method.

5.4.1 Source Velocity

The first parameter studied during the validation of the new frequency domain beamforming approach was the effect of the source velocity in the beamforming output. To this end, a monopole source emitting a pure tone at 1000 Hz moving along the x-direction with velocities varying between 50 m/s and 300 m/s in increments of 50 m/s was simulated. Note that the case of the source moving at 300 m/s is a very high subsonic case that is not common in most practical applications.

Figure 5.21 shows the emission angle range used to process the data for the source moving at various velocities. That is, data corresponding to the source located within 78° (at approach) and 102° (at recede) were used to compute the beamforming output. For the observer-to-source trajectory distance of 30 meters used for these simulations, the range of 78° to 102° corresponds to a source displacement of 12.75 meters.

The emission angle range used to process the data was selected based on previously conducted flight tests. In 2002, Piet et al.[11] conducted a flyover test of an Airbus A340 aircraft. In that test, the acoustic maps were computed using time frames of 0.5 seconds in which the emission angle varied around 15° to 20° . Therefore, with this angle variation, the acoustic maps were computed using the microphone signals sampled when the aircraft was between 80° (at

approach) and 100° (at recede). Using data outside this range increases the uncertainty in the source position due to the parallax effect. More recently, in 2005 Brusniak et al. [26] conducted a flight test of a Boeing 777-300ER using 5 nested phased arrays. In this particular test, the acoustic maps were obtained using data when the aircraft was between approximately 82° (at approach) and 98° at recede.

For the four different source velocities simulated to validate the new frequency domain beamforming method, the microphone data used to process the beamforming output was divided into time windows of 512 samples each, with no overlap between consecutive windows. The 512 samples correspond to 0.02 seconds for the 25600 Hz sampling frequency used. As the source velocity increases, the number of data points sampled by the microphones within the emission angle range decreases. Therefore, the faster the source moves the less time windows available for processing.

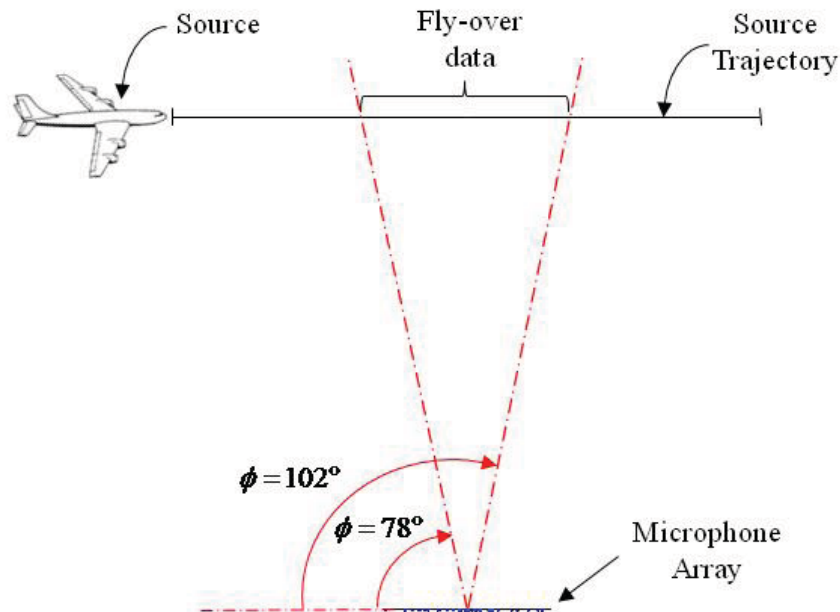


Figure 5.21: Emission angle range for data processing of a monopole source moving at various velocities.

Figure 5.22 shows the acoustic maps obtained for the a monopole source moving with velocities between 50 m/s and 300 m/s with a 6 dB cutoff. From this figure it can be seen that

there is not a significant effect of the source velocity on the acoustic maps within this dynamic range. However, increasing the dynamic range to 10 dB, as shown in Figure 5.23, reveals the presence of side-lobes in the acoustic maps. As the velocity of the source increases, the number of side-lobes on the acoustic maps also increases.

The presence of side-lobes on the acoustic maps shown in Figure 5.23 was suspected to be the result of less time windows used in the computation of the average source strength signal. Therefore, the datasets corresponding to the source moving at 250 m/s and 300 m/s were reprocessed using 50% overlap between consecutive time windows. The use of this overlap doubled the number of time windows used for the computation of the beamforming output. Figure 5.24 shows the acoustic maps for the monopole source moving at 250 m/s and 300 m/s processed using time windows of 512 data points with 50% overlap. From this figure it can be seen that using more time windows for the computation of the beamforming output reduced the amount of side-lobes.

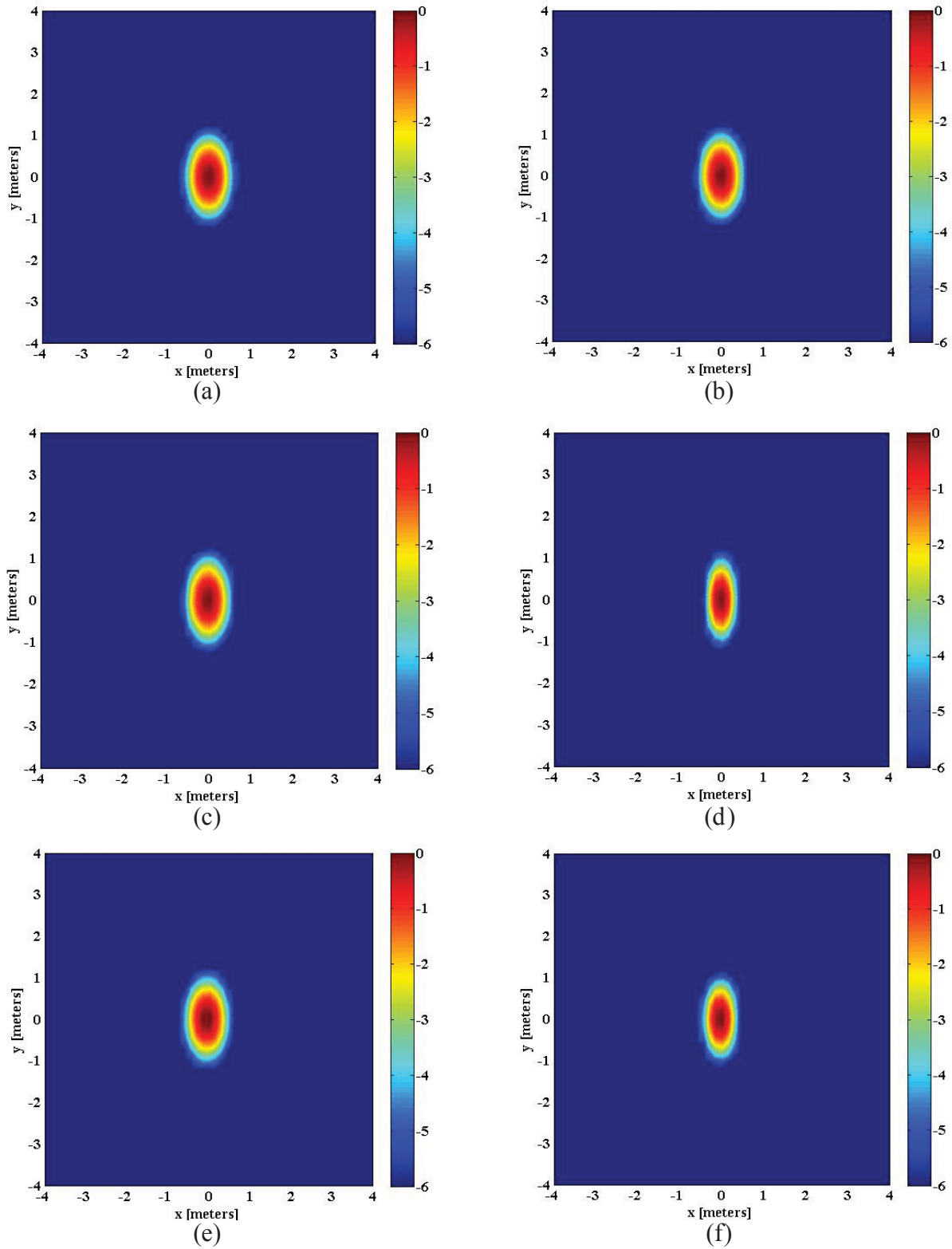


Figure 5.22: Acoustic maps for a monopole source emitting sound at 1000 Hz moving along the x-direction with velocities of: a) 50 m/s, b) 100 m/s, c) 150 m/s, d) 200 m/s, e) 250 m/s, and f) 300 m/s. All maps were processed using constant time windows of 0.02 sec. (6 dB cutoff).

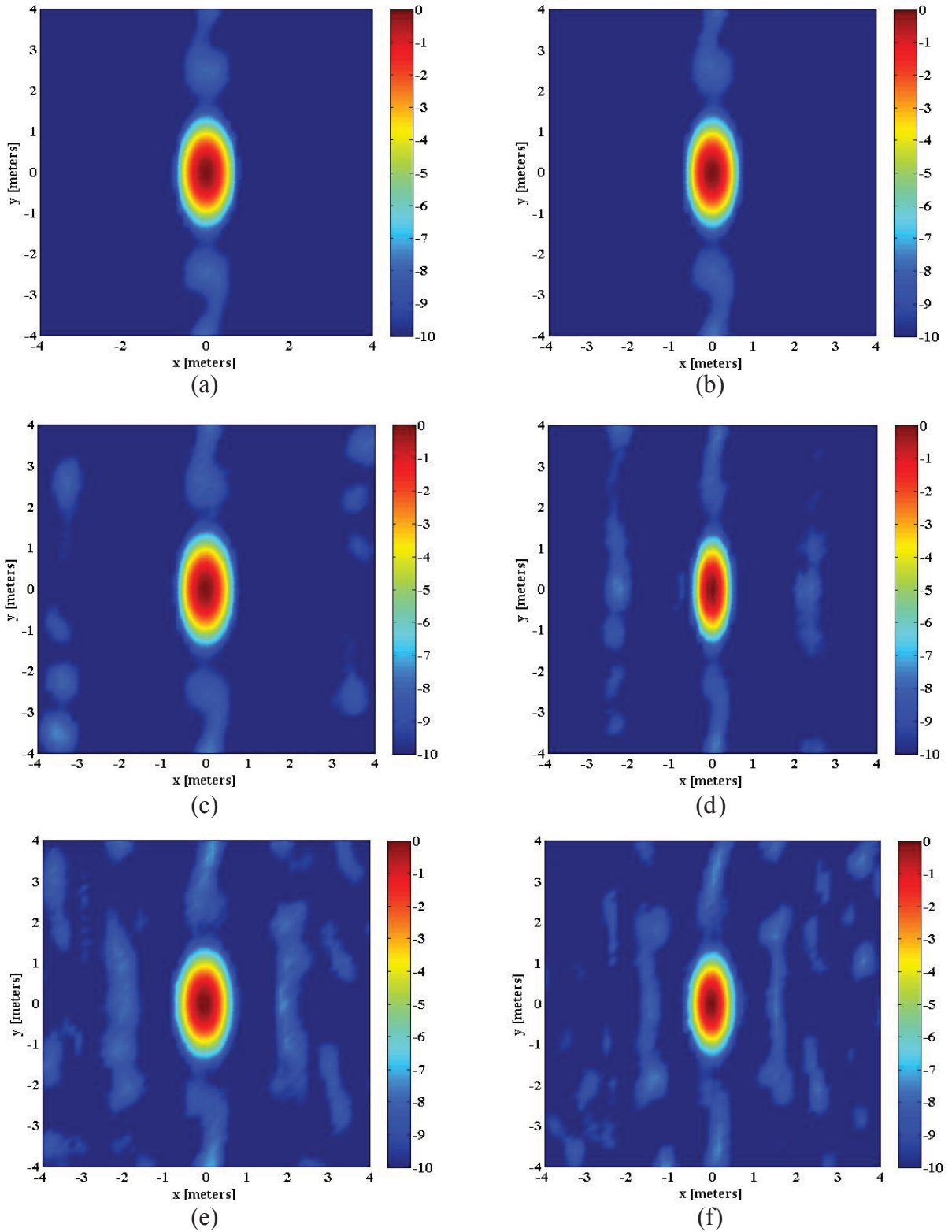


Figure 5.23: Acoustic maps for a monopole source emitting sound at 1000 Hz moving along the x-direction with velocities of: a) 50 m/s, b) 100 m/s, c) 150 m/s, d) 200 m/s, e) 250 m/s, and f) 300 m/s. All maps were processed using constant time windows of 0.02 sec with no overlap. (10 dB cutoff).

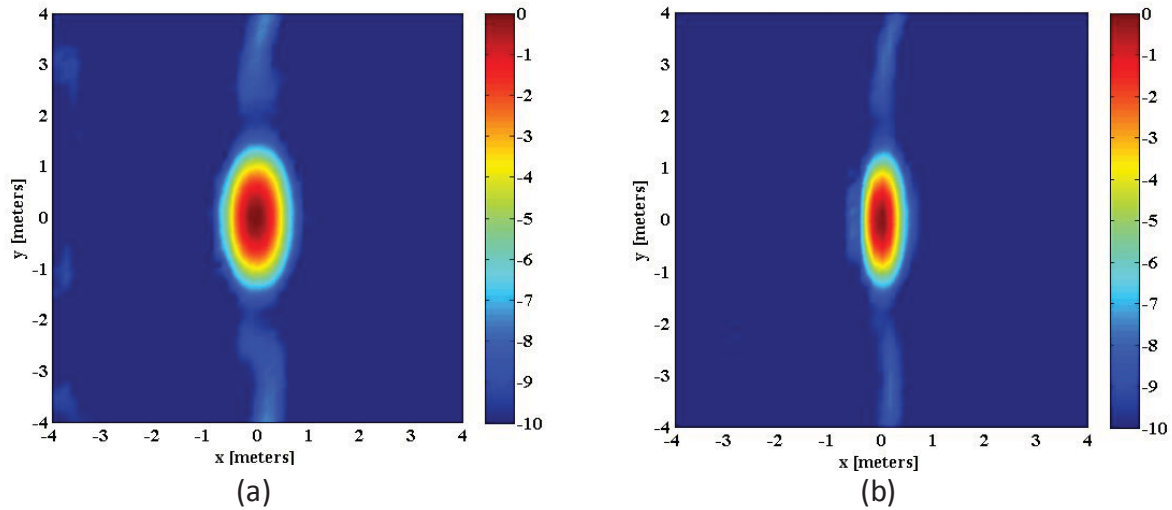


Figure 5.24: Acoustic maps for a monopole source emitting sound at 1000 Hz moving along the x-direction with velocities of: a) 250 m/s, and b) 300 m/s. Both maps were processed using constant time windows of 0.02 sec with 50% overlap. (10 dB cutoff).

5.4.2 Resolution of the Acoustic Maps

The resolution of the acoustic maps is related to the emission frequency of the source and is measured by the beamwidth also known as the spot-size. The beamwidth is the width of the main-lobe 3 dB down the peak. To study the performance of the new frequency domain method for various source emission frequencies, a monopole source moving along the x-direction at 50 m/s and emitting sound at frequencies varying between 1000 Hz and 4000 Hz was simulated. Both, the source position signal and the microphone signals for these simulations were sampled simultaneously at 25600 Hz.

Figure 5.25 shows the acoustic maps obtained for the source emitting sound at four different frequencies. Again, these maps were processed using the microphone signals corresponding to the source being located between the emission angles of 78° (at approach) and 102° (at recede). These data were broken down into short time windows of 0.02 seconds each. The first column of Figure 5.25 shows the acoustic maps in the plane of motion, while the figures in the center column and the left column show the amplitude of the acoustic maps along the direction of motion and along the transverse direction, respectively. From these figures, it can

be seen that beamwidth in the direction of motion is slightly smaller than the beamwidth in the transverse direction. Using the beamwidth of these acoustic maps in the direction of motion at the various frequencies allowed plotting the curve shown in Figure 5.26 which allows predicting the beamwidth at any frequency inside the studied range. Note that this exponential reduction of the beamwidth as frequency is increased follows the same pattern as the beamwidth obtained with conventional frequency domain beamforming and time domain beamforming, where the beamwidth is proportional to the product of the wavelength and the source-to-array distance [11].

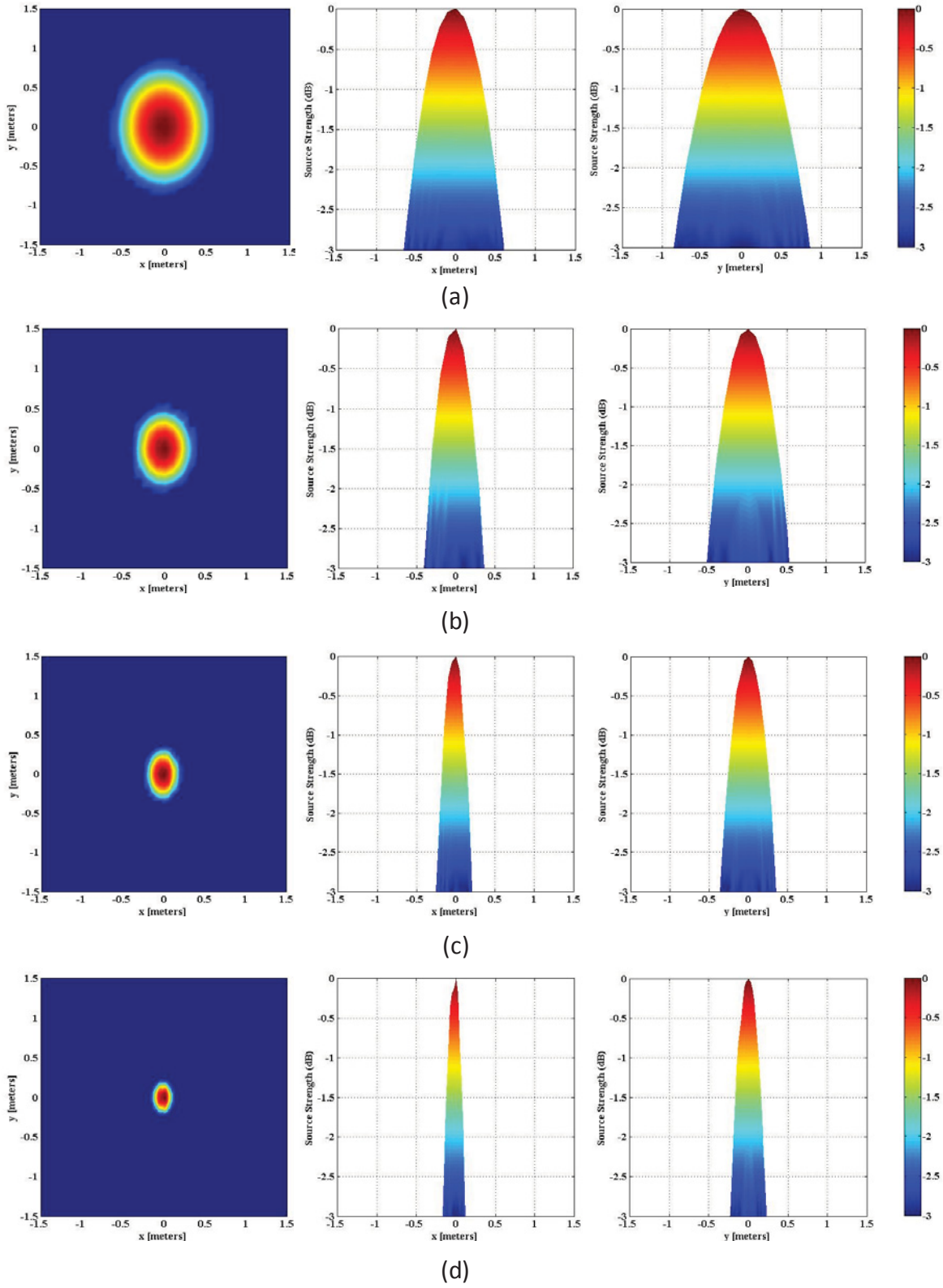


Figure 5.25: Acoustic maps for a monopole source moving along the x-direction at 50 m/s emitting sound at: a) 1000 Hz, b) 1600 Hz, c) 2500 Hz, and b) 4000 Hz.

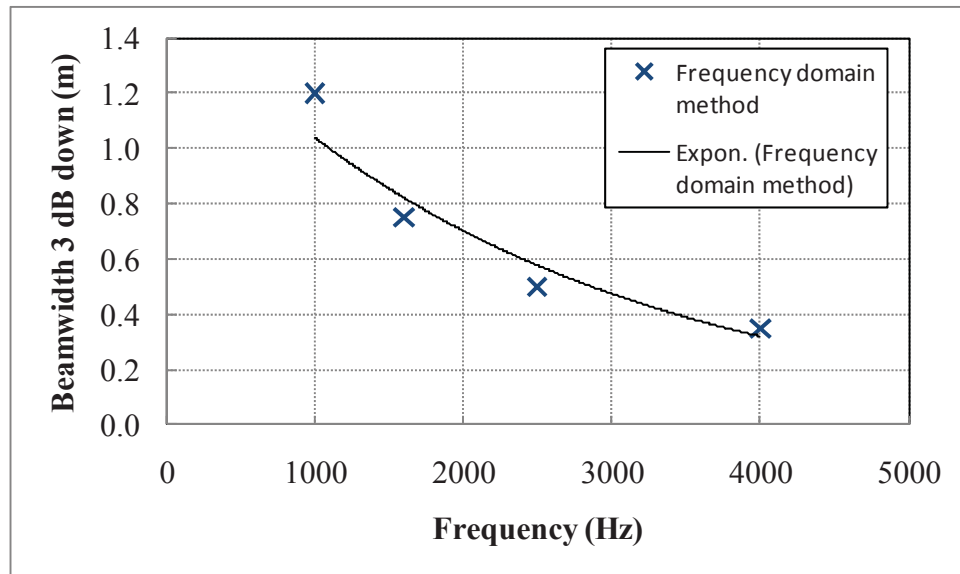


Figure 5.26: Beamwidth of the acoustic maps of a monopole source with linear motion emitting sound at various frequencies obtained using the new frequency domain beamforming method.

5.4.3 Emission Angle

To study the effect of the emission angle on the beamforming output, consider the source shown in Figure 5.27. This source moves along the x-direction at a constant speed of 50 m/s from position (0,0,0) to position (100,0,0), and radiates sound in the form of a pure tone at 1000 Hz. The source trajectory is divided into 50 segments of equal length (2 meters). Segments 1 through 20 correspond to the source approaching the array. Segment 25 corresponds to the source passing over the array (fly-over), and segments 30 to 50 correspond to the source moving away from the array. The acoustic maps for each of the segments shown in Figure 5.27 (in blue circles) are presented in Figure 5.28.

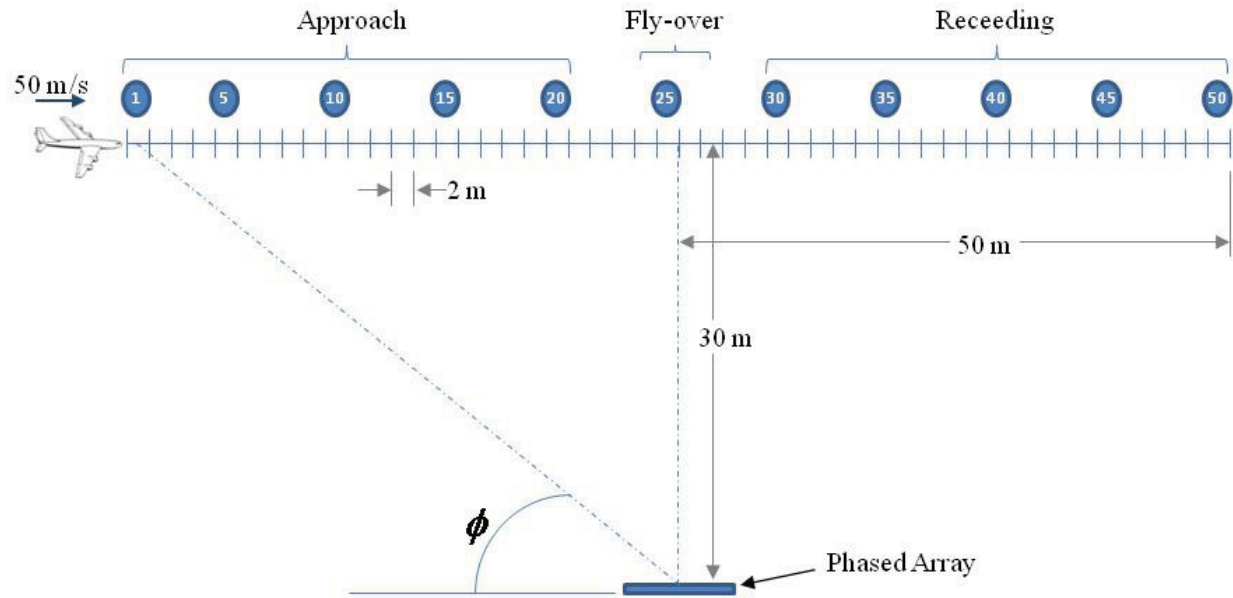


Figure 5.27: Source position segments for various emission angles ϕ .

From Figure 5.28 it can be seen that the acoustic maps obtained as the source approaches the array are not symmetric with the acoustic maps obtained while the source moves away from the array. For example, the acoustic map for the source approaching the array at $\phi = 55^\circ$ (Figure 5.28d) shows a smaller and rounder “hot-spot” as compared to the map for the source moving away from the array at $\phi = 122.2^\circ$ (Figure 5.28h). This difference in the shape of the acoustic maps for similar emission angles of approach and recede is the result of the change in the received frequency. That is, when the source approaches the array, the received (perceived) frequency is higher than the actual emission frequency and therefore the acoustic maps have a higher resolution (smaller “hot-spot”). However, when the source moves away from the array, the received (perceived) frequency is lower than the actual emission frequency and therefore the acoustic maps have a lower resolution (larger “hot-spot”). This phenomenon was also observed by Piet et al.[10] while conducting phased array measurements of an Airbus A340 airplane during flight tests.

From the acoustic maps shown in Figure 5.28, it can be seen that for this particular configuration and microphone array pattern, the beamforming output yields acceptable results in the range of 45° for approach and 120° for recede.

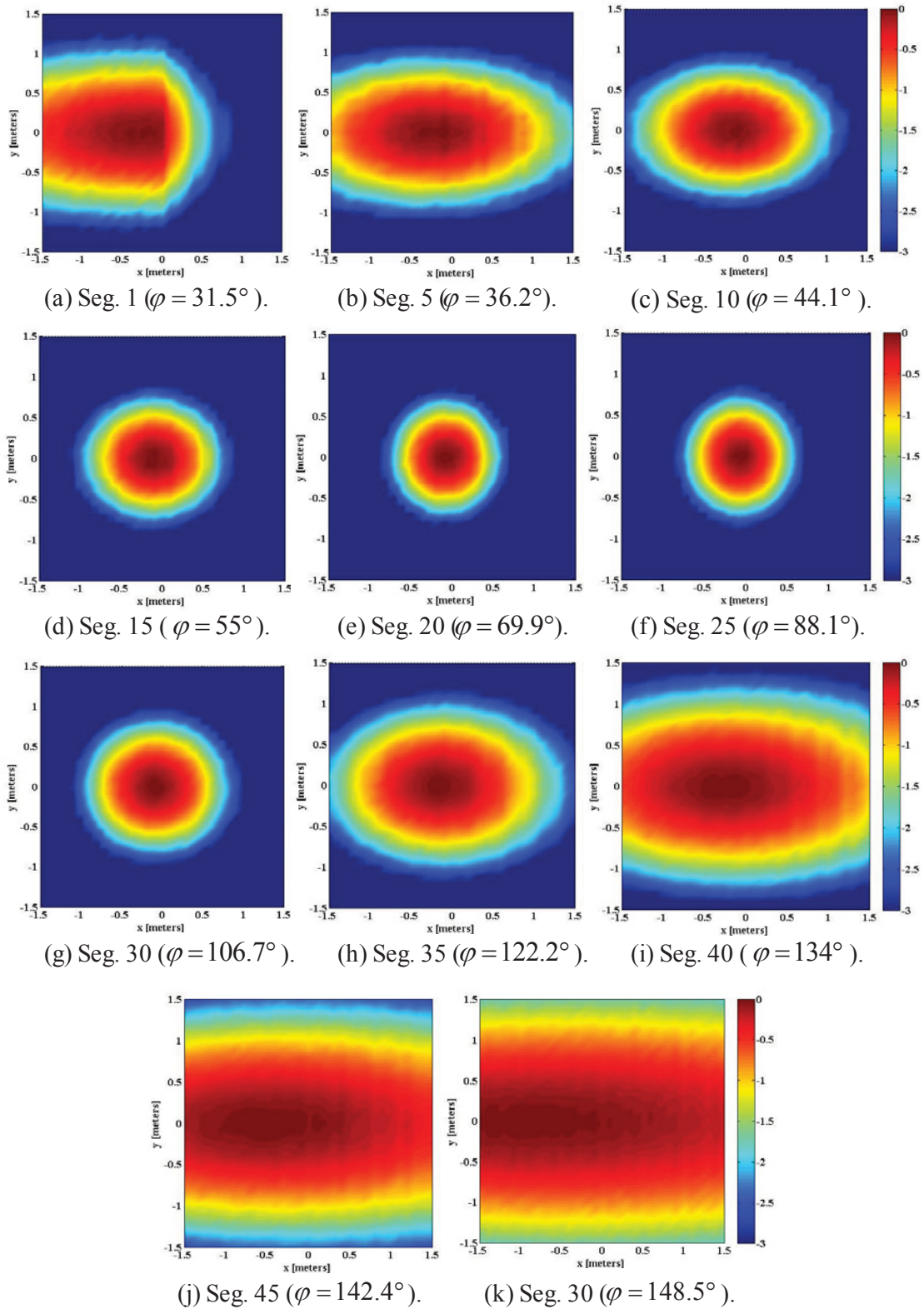


Figure 5.28: Acoustic maps showing the spot-size (3 dB down from the main-lobe peak) for the various source position segments shown in Figure 5.27.

5.4.4 Uncorrelated Noise in the Microphone signals

In most aerodynamic applications, the presence of wind or airflow over the microphones of the array causes uncorrelated broadband noise in the microphone signals. Therefore, as part of the numerical validation of the new frequency domain beamforming method, this section presents the results for the case where the microphone signals are contaminated by uncorrelated noise. To this end, three cases were studied where the microphone signals contained noise with signal-to-noise ratios of 6 dB, 3 dB, and 0 dB. For these three cases a monopole source moving along the x-direction at 50 m/s and emitting sound in the form of a pure tone at 1000 Hz was simulated. An array-to-source distance of 30 meters, and a scanning grid of 0.1 meters spacing were used for all three cases.

Figure 5.29 shows the acoustic maps obtained for the three simulated cases with different signal-to-noise ratios on the microphone signals. This figure also shows the amplitude spectrum corresponding to the signal of the first microphone of the array. From this figure it can be seen that the beamforming output of the new frequency domain beamforming method performs well for signals with 3 dB and 6 dB signal-to-noise ratio, however it starts deteriorating for signals with 0 dB signal-to-noise ratio.

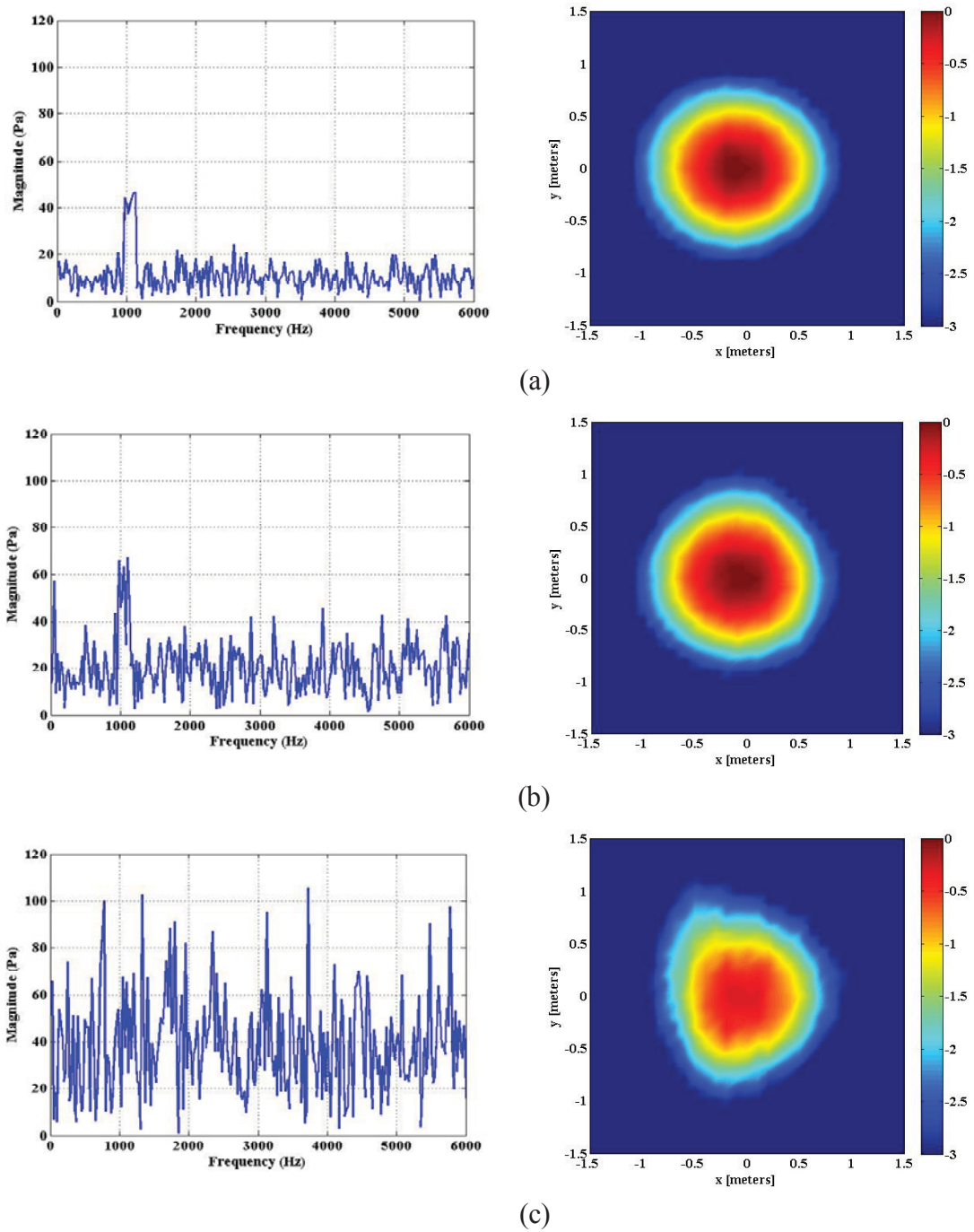


Figure 5.29: Fourier Transform of the first microphone of the array, and the corresponding acoustic map showing the effect of uncorrelated noise in the array microphones for various levels of noise.

5.4.5 Multiple Sources of Sound

Up to this point, the analysis has focused on a single moving monopole source. However, in many practical applications, there is more than one dominant source present. Therefore, this section presents the results of numerical simulations for two and three moving monopole sources of sound.

Figure 5.30 shows the acoustic maps of two monopole sources moving along the x -direction with a constant velocity of 100 m/s. Figure 5.30a corresponds to two monopole sources emitting sound at the same frequency of 1000 Hz, i.e. correlated sources; whereas Figure 5.30b is the acoustic map for one source emitting sound at 1000 Hz located at $(3,-3,0)$ and a second source emitting sound at 1100 Hz located at $(3,3,0)$, i.e. uncorrelated sources of sound.

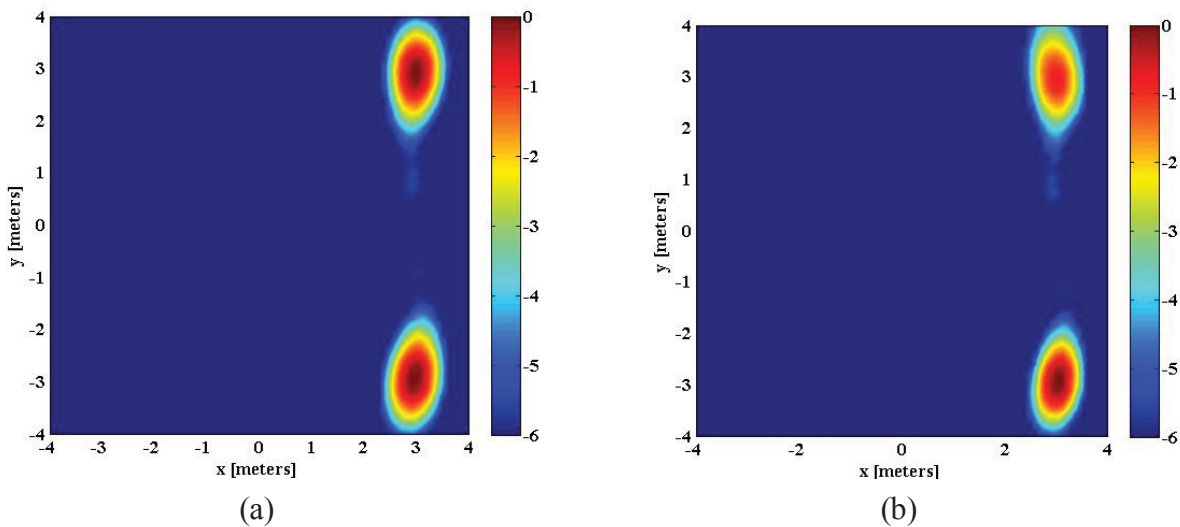


Figure 5.30: Acoustic maps for two monopole sources: a) Correlated sources emitting sound at 1000 Hz located at $(3,3,0)$ and $(3,-3,0)$, and b) Uncorrelated sources emitting sound at 1000 Hz $(3,3,0)$ and at 1100 Hz $(3,-3,0)$.

Figure 5.31 shows the acoustic maps for the case of three monopole sources moving along the x -direction with a constant velocity of 100 m/s. Figure 5.31a corresponds to the three sources emitting sound at the same frequency of 1000 Hz, i.e. correlated sources; whereas Figure 5.31b is the acoustic map for three uncorrelated sources: one source emitting sound at 1000 Hz

located at $(-1,0,0)$, a second source emitting sound at 1050 Hz located at $(3,3,0)$, and a third source emitting sound at 1100 Hz located at $(3,-3,0)$.

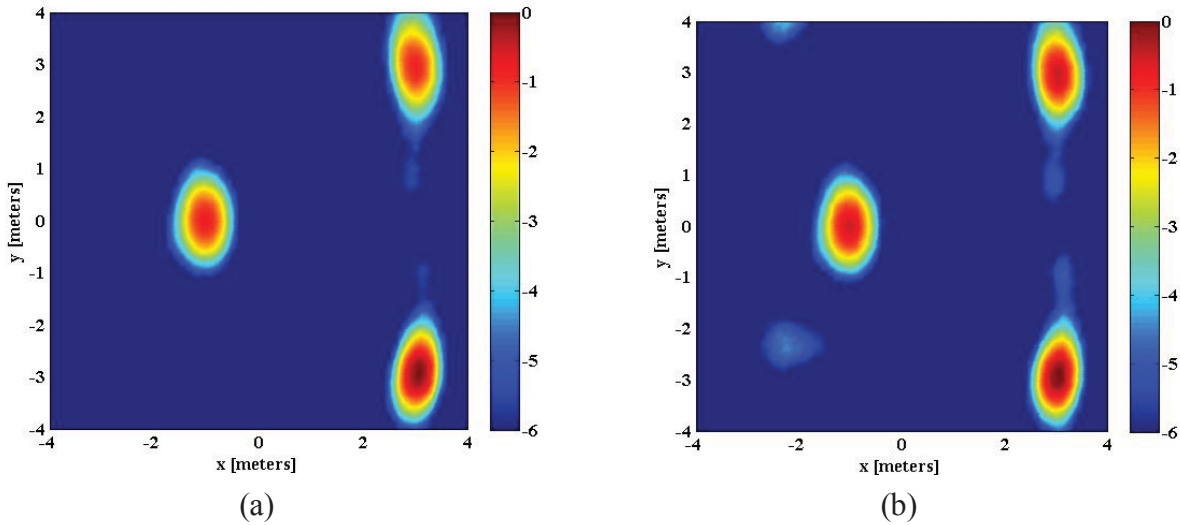


Figure 5.31: Acoustic maps for three monopole sources: a) Correlated sources emitting sound at 1000 Hz located at $(-1,0,0)$, $(3,3,0)$ and $(3,-3,0)$, and b) Uncorrelated sources emitting sound at 1000 Hz $(-1,0,0)$, 1050 Hz $(3,3,0)$, and at 1100 Hz $(3,-3,0)$.

From Figure 5.30 and Figure 5.31 it can be seen that the new frequency domain beamforming method localizes all sources at the correct position. It can also be seen that increasing the number of sources resulted in the appearance of more side-lobes. In this respect, as it was shown in section 5.4.1, one approach to reduce the side-lobes is to increase the number of averages in the computation of the beamforming output.

5.4.6 Processing Speed

As explained in Chapter 4, the new frequency domain beamforming method performs all the computations in the frequency domain. As a result, this method yields a more accurate relative phase between the microphones of the array as compared to traditional time domain beamforming. Furthermore, the new method does not need to perform any type of data interpolation as it is the case with time domain beamforming which requires interpolation of every data point of every microphone signal for every grid point of the scanning grid.

Both time domain and frequency domain beamforming methods for moving sources of sound perform the computations on a per microphone basis for every grid point of the scanning grid. Therefore, the processing time required to complete the computation of the beamforming output over a given scanning grid is a function of the product of the number of microphones in the array and the number of grid points in the scanning grid.

For comparison purposes, selected datasets used in the validation of the new frequency domain beamforming method were also processed using traditional time domain beamforming. For all cases, an emission time window of 0.4 seconds was used. The processing time required to complete the computation of these selected datasets using the time domain beamforming method and the new frequency domain beamforming method are presented in Figure 5.32.

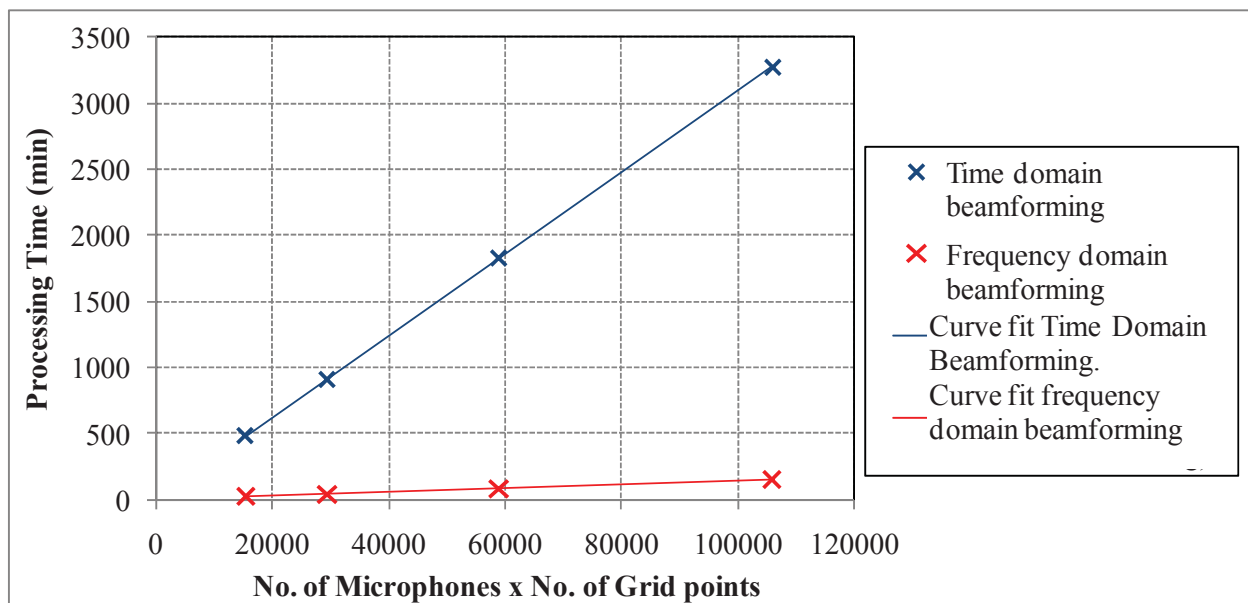


Figure 5.32: Processing time required to complete the computation of the beamforming output over a given scanning grid using the traditional time domain beamforming method and the new frequency domain beamforming method. For all the cases, a time window of 0.4 seconds was used.

Figure 5.32 clearly shows the benefits of the new frequency domain beamforming method in terms of computational efficiency. From this figure, it can be seen that as the product of grid points and microphones increases, the processing time for the time domain beamforming

increases at a rate 20 times the rate of increase of the new frequency domain beamforming method.

In actual fly-over measurements such as the flight test conducted by Boeing in 2005 [26], phased arrays with over 600 microphones are used, and the scanning grid which usually covers the entire aircraft can have hundreds of thousands of grid points. For these situations, the benefit of the new frequency domain beamforming method in terms of computational efficiency is even greater than in the simulations used in the present work.

5.5 Remarks from the Numerical Validation

From the results obtained for the various numerical simulations, it is clear that the most important strength of the new frequency domain beamforming method is its improved computational efficiency over the traditional time domain beamforming method. This difference in computational efficiency was assessed by direct comparison of the processing time used by each method to process the same data set. The results show that as the number of microphones and/or grid points increase, the processing time for the traditional time domain beamforming increases at a rate 20 times larger than the rate of increase of the new frequency domain beamforming. The implications of this difference in processing times is even more significant for actual situations where large microphone count and large scanning grids are used.

The new frequency domain beamforming method is faster than the time domain beamforming method because it does not require interpolation of the microphone time signals for every grid point analyzed. However, the new method still requires the computation of the Fourier transform of the source strength signal for every point of the scanning grid.

With respect to the emission angle, it was found that within the range of 45° for approach and 120° for recede, the acoustic maps obtained are consistent in shape. Outside this range, the acoustic maps become largely distorted.

In terms of the effect of the source velocity on the beamforming output, the results of simulated monopole sources at various velocities were studied. These results showed that the effect of source velocity is related to the amount of data available for processing. The higher the source velocity, the less data available for processing the result. This reduction of available data for sources with high velocity results in acoustic maps with an increased number of side-lobes, thus reducing the dynamic range of the maps. One way to approach this problem is by using overlap between consecutive time windows. As a consequence, the number of averages for the computation of the estimated source strength was increased, and the statistical error was reduced.

Another parameter considered during the validation of the new frequency domain beamforming method is the effect of uncorrelated noise in the microphone signals. This problem is frequently present in the case of aeroacoustic measurements where airflow over the microphones contaminates the recorded signals. In this context, it was found that the new beamforming method can localize sources with zero signal-to-noise ratios.

Regarding the performance of the new frequency domain beamforming method for the case where multiple sources are present, simulations with two and three correlated and uncorrelated noise sources were performed. From the acoustic maps of these simulations it was found that the new frequency domain beamforming method was able to localize the sources in the correct position. Furthermore, the maps for the correlated sources showed less side-lobes than the maps for the uncorrelated sources.

Chapter 6

Conclusions and Future Work

6.1 Conclusions

A new de-Dopplerization technique to remove the Doppler effect from acoustic signals of moving sources of sound was developed. The approach used for this technique consists in breaking down the motion of the source in short time periods. Then, the Short-Time Fourier Transform (STFT) is used to transform the acoustic time signals into the frequency domain. For each time period, the original (undistorted) source strength signal is estimated. The Doppler effect is accounted for using the translation and rescaling properties of the Fourier Transform. Therefore, the de-Dopplerization of the signal is performed entirely in the frequency domain.

The de-Dopplerization technique was then implemented into a frequency domain beamforming algorithm to locate sources of sound from moving objects. The approach used for this implementation consisted of attaching a grid of potential source locations, i.e. scanning grid, to the moving object. At each point of the grid, a potential source was assumed. Then, for each point of the grid, the acoustic signals were de-Dopplerized and the strength of the assumed source was estimated. The mathematical formulation for the implementation of the de-Dopplerization technique into the beamforming algorithm is presented for two different types of source motion: sources moving along a linear trajectory, and sources moving along a circular trajectory.

The validation of the new de-Dopplerization technique and its implementation into a beamforming algorithm was performed using numerical simulations. These numerical simulations consisted of two parts. First, a data set was generated for various source configurations such as emission frequency, source type, and source velocity. Then, these data

sets were processed using the new frequency domain beamforming algorithm implemented into a computer code. A few selected data sets were also processed using the currently available time domain beamforming algorithm for comparison purposes.

The results obtained from the numerical simulations in terms of computational efficiency show that the new frequency domain beamforming method is approximately 10 times faster than the currently available time domain beamforming. This improvement in computational efficiency from time domain to frequency domain beamforming is the result of eliminating the need for resampling and interpolation of the acoustic signals

The new frequency domain beamforming method was also tested for several source velocities varying from 0 m/s to 300 m/s. At all velocities, the new method was able to locate the simulated source.

6.2 Future Work

The work presented in this dissertation provides the analytical formulation of a new frequency domain beamforming method to locate moving sources of sound, which was validated using numerical simulations. Therefore, the next step is to validate the method using experimental data. For example, this could be done using airplane flyover measurements or wind turbine noise measurements.

In many aeroacoustic applications, airflow plays an important role. Therefore, another area for future work regarding the experimental validation of the new frequency domain beamforming method is the implementation of a convective amplification factor to account for this effect. Airflow also produces uncorrelated noise in the microphone signals. The approach that is used for this type of situation is to remove the diagonal elements of the cross-spectral matrix. Thus, future efforts to validate the new method experimentally should also focus in implementing the diagonal removal technique.

Another parameter to be considered for future work is related to the effect of the microphone array characteristics on the performance of the new frequency domain beamforming method. The array dimension, microphone number and microphone distribution have an important role in determining the resolution and side-lobe level of the acoustic maps, Therefore, a study could be conducted to investigate if there are particular array designs that in combination with the new frequency domain beamforming method will improve the beamforming output.

In terms of improving the accuracy of the de-Dopplerization technique presented in this dissertation, future work should focus on investigating the possibility of using higher order or more complex approximations of the emission/reception time relation to reduce variations, and still be able to use Fourier transform properties to estimate the de-Dopplerized source signal.

References

- [1] Verhas, H.P., “A Restoration Procedure for (Non-Stationary) Signals from Moving Sources”, *Journal of Sound and Vibration*, 89(4), pp. 487-497, 1983.
- [2] Howell, G.P., Bradley, A.J., McCormick, M.A., and Brown, J.D., “De-Dopplerization and Acoustic Imaging of Aircraft Fly-Over Noise Measurements”, *Journal of Sound and Vibration* 105(1), pp. 151-167, 1986.
- [3] Bariskow, B., and King III, W.F., “On Removing the Doppler Frequency Shift from Array Measurements of Railway Noise”, *Journal of Sound and Vibration* 120(1), pp. 190-196, 1988.
- [4] Jonhson, DH, and Dudgeon, DE, *Array Signal Processing: Concepts and Techniques*, Prentice Hall, New Jersey, 1993.
- [5] Bariskow, B., “Experiences with Various Configurations of Microphone Arrays Used to Locate Sound Sources on Railway Trains Operated by the DBAG”, *Journal of Sound and Vibration* 193(1), pp. 283-293, 1996.
- [6] Dougherty, RP, “Spiral-Shaped Array for Broadband Imaging”, U.S. Patent No.5,838,284.
- [7] Underbrink, JR, and Dougherty, RP, “Array Design for Non-Intrusive Measurements of Noise Sources”, *Proceedings of NoiseCon 1996*, Seattle, WA., 1996.
- [8] Thomas Mueller (ed.), *Aeroacoustic Measurements*, Springer, 2002. ISBN 3-540-41757-5.
- [9] Michel, U., Bariskow, B., Helbig, J., Hellmig, M., and Schuttpelz, M., ”Flyover Noise Measurements on Landing Aircraft with a Microphone Array”, *AIAA Paper*, AIAA 1998-2336, 1998.

- [10] Piet, J.F., Elias, G., and Lebigot, P., “Localization of Acoustic Sources from a Landing Aircraft with a Microphone Array”, AIAA Paper, AIAA 1999-1811, 1999.
- [11] Piet, J.F., Michel, U., and Bohning, P., “Localization of the Acoustic Sources of the A340 with a Large Phased Microphone Array During Flight Tests”, AIAA Paper, AIAA 2002-2506, 2002.
- [12] Sijtsma, P., and Holthusen, H., “Source Location by Phased Array Measurements in Closed Wind Tunnel Test Sections”, AIAA/CEAS Aeroacoustics Conference and Exhibit, 5th Bellevue, WA, May 10-12, 1999, Collection of Technical Papers. Vol. 1(A99-27801 06-71).
- [13] Stoker, R.W., Guo, Y., Streett, C., and Burnside, N., “Airframe Noise Source Locations of a 777 Aircraft in Flight and Comparisons with Past Model Scale tests”, AIAA Paper, AIAA 2003-3232, 2003.
- [14] Ravetta, P.A., Burdisso, R.A., and Ng, W., “Wind Tunnel Aeroacoustic Measurements of a 26%-scale 777 Main Landing Gear”, 10th AIAA/CEAS Aeroacoustics Conference, Manchester, Great Britain, May 10-12, 2004, AIAA-2004-2885.
- [15] Oerlemans S., and Sijtsma, P., “Acoustic Array Measurements of a 1:10.6 Scaled Airbus A340 Model”, 10th AIAA/CEAS Aeroacoustics Conference and Exhibit, Manchester, United Kingdom, May 10-12, 2004, AIAA-2004-2924.
- [16] Remillieux, M., Camargo, H.E., Burdisso, R.A., and Ng, W., “Aeroacoustic Study of a 26%-Scale , High-Fidelity, Boeing 777 Main Landing Gear in a Semi-Anechoic-Wind-Tunnel Test Section”, 13th AIAA/CEAS Aeroacoustics Conference, Rome, Italy, May 21-23, 2007, AIAA-2007-3453.
- [17] Hutcheson, F.V., and Brooks, T.F., “Measurements of Trailing Edge Noise using Directional Array and Coherent Output Power Methods”, 8th AIAA/CEAS Aeroacoustics Conference and Exhibit, Breckenridge, CO, June 17-19 2002, AIAA-2002-2472.

- [18] Oerlemans, S., and Migliore, P., "Aeroacoustic Wind Tunnel Tests of Wind Turbine Airfoils", 10th AIAA/CEAS Aeroacoustics Conference, Manchester, United Kingdom, May 10-12, 2004, AIAA-2004-3042.
- [19] Oerlemans, S., "Wind Tunnel Aeroacoustic Tests of Six Airfoils for Use on Small Wind Turbines", NREL Report SR-500-34470, April 2004.
- [20] Sijtsma, P., Oerlemans, S., and Holthusen, H., "Location of Rotating Sources by Phased Array Measurements", AIAA Paper, AIAA 2001-2167, 2001.
- [21] Oerlemans, S., and Mendez Lopez, B., "Acoustic Array Measurements on a Full Scale Wind Turbine", AIAA Paper, AIAA 2005-2963, 2005.
- [22] Oerlemans, S., Sijtsma, P., and Lopez Mendez, B., "Location and Quantification of Noise Sources on a Wind Turbine", *Journal of Sound and Vibration* 299, pp. 869-883, 2006.
- [23] Dowling A.P. and Ffowcs Williams J.E., "Sound and Sources of Sound," Ellis Horwood Series in Engineering Science, 1983.
- [24] Pierce, AD, *Acoustics, An Introduction to its Physical Principles and Applications*, Acoustical Society of America, 1989.
- [25] Spanier, J. and Oldham, K. B. "The Dirac Delta Function $\delta(x-a)$." Ch. 10 in *An Atlas of Functions*. Washington, DC: Hemisphere, pp. 79-82, 1987.
- [26] Brusniak, L., Underbrink, J., and Stoker, R., "Acoustic Imaging of Aircraft Noise Sources Using Large Aperture Phased Arrays", AIAA Paper 2006-2715, 12th AIAA/CEAS Aeroacoustics Conference, May 8-10, 2006, Cambridge, Massachusetts.
- [27] Bracewell, R. "The Impulse Symbol." Ch. 5 in *The Fourier Transform and Its Applications*, 3rd ed. New York: McGraw-Hill, 2000.

APPENDIX A: Derivation of Equations

This appendix presents detailed derivations of several equations used in the main text. They are included here for the readers interested in the mathematical derivations without interrupting the flow of the presentation of the material.

A1.1 Properties of Delta Dirac Function δ

The delta function also obeys the so-called sifting property [27].

$$\int f(x)\delta(x-x_0)dx=f(x_0) \quad (\text{A.1})$$

A1.2 Derivative of Equation $g(\tau)=t-\tau-|\bar{x}-\bar{x}_s(\tau)|/c$

Differentiating $g(\tau)$ gives

$$\frac{dg(\tau)}{d\tau}=-1-\frac{1}{c}\frac{d|\bar{x}-\bar{x}_s(\tau)|}{d\tau} \quad (\text{A.2})$$

Expanding the coordinates of the observation and source leads to:

$$\begin{aligned} \frac{d|\bar{x}-\bar{x}_s(\tau)|}{d\tau} &= \frac{d}{d\tau}\left(\sqrt{(x_1-x_{s1}(\tau))^2+(x_2-x_{s2}(\tau))^2+(x_3-x_{s3}(\tau))^2}\right) \\ &= \frac{-2(x_1-x_{s1}(\tau))\frac{dx_{s1}(\tau)}{d\tau}-2(x_2-x_{s2}(\tau))\frac{dx_{s2}(\tau)}{d\tau}-2(x_3-x_{s3}(\tau))\frac{dx_{s3}(\tau)}{d\tau}}{2\sqrt{(x_1-x_{s1}(\tau))^2+(x_2-x_{s2}(\tau))^2+(x_3-x_{s3}(\tau))^2}} \\ &= -\frac{(x_1-x_{s1}(\tau))}{|\bar{x}-\bar{x}_s(\tau)|}\frac{dx_{s1}(\tau)}{d\tau}-\frac{(x_2-x_{s2}(\tau))}{|\bar{x}-\bar{x}_s(\tau)|}\frac{dx_{s2}(\tau)}{d\tau}-\frac{(x_3-x_{s3}(\tau))}{|\bar{x}-\bar{x}_s(\tau)|}\frac{dx_{s3}(\tau)}{d\tau} \end{aligned} \quad (\text{A.3})$$

Then

$$\frac{dg(\tau)}{d\tau} = -1 + \frac{(x_1 - x_{s1}(\tau))}{c|\vec{x} - \vec{x}_s(\tau)|} \frac{dx_{s1}(\tau)}{d\tau} + \frac{(x_2 - x_{s2}(\tau))}{c|\vec{x} - \vec{x}_s(\tau)|} \frac{dx_{s2}(\tau)}{d\tau} + \frac{(x_3 - x_{s3}(\tau))}{c|\vec{x} - \vec{x}_s(\tau)|} \frac{dx_{s3}(\tau)}{d\tau} \quad (\text{A.4})$$

However, the terms in this equation have the following physical meaning:

- i. $\frac{dx_{s\ell}(\tau)}{d\tau}$ is the ℓ^{th} component of the source velocity, $\vec{v}_s(\tau)$, and
- ii. $\frac{(x_\ell - x_{s\ell}(\tau))}{|\vec{x} - \vec{x}_s(\tau)|}$ is the ℓ^{th} directional cosine term of the vector pointing from the source to the observer, $\vec{x} - \vec{x}_s(\tau)$.

Therefore,

$$\frac{dg(\tau)}{d\tau} = -1 + \frac{1}{c} \frac{(\vec{x} - \vec{x}_s(\tau))}{|\vec{x} - \vec{x}_s(\tau)|} \cdot \vec{v}(\tau) = -1 + \frac{v_{so}(\tau)}{c} = -1 + M_{so}(\tau) \quad (\text{A.5})$$

The dot in this equation represents the inner product of the unit length vector in the direction of the source-to-observer, $(\vec{x} - \vec{x}_s(\tau))/|\vec{x} - \vec{x}_s(\tau)|$, and the source velocity, $\vec{v}(\tau)$. Thus, v_{so} is the component of the velocity of the source in the source-observer direction.

A1.3 Derivation of $\partial\tau/\partial t$

The relation between emission time τ and observer time t is given by equation (2.4) which can be written as:

$$c(t - \tau) = r \quad (\text{A.6})$$

where r is the distance between the source and the observer. For a source rotating around the z -axis with radius of rotation R , and rotational frequency ω_r , the propagation distance is given by:

$$r = \left\{ (x_1 - R \cos(\omega_r \tau))^2 + (x_2 - R \sin(\omega_r \tau))^2 + (x_3 - x_{s3})^2 \right\}^{1/2} \quad (\text{A.7})$$

Implicit differentiation of (A.6) yields:

$$c - c \cdot \frac{\partial \tau}{\partial t} = \frac{1}{2} \cdot r^{-1/2} \left[2(x_1 - R \cos(\omega_r \tau))(\omega_r \sin(\omega_r \tau)) \frac{\partial \tau}{\partial t} + 2(x_2 - R \sin(\omega_r \tau))(-\omega_r \cos(\omega_r \tau)) \frac{\partial \tau}{\partial t} \right] \quad (\text{A.8})$$

Expanding the terms inside the square brackets of (A.8):

$$c - c \cdot \frac{\partial \tau}{\partial t} = r^{-1/2} \left[\frac{\partial \tau}{\partial t} (x_1 \omega_r \sin(\omega_r \tau) - x_2 \omega_r \cos(\omega_r \tau)) \right] \quad (\text{A.9})$$

Collecting the $\partial \tau / \partial t$ terms on the r.h.s.

$$c = \frac{\partial \tau}{\partial t} \left(c + \frac{(x_1 \omega_r \sin(\omega_r \tau) - x_2 \omega_r \cos(\omega_r \tau))}{r^{1/2}} \right) \quad (\text{A.10})$$

Solving for $\partial \tau / \partial t$

$$\frac{\partial \tau}{\partial t} = \frac{1}{c + (x_1 \omega_r \sin(\omega_r \tau) - x_2 \omega_r \cos(\omega_r \tau)) / r^{1/2}} \quad (\text{A.11})$$

Note that the second term of the denominator represents the component of the source velocity in the direction of the observer which is given by equation (2.3) and is known as M_r . Therefore, substitution of equation (2.3) into equation (A5.6) yields:

$$\frac{\partial \tau}{\partial t} = \frac{1}{1 - M_r} \quad (\text{A.12})$$

A.1.4 Derivation of the Discrete Fourier Transform Equations

Fourier Series states that any periodic waveform $y(t)$ can be represented by an infinite series of sine and cosine functions according to the following expression:

$$y(t) = a_0 + \sum_{n=1}^{\infty} a_n \cos(\omega n t) + \sum_{n=1}^{\infty} b_n \sin(\omega n t) \quad (\text{A.13})$$

where $\omega = 2\pi / T_p$ is the fundamental angular frequency, and T_p is the repetition period of the waveform. The coefficient a_0 is given by

$$a_0 = \frac{1}{T_p} \int_{-T_p/2}^{T_p/2} y(t) dt \quad (\text{A.14})$$

which represents the time average of $y(t)$ over one period. The coefficients a_n and b_n are given by:

$$a_n = \frac{2}{T_p} \int_{-T_p/2}^{T_p/2} y(t) \cos(\omega n t) dt \quad (\text{A.15})$$

and

$$b_n = \frac{2}{T_p} \int_{-T_p/2}^{T_p/2} y(t) \sin(\omega n t) dt \quad (\text{A.16})$$

An insight of the meaning of coefficients a_n and b_n can be gained by noticing that equations (A.15) and (A.16) represent the correlation between the function $y(t)$ and the cosine and sine functions, respectively. That is, coefficient a_n measures the degree of similarity between

the functions $y(t)$ and $\cos(\omega t)$; whereas b_n measures the degree of similarity between the functions $y(t)$ and $\sin(\omega t)$.

The Fourier Series equation (A.13) can be written in exponential form as:

$$y(t) = \sum_{n=-\infty}^{n=+\infty} d_n e^{i\omega n t} \quad (\text{A.17})$$

where

$$d_n = \frac{1}{T_p} \int_{-T_p/2}^{T_p/2} y(t) e^{-i\omega n t} dt \quad (\text{A.18})$$

Unfortunately, not all signals are periodic. For non-periodic signals, equations (A.17) and (A.18) need to be modified. Any periodic signal can be made non-periodic by increasing the period T_p to approach infinite. In the limit as $T_p \rightarrow \infty$, equations (A.17) and (A.18) become:

$$y(t) = \frac{1}{2\pi} \int_{-\infty}^{\infty} Y(\omega) e^{i\omega t} d\omega \quad (\text{A.19})$$

where,

$$Y(\omega) = \int_{-\infty}^{\infty} y(t) e^{-i\omega t} dt \quad (\text{A.20})$$

Equations (A.19) and (A.20) are also known as the Fourier transform pair, which are the equivalent of Fourier Series equations (A.17) and (A.18) for non-periodic continuous signals of infinite duration.

In real life however, signals are obtained by sampling a continuous waveform at regular intervals of time, Δt . Furthermore, real life signals have a finite duration. Thus, the discrete version of the Fourier transform pair is given by:

$$y(n) = \frac{1}{N} \sum_{k=1}^{N-1} Y(k) e^{i\omega k \Delta t} \quad (\text{A.21})$$

where,

$$Y(\omega) = \sum_{n=0}^{N-1} y(n) e^{-i\omega k \Delta t} \quad (\text{A.22})$$

Equations (A.21) and (A.22) are known as the Inverse Discrete Fourier Transform (IDFT) and the Discrete Fourier transform (DFT) equations, respectively.

A1.5 Shifting and Scaling Properties of the Fourier Transform

The Shifting property:

Given the FT of a stationary signal $f(t)$

$$F(f) = \int_{-\infty}^{\infty} f(t) e^{-j2\pi ft} dt \quad (\text{A.23})$$

The FT of the shifted signal $f(t-a)$ is

$$F_s(f) = \int_{-\infty}^{\infty} f(t-a) e^{-j2\pi ft} dt \quad (\text{A.24})$$

Changing variables $\tau = t - a$

$$\begin{aligned}
F_s(f) &= \int_{-\infty}^{\infty} f(\tau) e^{-j2\pi f(\tau+a)} d\tau = e^{-j2\pi fa} \int_{-\infty}^{\infty} f(\tau) e^{-j2\pi f\tau} d\tau \\
F_s(f) &= e^{-j2\pi fa} F(f)
\end{aligned} \tag{A.25}$$

Thus, the FT of the shifted signal is the phase adjusted FT of the original signal by the term $e^{-j2\pi fa}$.

Scaling Property:

The FT of the scaled signal $f(at)$ is

$$F_s(f) = \int_{-\infty}^{\infty} f(at) e^{-j2\pi ft} dt \tag{A.26}$$

Changing variables $\tau = at$

$$F_s(f) = \int_{-\infty}^{\infty} f(\tau) e^{-j2\pi f\tau/a} \frac{d\tau}{a} = \frac{1}{a} \int_{-\infty}^{\infty} f(\tau) e^{-j2\pi \hat{f}\tau} d\tau \tag{A.27}$$

where $\hat{f} = f/a$ is the frequency content of the original signal.

Then

$$F_s(f) = \frac{1}{a} F(\hat{f}) = \frac{1}{a} F\left(\frac{f}{a}\right) \tag{A.28}$$

Thus, the FT of the scaled signal is obtained by adjusting the frequency and amplitude of the FT of the original signal.

A1.6 Linearization of the Reception vs Emission Times

The linearization of the reception time in terms of the emission time is simply to expand

$$t = h_n(\tau) = \tau + \frac{|\vec{x}_n - \vec{x}_s(\tau)|}{c} \quad \text{for} \quad -\frac{T}{2} \leq \tau \leq \frac{T}{2} \quad (\text{A.29})$$

in Taylor' series around $\tau_o = 0$. In general, the expansion gives

$$t \approx \tau + \frac{|\vec{x}_n - \vec{x}_s(\tau_o)|}{c} + \frac{1}{c} \left. \frac{d|\vec{x}_n - \vec{x}_s(\tau)|}{d\tau} \right|_{\tau_o} (\tau - \tau_o) = \tau + \frac{|\vec{x}_n - \vec{x}_s(0)|}{c} + \frac{1}{c} \left. \frac{d|\vec{x}_n - \vec{x}_s(\tau)|}{d\tau} \right|_{\tau_o=0} \tau \quad (\text{A.30})$$

or

$$t = h_n(\tau) \approx h_{no} + \frac{dh_n}{d\tau} \tau = h_{no} + h_{nr} \tau \quad (\text{A.31})$$

where

$$\begin{aligned} h_{no} &= \frac{|\vec{x}_n - \vec{x}_s(0)|}{c} \\ h_{nr} &= 1 + \frac{1}{c} \left. \frac{d|\vec{x}_n - \vec{x}_s(\tau)|}{d\tau} \right|_{\tau_o=0} = 1 - \frac{1}{c} \frac{(\vec{x}_n - \vec{x}_s(0)) \cdot \vec{v}_s(0)}{|\vec{x}_n - \vec{x}_s(0)|} \end{aligned} \quad (\text{A.32})$$

However, the term $(\vec{x}_n - \vec{x}_s(\tau_o))/|\vec{x}_n - \vec{x}_s(\tau_o)|$ is the directional cosine of the vector pointing from the source to the nth microphone. Thus, the term h_{nr} becomes

$$h_{nr} = 1 - \frac{1}{c} \left. \frac{d|\vec{x}_n - \vec{x}_s(\tau)|}{d\tau} \right|_{\tau_o=0} = 1 - M_{sn}(0) \quad (\text{A.33})$$

The explicit equations to use in the linearization for a source moving linearly and rotating are presented next.

Linear Motion

Assuming the coordinate system at the source, the relation between emission time and reception time for sources in linear motion is

$$t = \tau + \frac{\sqrt{(x_{1n} - U\tau)^2 + x_{2n}^2 + x_{3n}^2}}{c} \quad (\text{A.34})$$

and the source velocity

$$\vec{v}_s(\tau) = -U\tau\vec{e}_1 \quad (\text{A.35})$$

Rotating Motion

The relation between emission time and reception time for rotating sources is given by equation (4.30) which is rewritten here for convenience as

$$t = h_n(\tau) = \tau + \frac{|\vec{x}_n - \vec{x}_l(\tau)|}{c} \quad (\text{A.36})$$

$$t = h_n(\tau) = \tau + \frac{\sqrt{\{x_{1n} - r_l \cos(\omega_r \tau + \phi_l)\}^2 + \{x_{2n} - r_l \sin(\omega_r \tau + \phi_l)\}^2 + x_{3n}^2}}{c}$$

and the source velocity

$$\vec{v}_s(\tau) = r_l \omega_r \sin(\omega_r \tau + \phi_l) \vec{e}_1 - r_l \omega_r \cos(\omega_r \tau + \phi_l) \vec{e}_2 \quad (\text{A.37})$$